

REPORT DOCUMENTATION PAGE

AFRL-SR-BL-TR-00-

Public reporting burden for this collection of information is estimated to average 1 hour per response, including the time for reviewing existing information, gathering new information, and completing and reviewing this collection of information. Send comments regarding this burden estimate or any other aspect of this collection of information, including suggestions for reducing this burden to Washington Headquarters Services, Directorate for Information Operations and Reports, 1204, Arlington, VA 22202-4302, and to the Office of Management and Budget, Paperwork Reduction Project (01-1204), Arlington, VA 22202-4302.

Gathering
of
/ Suite

0442

1. AGENCY USE ONLY (Leave blank)		2. REPORT DATE August 31, 2000		3. REPORT TYPE AND DATES COVERED Final Technical Report, 01 Jun 97-31 May 00	
4. TITLE AND SUBTITLE Development of Methods to Observe Material's Fatigue and Corrosion Damage through Surface Characteristics Monitoring				5. FUNDING NUMBERS Grant No. F49620-97-0445	
6. AUTHOR(S) Laura Beth Simon Jody Lynn Schroeder					
7. PERFORMING ORGANIZATION NAME(S) AND ADDRESS(ES) University of Dayton 300 College Park Dayton, OH 45469-0121				8. PERFORMING ORGANIZATION REPORT NUMBER UDR-TR-2000-00094	
9. SPONSORING / MONITORING AGENCY NAME(S) AND ADDRESS(ES) AFOSR/NL 110 Duncan Avenue Room B115 Bolling AFB DC 20332-8050				10. SPONSORING / MONITORING AGENCY REPORT NUMBER	
11. SUPPLEMENTARY NOTES					
12a. DISTRIBUTION / AVAILABILITY STATEMENT APPROVED FOR PUBLIC RELEASE: DISTRIBUTION UNLIMITED					12b. DISTRIBUTION CODE
13. ABSTRACT (Maximum 200 Words) White Light Interferometry was used for surface characterization accompanied by other methods to observe materials damage caused by corrosion and fatigue. White Light Interferometry has a spatial resolution of 0.2 μ m and depth resolution of 3 nm. It was applied to study corroded surfaces. Parameters such as average roughness and pit depths were determined. The results provided the details of the critical pit size that can lead to fatigue crack initiation in A1-2024-T3. A relationship between the critical pit depth and the stress intensity factor, a structural integrity parameter, was determined. In the second part of this report, a method to characterize the depression zone at a crack tip and predict upcoming fracture under static load using white light interference microscopy was developed and studied. Results showed an exponential relationship between the area of the crack tip deformation and volume of the crack tip depression with the stress applied to the pre-cracked sample. The findings of this study indicate that it is possible to determine a critical rate of change in surface deformation at a crack tip versus the applied stress that can be used to predict oncoming catastrophic failure.					
14. SUBJECT TERMS Interferometry, Parameters					15. NUMBER OF PAGES 147
					16. PRICE CODE
17. SECURITY CLASSIFICATION OF REPORT Unclassified	18. SECURITY CLASSIFICATION OF THIS PAGE Unclassified	19. SECURITY CLASSIFICATION OF ABSTRACT Unclassified		20. LIMITATION OF ABSTRACT UL	

NSN 7540-01-280-5500

Standard Form 298 (Rev. 2-89)
Prescribed by ANSI Std. Z39-18
298-102

DTIC QUALITY INSPECTED 4

20000 925 089

***Development of Methods to Observe Material's
Fatigue and Corrosion Damage through
Surface Characteristics Monitoring***

FINAL TECHNICAL REPORT

Grant No. F49620-97-1-0445

**Project A: In-situ Detection of Corrosion Initiation in A1 2024-T3
By: Laura Beth Simon, December 1999**

**Project B: Detection of Internal Damage in Ti-6Al-4V Caused by Fatigue
By: Jody Lynn Schroeder, May 2000**



CENTER FOR MATERIALS DIAGNOSTICS

**University of Dayton
300 College Park
Dayton, OH 45469-0121
Tel: 937-229-4830
Fax: 937-229-4032**

The results of this report are also part of the NDE MURI Report.

PART A
TABLE OF CONTENTS

ABSTRACT.....	A-1
LIST OF FIGURES.....	A-3
LIST OF TABLES.....	A-7
LIST OF ABBREVIATIONS	A-8
CHAPTER	
1. INTRODUCTION	A-9
2. REVIEW OF RELATED MATERIAL.....	A-12
2.1 PITTING CORROSION.....	A-12
2.2 PITTING AND FATIGUE	A-16
3. EXPERIMENTAL PROCEDURE	A-19
3.1 ACCELERATED CONTROLLED PITTING TECHNIQUE	A-19
3.2 INSTRUMENTATION	A-23
3.2.1 Electrochemical Equipment.....	A-23
3.2.2 Characterization Equipment	A-25
3.3 FATIGUE EXPERIMENT	A-29
4. RESULTS AND DISCUSSION	A-32
4.1 DEVELOPMENT OF ACCELERATED CONTROLLED PITTING TECHNIQUE	A-32
4.1.1 Chemical Techniques	A-32
4.1.2 Polarization Techniques	A-34
4.1.3 Characterization Techniques	A-42

4.2 FATIGUE EXPERIMENT AND RESULTS	A-54
4.2.1 Production of Pits	A-55
4.2.2 Characterization of Pitted Samples.....	A-58
4.2.3 Fatigue Testing	A-67
4.2.4 Stress Intensity Factor Calculation	A-72
4.2.5 Relationships Resulting From Controlled Fatigue Experiment.....	A-75
5. SUMMARY	A-87
5.1 FUTURE WORK.....	A-88
APPENDIX A.....	A-89
BIBLIOGRAPHY	A-92

PART B

TABLE OF CONTENTS

ABSTRACT.....	B-94
LIST OF FIGURES.....	B-96
CHAPTER	
I. INTRODUCTION.....	B-98
1.1 Use of Titanium in High Performance Aircraft Components	
1.2 Significance of Deformation Zone and Crack Propagation	
1.3 Fracture Mechanics and Crack Tip Deformation	
1.4 Need for Novel Surface Technique to Quantify Crack Tip Deformation	
1.5 Objectives of this Work	
1.6 Application of a Novel Optical Surface Diagnostic Technique	
1.7 Shape and Size of Crack Tip Deformation	
1.8 Distinguishing the Components of Surface Deformation	
II. EXPERIMENTAL PROCEDURES.....	B-109
2.1 Material	
2.2 Crack Initiation	
2.3 Observation of Crack Tip Deformation Zone	
2.4 White Light Interference Profilometry	
2.5 Quantification of Topographical Data	
2.6 Image Preparation for Calculations	
III. RESULTS AND DISCUSSION	B-120
3.1 Incrementally Increased Load Results	
3.1.1 Profilometer Images	
3.1.2 Stress Intensity Factor Calculations and Consideration	
3.1.3 Analysis of Profilometer Images	
3.2 Deformation Shape and Size	
3.2.1 Influence of Microstructure on Deformation Shape	
3.2.2 Affects of Depression Volume on the Specimen Cross Sectional Area	
3.2.3 Correlating Surface Deformation and Plastic Deformation	
3.3 Deformation as a Function of Time	
3.4 Deformation Relaxation	
3.5 Criteria for Failure Prediction	

IV. CONCLUSIONS AND RECOMMENDATIONS.....B-135

4.1 Conclusions

4.2 Recommendations

BIBLIOGRAPHY.....B-138

ABSTRACT

INFLUENCE OF PITTING CORROSION ON THE LOSS OF STRUCTURAL INTEGRITY IN ALUMINUM ALLOY 2024-T3

Name: Simon, Laura Beth
University of Dayton, 1999

Research Advisor: Mohammed Khobaib, Ph. D.
Academic Advisor: Kevin Myers, D.Sc., P.E.

The United States Air Force has decided to extend the life of its existing aircraft. These aging aircraft are becoming an increasingly important issue because they are to be used beyond their designed life. One of the main causes of failure of aging aircraft is due to corrosion and fatigue of its aluminum alloy structures, with pitting corrosion being the most serious type of corrosion that affects the aluminum structures. To study the role of pitting corrosion in fatigue crack initiation, pits were created on high strength aluminum 2024-T3 dog-bone fatigue samples by an accelerated electrochemical method, followed by fatigue testing. These pits have a variety of morphologies. The corrosion damage was described quantitatively using nondestructive means in order to investigate the role pitting plays in fatigue crack nucleation and subsequent loss of structural integrity of the material. The non-destructive techniques used in this study were optical microscopy, scanning electron microscopy, and white light interference microscopy. The pitted surface was examined, and parameters such as average roughness and pit depth were determined. In addition, 3-dimensional images of the pitted surface were obtained.

These results provide the details of the critical pit size that can lead to fatigue crack initiation in Al 2024-T3. The samples were fatigued to failure, and the fractured surfaces were examined using scanning electron microscopy and optical microscopy. The critical pit size was determined, and the stress intensity factor for each sample was calculated. A relationship between the critical pit depth and the stress intensity factor, a structural integrity parameter, was determined. The crack growth behavior of a fatigue crack initiating from a pit was modeled. However, more data with various pit depths and distributions are needed before any meaningful conclusions can be made. This investigation is invaluable in understanding the role of pitting in fatigue crack initiation, and will eventually aid in extending the life of the growing aging aircraft fleet.

LIST OF FIGURES

1. Schematic of a pit. Dimension a is the radius or depth of the pit, and dimension c is the diameter of the pit A-12
2. Schematic of the reaction and migration processes occurring in a corrosion pit ... A-14
3. Schematic of the three modes of crack growth: (a) mode I, (b) mode II, and (c) mode III A-18
4. Masked sample, prior to pitting A-20
5. Gauge section of masked dog-bone sample with imperfect coating of clear fingernail polish..... A-21
6. The electrochemical set-up used in all experiments A-22
7. Schematic of the white light surface profiler..... A-26
8. Schematic of image formation process in the SEM..... A-28
9. Geometry of dog-bone fatigue sample made of Al 2024-T3. Primary dimensions are in inches, and dimensions in parentheses are in cm A-29
10. Evan's Diagram A-34
11. Potentiodynamic plot showing behavior of Al 2024-T3. SCE refers to the saturated Calomel reference electrode A-36
12. A representative galvanostatic plot used to create pits on Al 2024-T3 sample..... A-37
13. Potentiodynamic plot used to create pits on Al 2024-T3 sample A-38
14. Optical micrograph of the top surface of a vinyl-silane sol-gel film..... A-39
15. (a)-(c) Optical micrographs of sol-gel coated pitted dog-bone samples at different magnifications. (d) Sol-gel coated pitted dog-bone sample covered with waterproof tape..... A-40
16. First optical micrograph of pitted dog-bone sample..... A-42

17. Second optical micrograph of pitted dog-bone sample	A-43
18. (a) WLIM surface profile of sample shown in Figure 16. (b) WLIM surface profile of sample shown in Figure 17.....	A-44
19. (a) WLIM maximum contrast profile of sample shown in Figure 16 and 18(a). (b) WLIM maximum contrast profile of sample shown in Figure 17 and 18(b).....	A-46
20. (a) WLIM 3-dimensional profile of sample shown in Figures 16, 18(a) and 19(a). (b) WLIM 3-dimensional profile of sample shown in Figure 17, 18(b) and 19(b).....	A-47
21. (a) Surface profile used in two- dimensional analysis. (b) X profile in two-dimensional analysis illustrating the determination of pit depth. (c) Y profile in two-dimensional analysis illustrating the determination of pit diameter	A-49-50
22. Center pit as a subregion of the surface profile shown in Figure 18(a).....	A-50
23. Illustration of volume calculation.	A-52
24. Interactive volume profile used to determine total pit volume.....	A-52
25. Representative examples of dog-bone samples polarized without the fingernail polish coating. (a) 4 hours of polarization (b) 8 hours of polarization (c) 12 hours of polarization	A-56
26. Six examples of dog-bone samples polarized with the fingernail polish coating. (a) 4 hours of polarization (b) 8 hours of polarization (c) 12 hours of polarization (d) 16 hours of polarization (e) 20 hours of polarization (f) 24 hours of polarization	A-57
27. Bare dog-bone sample polarized for 4 hours: (a) Optical micrograph of pitted surface (b) WLIM maximum contrast profile showing shallow surface features (c) WLIM surface profile (d) WLIM 3-D profile showing pit contour and shape	A-60
28. Bare dog-bone sample polarized for 12 hours: (a) Optical micrograph of pitted surface (b) WLIM maximum contrast profile showing shallow surface features (c) WLIM surface profile (d) WLIM 3-D profile showing pit contour and shape	A-61
29. Fingernail polish coated dog-bone sample polarized for 4 hours: (a) Scanning electron micrograph of pitted surface (b) WLIM maximum contrast profile showing shallow surface features (c) WLIM surface profile (d) WLIM 3-D profile showing pit contour and shape	A-62
30. Fingernail polish coated dog-bone sample polarized for 12 hours: (a) Optical micrograph of pitted surface (b) WLIM maximum contrast profile showing shallow surface features (c) WLIM surface profile (d) WLIM 3-D profile showing pit contour and shape	A-63

31. Fingernail polish coated dog-bone sample polarized for 16 hours: (a) Optical micrograph of pitted surface (b) WLIM maximum contrast profile showing shallow surface features (c) WLIM surface profile (d) WLIM 3-D profile showing pit contour and shape A-64
32. Fingernail polish coated dog-bone sample polarized for 20 hours: (a) Scanning electron micrograph of pitted surface (b) WLIM maximum contrast profile showing shallow surface features (c) WLIM surface profile (d) WLIM 3-D profile showing pit contour and shape A-65
33. Fingernail polish coated dog-bone sample polarized for 24 hours: (a) Scanning electron micrograph of pitted surface (b) WLIM maximum contrast profile showing shallow surface features (c) WLIM surface profile (d) WLIM 3-D profile showing pit contour and shape A-66
34. Fatigue crack growth schematics of pitted sample A-67
35. Fingernail polish coated dog-bone sample polarized for 4 hours (a) Optical micrograph of pitted surface before fracture (b) Optical micrograph of pitted surface after fracture (c) Fractured surface showing semi-elliptic crack A-69
36. Fingernail polish coated dog-bone sample polarized for 20 hours (a) Optical micrograph of pitted surface before fracture (b) Optical micrograph of pitted surface after fracture (c) Fractured surface showing semi-elliptic crack A-70
37. Fingernail polish coated dog-bone sample polarized for 8 hours (a) Optical micrograph of pitted surface before fracture (b) Optical micrograph of pitted surface after fracture (c) Fractured surface showing semi-elliptical crack A-71
38. Semi-elliptical surface crack configuration, where dimension a is the crack depth, t is half-thickness of plate, b is half-width of cracked plate, and c is half-length of Crack A-72
39. Coordinate system used to define parametric angle for $a/c \leq 1$ A-73
40. Cycles to failure versus polarization time for samples not coated with the fingernail polish A-76
41. Cycles to failure versus polarization time for samples coated with the fingernail Polish A-77
42. Critical pit depth versus polarization time A-79
43. Rms roughness versus polarization time A-80

44. Mass loss versus polarization time	A-82
45. Stress intensity factor versus critical pit depth	A-83
46. Stress intensity factor versus rms roughness	A-85
47. Crack growth rate versus ΔK	A-86

LIST OF TABLES

1. Test matrix for the electrochemically pitted fatigue samples. Polarization time refers to the length of time the sample was polarized A-31
2. Chemical composition limits for aluminum alloy 2024-T3 A-32

LIST OF ABBREVIATIONS

DARPA-MURI	Defense Advanced Research Projects Agency-Multidisciplinary University Research Initiative
AFOSR	Air Force Office of Scientific Research
Al 2024-T3	Aluminum alloy 2024-T3
NDE	Non-Destructive Evaluation
SiC	Silicon Carbide
SCE	standard Calomel electrode
HCl	hydrochloric acid
NaCl	Sodium Chloride
WLIM	White Light Interference Microscopy
SEM	Scanning Electron Microscopy
VSI	Vertical Scanning Interferometry
rms	root-mean-square
WPAFB	Wright Patterson Air Force Base
UDRI	University of Dayton Research Institute

CHAPTER 1

INTRODUCTION

In recent years, the United States Air Force has reduced the production of new aircraft, and has turned its focus to extending the life of the existing fleet. Consequently, these existing aircraft, known as aging aircraft, will be operated for longer than they were originally designedⁱ. For example, the C/KC-135, which was produced in the 1950's and 1960's, is currently projected for service through the first half of the 21st century.ⁱⁱ These aging aircraft require extensive maintenance in addition to the regular routine maintenance cycle to prevent failure that may result, in the worst case scenario, in a fatal accident. One of the main causes of failure of aging aircraft is corrosion damage, specifically corrosion of the aluminum alloy structures. Many different types of corrosion damage may affect the aluminum structures of an aircraft, depending on the environmental conditions encountered. General corrosion, pitting corrosion, crevice corrosion, exfoliation corrosion and galvanic corrosion are among the most common forms observed for aluminum alloys. Pitting corrosion is most commonly observed in high strength aluminum alloys and is one of the most dangerous types of corrosion that may affect the life of aircraft.ⁱⁱⁱ Research has shown that pits are one of the nucleation sites of fatigue crack formation in aluminum alloys.^{iii,iv,v} Continued growth of these cracks under fatigue results in premature failure of the aircraft structure.

It is well known that the conjoint action of corrosion and stress leads to accelerated loss in the structural integrity of aircraft. However, the critical stage of damage, where, under stress, a corroded area leads to crack initiation is not well understood. In addition, no reliable technique exists to detect the onset and propagation of the localized corrosion attack. Therefore, the Department of Defense has initiated this research program to quantitatively investigate the role of corrosion damage on the fatigue behavior of high strength aluminum alloys.

The most significant corrosion problems are usually associated with airframe components, such as rivets, fasteners and joints. To date, the practical solution to inspect for corrosion damage in these areas is to completely strip the paint from the plane. This method is naturally quite expensive, time consuming, and sometimes no corrosion is found. Therefore, in current practice, a plane is not stripped until a major overhaul of the plane is performed. Any major corrosion problems are repaired at this time, but minor damage, such as shallow general pitting, is often overlooked during the overhaul. Because there are no good methods for detecting minor damage, this oversight can lead to catastrophic consequences. It is much easier and more cost effective to repair minor damage than to wait until the corrosion has become a significant problem. In addition, the minor undetected corrosion may also lead to related fatigue damage, resulting in even greater repair costs.^{vi}

Life extension programs for aging fleets and the development of non-chromate based primers and coating systems have lead to a large amount of research in the testing and characterization of materials and coatings. These efforts have shown the need for corrosion damage detection tools for airframe and engine materials. Since the aerospace

industry and research communities have realized the significance of corrosion in initiating fatigue damage, efforts have been focused on the development of a method for detecting the onset of corrosion. As stated previously, unnecessary routine maintenance is very time consuming and expensive, but aircraft safety must be maintained. A corrosion detection tool would minimize the loss of structural integrity by timely repair, therefore increasing the safety of the aircraft. The result will simultaneously increase reliability of aircraft while considerably reducing the operating costs.^{vi}

This DARPA-MURI (Defense Advanced Research Projects Agency-Multidisciplinary University Research Initiative) five year project is sponsored by the Air Force Office of Scientific Research (AFOSR). It is a major effort to develop enabling methodologies of detection and characterization of the early stages of damage in aerospace materials.

The primary objective of this part of the investigation is to develop a method of producing controlled pitting, so that pits of varying sizes, morphologies and distributions could be created on standard fatigue samples made of aluminum alloy 2024-T3. These pitted samples are characterized using electrochemical, metallurgical and non-destructive evaluation (NDE) tools. The samples are then subjected to controlled fatigue. The main purpose of this study is to find a correlation between a pitting / surface parameter and a structural integrity parameter. Such a relationship could be to predict the life of the structure.

CHAPTER 2

REVIEW OF RELATED MATERIAL

2.1 PITTING CORROSION

Pitting is a form of intensive localized corrosion that creates holes in the surface of a metal. A passive metal is one in which a very thin film is present on the surface, enhancing the metal's corrosion resistance. For aluminum and its alloys, this film is formed when the surface interacts with oxygen or water forming a thin layer of aluminum oxide on the surface. It is thought that when this passive film is compromised, pitting can take place.⁷ Pits may be small or large in diameter depending on the alloy and the aggressive environment, but are more commonly small. Pit density and distribution also varies depending on the affected metal and alloy. In the simplest assumption, a pit may be described as a cavity or hole with a surface diameter and depth,⁷ as seen in Figure 1.

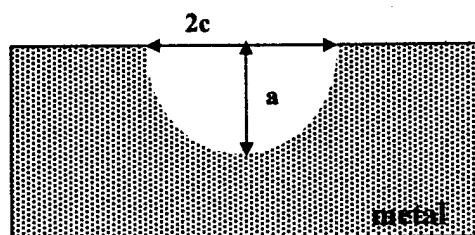


Figure 1. Schematic of a pit. Dimension a is the depth of the pit, and dimension $2c$ is the diameter of the pit.

Pitting is one of the most destructive forms of corrosion. Although only a small percentage of metal is dissolved, the result can lead to total failure of the structure in a very short time. It is difficult to detect pits due to their small size and the fact that they may be covered with corrosion product.⁷ It is not well known how or why pitting initiates, however, the pitting mechanism has been investigated extensively in an effort to learn how to prevent this form of corrosion from causing damage.

For any type of corrosion to take place, including pitting, five conditions must be met:

1. An anode must be present. This is where the oxidation reaction occurs.
2. A cathode must be present. This is where the reduction reaction occurs.
3. The anode and cathode must be electrically connected allowing electrons to flow from anode to cathode.
4. An electrolyte (liquid solution) must be present allowing ionic flow between the cathode and anode.
5. A cathodic reactant must be present allowing the consumption of electrons.

These conditions, when applied to the pitting process, are illustrated using Figure 2.

Once initiated, the corrosion pit is an autocatalytic process, inferring that the corrosion processes within the pit produce conditions that are both stimulating and required for continued growth of the pit. Figure 2 illustrates a metal, M, being pitted by an aerated solution of sodium chloride.

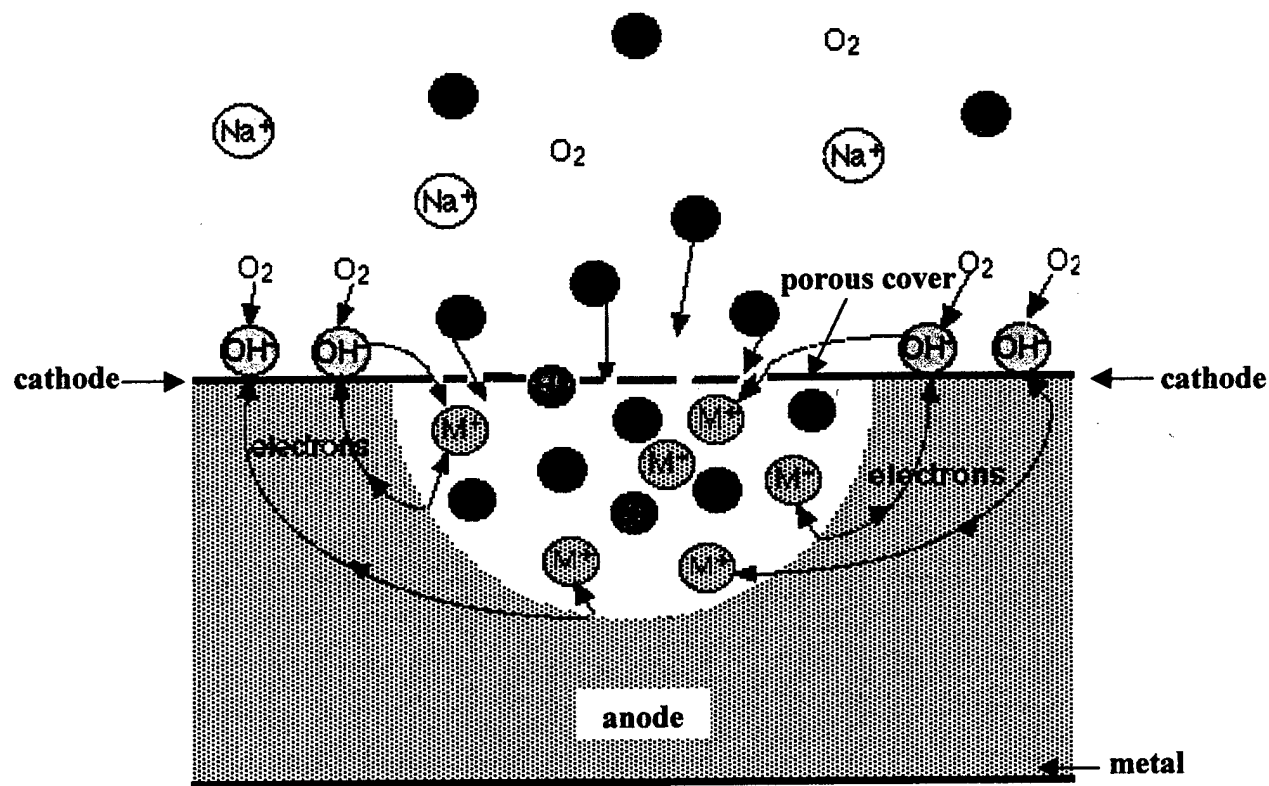


Figure 2. Schematic of the reaction and migration processes occurring in a corrosion pit.⁷

The metal, M, is rapidly dissolved within the pit by the following oxidation reaction:



The electron released by this reaction then travels through the metal substrate to the surface. At the surface, under neutral pH conditions, oxygen reduction takes place by the following reaction:



The dissolution of the metal within the pit tends to produce an excess of positive charge due to the metal cations being released into the electrolyte, as shown in Eq. 1. To

maintain electroneutrality, chloride ions migrate into the interior of the pit from the bulk solution. This results in a high concentration of metal cations and chloride anions inside the pit. When the concentration is large enough, this metal salt reacts with the water and the following hydrolysis reaction produces hydrogen ions:



Both hydrogen and chloride ions stimulate the dissolution of most metals and alloys, although the reason is still not clear. This results in a driving force for the oxidation reaction (Eq. 1) that dissolves the metal. Therefore, the entire pitting process repeats itself. This is why pitting is considered self-propagating once the process is initiated.⁷

Although pure aluminum is corrosion resistant, mechanically it is very weak. Specific alloying elements are added to aluminum to increase its strength without adding much weight. Thus, aluminum alloys attain suitable properties to be used in aircraft structures. Aluminum alloys are relatively strong for their light weight. However, some of the alloying elements are a potential cause for loss in corrosion resistance. For example, in Al 2024-T3, copper is one of the main alloying elements. According to the galvanic series, copper is noble compared to aluminum.⁷ The term noble refers to the fact that aluminum will act as the anode in the presence of copper, and copper will act as the cathode. Since the copper is present in the main strengthening phase dispersed over the surface of the alloy, the two metals are in electrical contact with each other. The final corrosion criterion is realized when the aluminum alloy is exposed to an electrolyte. The aluminum corrodes resulting in pitting corrosion.

2.2 PITTING AND FATIGUE

This section describes the relationship between pitting corrosion and fatigue as it occurs on a structure in the field.

Corrosion pitting coupled with an applied stress can have a profound effect on limiting the lifetime of the aluminum structures on aircraft⁸. This pitting and fatigue process has been conceptually divided into the following stages⁹:

1. electrochemical stage and pit nucleation
2. pit growth
3. competitive mechanisms in pit growth and fatigue crack nucleation
4. chemically "short crack" growth
5. "short crack" transition to "long crack" behavior
6. long crack growth
7. unstable crack growth and final failure

This study did not exactly duplicate all the stages shown above. Instead of the pitting and fatigue crack nucleation occurring simultaneously in step 3, the pits were created first, then the samples were fatigued in laboratory air. However, most of the stages shown above still apply to this experimental investigation, and it is important to understand why this process can lead to failure in aging aircraft.

Pit formation and shape are random phenomena. The location of a pit and its shape are dependent upon several material and electrochemical factors. Pits usually initiate at some chemical or physical heterogeneity at the surface, such as inclusions, second phase particles, solute-segregated grain boundaries, flaws, mechanical damage or dislocations.^{9,10} These sites are vulnerable to corrosive attack if the protective film thickness in this area is uneven or broken. This allows the electrolyte to contact the metal

2.2 PITTING AND FATIGUE

This section describes the relationship between pitting corrosion and fatigue as it occurs on a structure in the field.

Corrosion pitting coupled with an applied stress can have a profound effect on limiting the lifetime of the aluminum structures on aircraft⁸. This pitting and fatigue process has been conceptually divided into the following stages⁹:

1. electrochemical stage and pit nucleation
2. pit growth
3. competitive mechanisms in pit growth and fatigue crack nucleation
4. chemically "short crack" growth
5. "short crack" transition to "long crack" behavior
6. long crack growth
7. unstable crack growth and final failure

This study did not exactly duplicate all the stages shown above. Instead of the pitting and fatigue crack nucleation occurring simultaneously in step 3, the pits were created first, then the samples were fatigued in laboratory air. However, most of the stages shown above still apply to this experimental investigation, and it is important to understand why this process can lead to failure in aging aircraft.

Pit formation and shape are random phenomena. The location of a pit and its shape are dependent upon several material and electrochemical factors. Pits usually initiate at some chemical or physical heterogeneity at the surface, such as inclusions, second phase particles, solute-segregated grain boundaries, flaws, mechanical damage or dislocations.^{9,10} These sites are vulnerable to corrosive attack if the protective film thickness in this area is uneven or broken. This allows the electrolyte to contact the metal

surface, creating the right conditions for corrosion to occur. The breakdown of the passive film and the initiation of the pitting process are probably the least understood aspect of the pitting phenomena.¹⁰ The theories that describe passive film breakdown and initiation of pitting have been divided into 3 categories: passive film penetration, film breaking and adsorption.^{9,10} However, pits in real alloys are most often associated with inclusions or second-phase particles.

The mechanism of pit growth is the next important phase of activity. The rate of pit growth is principally governed by the material, local solution conditions, and stress state. Several pit growth mechanisms are described in the literature.^{9,11}

During the third stage, pit growth and fatigue damage compete with one another. The electrochemical growth rate of a pit is enhanced if the damage produced by the various processes interact with each other. When the pit growth rate is smaller than the damage produced under fatigue for crack nucleation, the pit transforms to a crack. The pit amplifies the applied stress at its tip. These types of flaws are called stress raisers because of their ability to concentrate the applied stress.¹² A study by Chen *et al.* suggested that a threshold pit size must be reached before a fatigue crack will initiate, which is consistent with fatigue threshold theory.¹³

There are three fundamental modes by which a load can operate on a crack: mode I is an opening or tensile mode, mode II is a shear or sliding mode, and mode III is a tearing mode.¹² Mode I is encountered most frequently, and it is the only mode that was considered in this investigation. A schematic illustrating modes I, II, and III is shown in Figure 3.

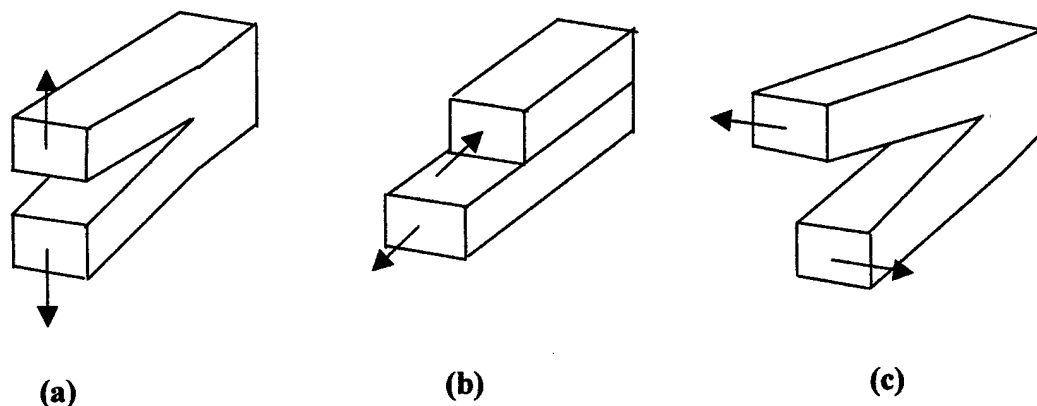


Figure 3. Schematic of the three modes of crack growth: (a) mode I, (b) mode II, and (c) mode III.¹²

A parameter has been developed to quantify the stress distribution around a flaw, such as a pit. This parameter is known as a stress intensity factor, and is represented by the letter K . The stress intensity factor has the units of $\text{MPa}\sqrt{\text{m}}$.

Once a crack has initiated, it may follow short crack behavior. This behavior has not been investigated very thoroughly, so limited data is available⁵. The short cracks grow quite early in this process and appear to propagate much more quickly than the usual long cracks, which have been studied much more extensively.

Long cracks do not propagate at the high rate of short cracks. Their growth is slower and more predictable compared to short crack growth. Depending on frequency and the environment, the crack growth rate increases abruptly after a certain critical stage is reached⁹. Unstable crack growth then dominates the process, and failure of the structure occurs.

CHAPTER 3

EXPERIMENTAL PROCEDURE

3.1 ACCERLERATED CONTROLLED PITTING TECHNIQUE

The section discusses the technique for creating reproducible controlled pitting corrosion on high strength aluminum alloy 2024-T3 (Al 2024-T3) samples.

The initial pitting experiments were conducted using bare or uncoated 50 mm x 25 mm x 1.6 mm Al 2024-T3 samples. The samples were prepared as follows: The surface was polished using 600 grit silicon carbide (SiC) paper. After polishing, the specimens were ultrasonically cleaned in water and acetone, dried in a stream of air, and stored in a desiccator. A second set of experiments was conducted with sol-gel coated 50 mm x 25 mm x 1.6 mm Al 2024-T3 samples. The cross-linked vinyl silane sol-gel film was approximately 100 μm thick. The sample surface was prepared as described above before the sol-gel was introduced onto the surface. The sample was laid on a flat surface, and the sol-gel was poured over the sample using a syringe. The samples were then left undisturbed overnight. The sol-gel coating covered most of the sample surface, however a waterproof tape was also placed over the sol-gel coating except for a small area in the center of the sample. This was done to restrict the area exposed to the electrolyte, as shown in Figure 4.

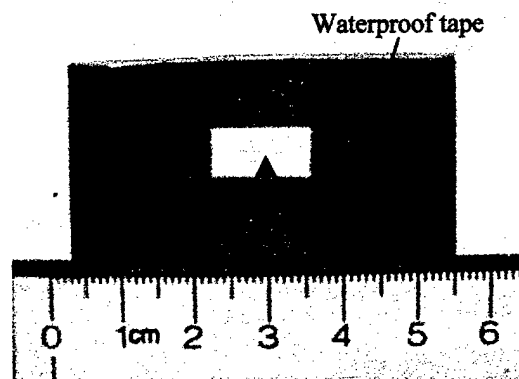


Figure 4. Masked sample, prior to pitting.

After this technique for masking and coating the samples had been developed, the main experiments were conducted using dog-bone fatigue samples. The sample surface for the dog-bone samples was prepared as follows: the surface was polished manually using 600 grit SiC paper. After polishing, the surface was rinsed with distilled water, and ultrasonically cleaned in distilled water. A stream of filtered air was used to dry each sample. A sol-gel coating was applied to this surface, and then the waterproof tape was placed over it. Cracks formed in the sol-gel after it had dried, resulting in an imperfect coating. It was discovered, however, that the sol-gel coating could not be removed from the sample surface for analysis without destroying the sample. Therefore, a clear fingernail polish was used to mask a selected part of the specimen surface instead of the sol-gel coating. The dog-bone sample was prepared as described above, but the fingernail polish was applied after the waterproof tape was in place. Several flaws were then introduced into the fingernail polish when it was still tacky to create a controlled flawed coating. The flaws were created using the tip of a needle, and care was taken not to scratch the sample surface beneath the fingernail polish, as shown in Figure 5. This procedure allows the pits to form in the vicinity of the holes and reduces the initiation of a large number of pits often seen with bare Al 2024-T3.

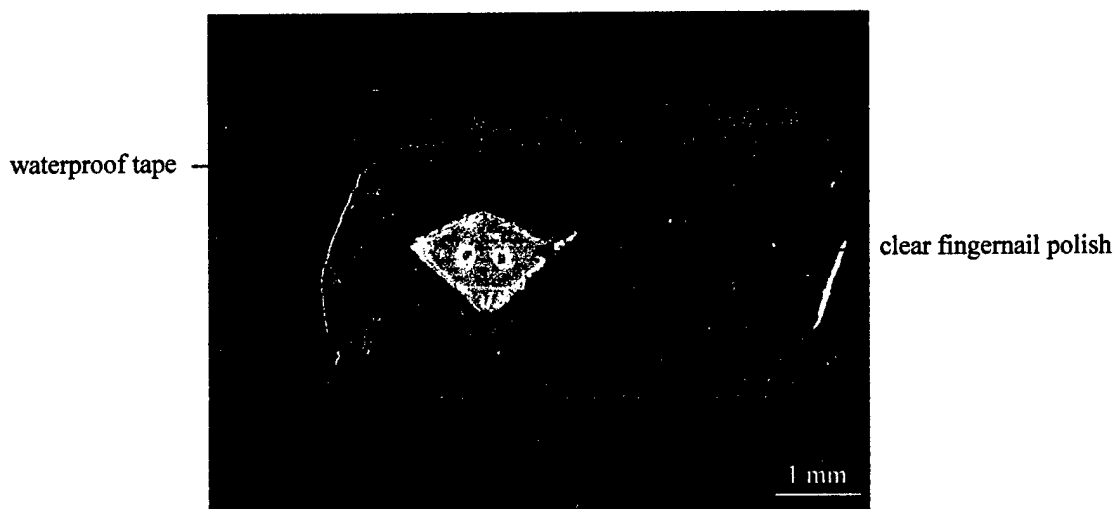


Figure 5. Gauge section of dog-bone sample with imperfect coating of clear fingernail polish.

Each sample with the flawed coating was placed in an electrochemical cell, using a saturated Calomel electrode (SCE) as the reference electrode, and a 1x1 cm platinum mesh screen electrode as the counter electrode. The dog-bone sample served as the working electrode. A special holder, as shown in Figure 6, was fabricated to hold the sample in contact with the electrolyte. The cell was placed in a Faraday cage to reduce all possible external electrical interference.

The electrolyte used in the electrochemical cell varied over the period of this investigation. Initially, 3.5 % NaCl solution was used. However, some experiments were conducted with various mixtures of hydrochloric acid (HCl), glacial acetic acid and sodium chloride (NaCl). The electrolyte used in all remaining experiments was 0.1M NaCl.

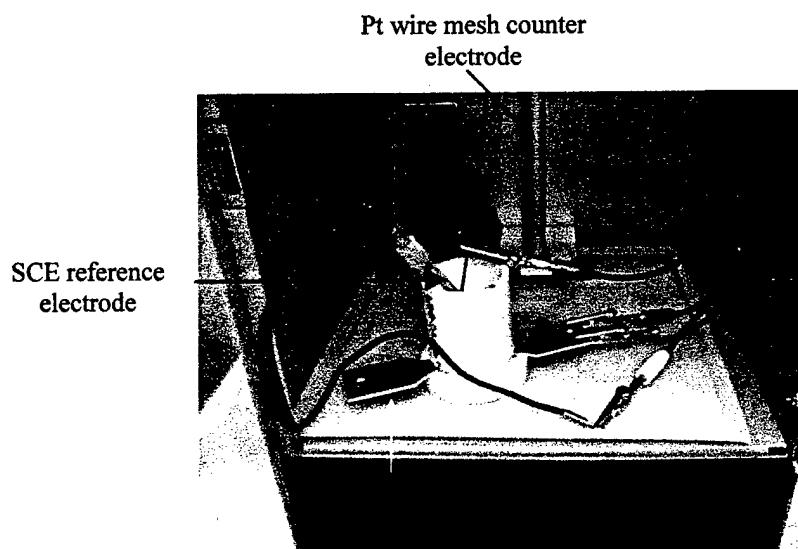


Figure 6. The electrochemical set-up used in all experiments.

Various polarization tests were conducted to create pitting corrosion on the samples. All polarization tests were conducted at laboratory temperature (20-25°C). Initially, samples were potentiodynamically and galvanostatically polarized to produce corrosion pits. The potentiostatic scans produced the best controlled pitting corrosion damage and were used in all remaining experiments. These different polarization scans will be discussed further in the following section.

All samples were then washed with distilled water. Those samples masked with fingernail polish were cleaned with acetone to remove the polish, then rinsed with distilled water. The samples were then dried thoroughly in a stream of filtered air.

3.2 INSTRUMENTATION

Various kinds of instrumentation were involved in the preparation and characterization of the samples in this investigation. This section briefly describes these instruments and their operation related to the investigation.

3.2.1 Electrochemical Equipment

The electrochemical equipment used in this study was manufactured by Gamry Instruments, Inc.¹⁵ This measuring unit was used to conduct the polarization experiments mentioned previously. After the electrodes had been properly inserted into the electrochemical cell, as shown in Figure 3, the type of polarization scan was chosen using the software package CMS 100, produced by Gamry Instruments.

As mentioned previously, several different types of scans were used during the early stages of this study. The first type of polarization scan used was an anodic potentiodynamic scan. This scan was used to determine the pitting potential for the sample. Once the pitting potential was determined, either a galvanostatic (constant current) or potentiostatic (constant potential) method was used to grow the pits. During a galvanostatic scan, the current is held constant, and potential is monitored as a function of time. After many experiments, it was found that a specific potentiostatic method produced better results in controlling the number and depth of the pits. In this type of

experiment, potential is held constant, and current is monitored as a function of time. An increased current indicates metal dissolution. For most scans used in this study, the initial potential was set above the pitting potential for several minutes. The pitting potential is the threshold potential above which pitting takes place. A final potential was then set below the pitting potential to foster the growth of the pits initiated in the first part of the scan. This step in potential is performed automatically once the parameters are set in the CMS 100 software.

3.2.2 Characterization Equipment

The pit morphology was characterized using several NDE techniques. Optical microscopy was used throughout the project to qualitatively evaluate the surface of the sample. The detailed characterization was conducted using white light interference microscopy (WLIM).

This white light surface profiler system is a non-contact optical profiler manufactured by WYKO Corporation.¹⁶ The vertical scanning interferometry (VSI) mode was used to characterize the surfaces of the Al 2024-T3 samples.

A schematic of the white light surface profiler is shown in Figure 7. In the VSI mode, an unfiltered white light beam is passed through a microscope objective to the test surface. The interferometer beam splitter reflects half of the incident beam to the reference surface within the interferometer. The light reflected from this reference surface and the test surface recombines at the beam splitter to form interference fringes. The system measures the degree of fringe modulation or coherence.

During a measurement, the reference arm containing the interferometer objective moves vertically to scan the surface at varying heights. A linearized piezoelectric transducer precisely controls the motion. White light has a short coherence length, therefore the interference fringes are only present over a very shallow depth for each focus position. The surface is in focus when the fringes are at highest contrast.

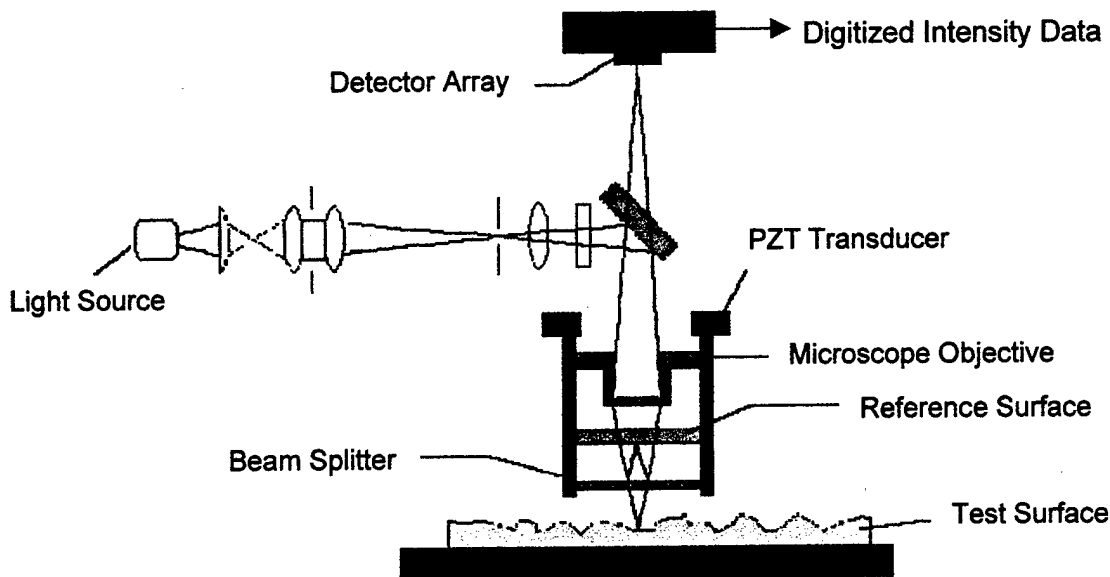


Figure 7. Schematic of the white light surface profiler.

The system scans through focus at evenly spaced intervals as the camera captures frames of interference data. As the system scans downward, an interference signal for each point on the surface is recorded. The system then uses a series of complex algorithms to decipher this data and determine a vertical position corresponding to each focused point. In this way, the pit morphology is completely characterized.

The vertical range of the VSI mode is 500 μm . This indicates that a step larger than 500 μm will produce errors when the data is deciphered. However, none of the pits in this study were deeper than 250 μm .

All profiles were taken using the highest possible resolution settings. The intensity, which controls the brightness of the unfiltered white light beam, was set slightly above saturation, so that the bottoms of the pits were sufficiently illuminated.

Three profiles of each sample were completed, and then averaged together. This reduces the effects of electronic noise and improves the repeatability and reliability of the measurements. The WLIM software, written by WYKO¹⁶, allows certain characteristics to be removed from the profile. Tilt, curvature & tilt, or cylinder & tilt can be removed from the surface profile. These eliminate the inherent sample shapes that distort or distract from the true surface features. For this study, the samples were neither curved nor cylindrical, so the latter two terms were not removed. Occasionally, the tilt would be removed from the samples that were not completely flat, so that the data could be accurately compared with the flat samples.

This technique was chosen to characterize the pit morphology because it offered fast imaging with high resolution. A typical scan takes approximately 30 to 60 seconds, and for the VSI mode, and the vertical resolution is 1 nm.

Another technique used to characterize the sample surface was scanning electron microscopy (SEM). The scanning electron microscope used in this study was an XL 30 FEG, manufactured by Philips Electron Optics.¹⁷

Image formation in the scanning electron microscope occurs at four different levels in the microscope, as shown in Figure 8. First, the electrons are emitted from an electron gun and focussed in the smallest possible virtual electron source, known as a cross-over. This cross-over beam is further demagnified in the microscope column by several condensor lenses, then the beam is focussed on the sample surface by the objective lens. When the beam of electrons interacts with the sample, different types of secondary signals escape from the sample surface. Each of these secondary signals are

detected using the appropriate detector. The signals are then converted to an electronic signal that is deciphered by the computer.¹⁸

The actual formation of a viewable image requires a scanning system to construct the image point by point over time. The signal intensity must be measured from point to point across the area of interest to produce contrast in the image. A beam deflection system is used to scan the beam across a line, and when a large number of lines are scanned together, a framed image is formed. Two pairs of electromagnetic deflection coils are used to control this process.¹⁸

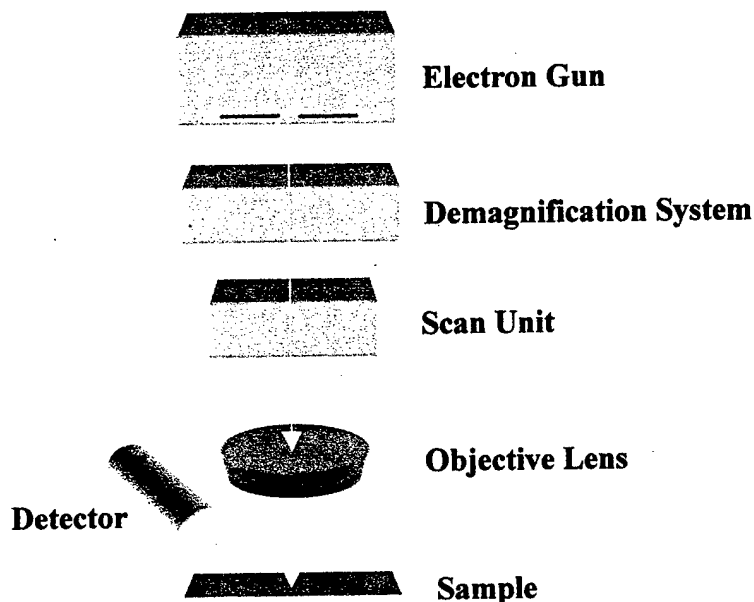


Figure 8. Schematic of image formation process in the SEM.

3.3 FATIGUE EXPERIMENT

The main objective of this investigation is to determine a correlation between an NDE parameter and a structural integrity parameter. Following the development of the accelerated controlled pitting corrosion technique, an initial experiment consisting of a series of fatigue tests was conducted on the pitted dog-bone samples to develop such a relationship.

Standard fatigue dog-bone samples were used for this study. Forty-four samples were fabricated from Al 2024-T3 sheet with the tensile axis parallel to the rolling direction. The dimensions for the dog-bone specimens are shown in Figure 9.

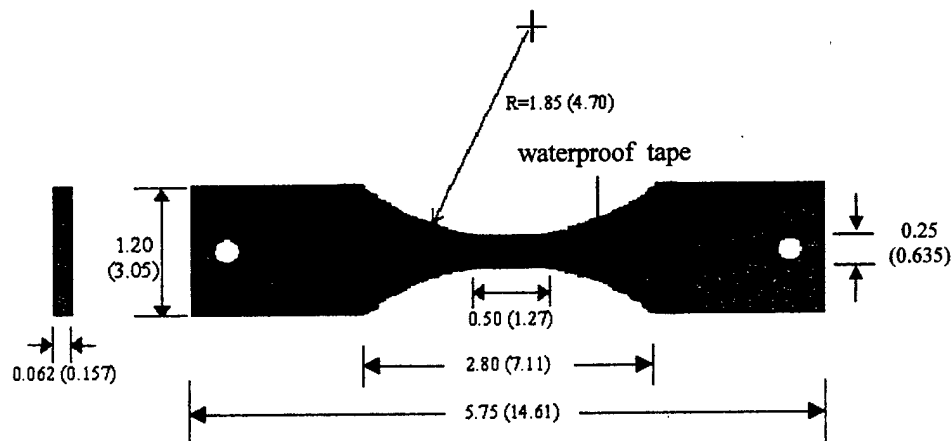


Figure 9. Geometry of dog-bone fatigue sample made of Al 2024-T3. Primary dimensions are in inches, and dimensions in parentheses are in cm.

The samples were cleaned and prepared one at a time using the method previously described in section 3.1. The details of the polarization test conditions for the samples are illustrated in Table 1. Four specimens were allocated for each set of conditions to

account for the inherent variance in corrosion and fatigue data. As the test matrix shows, the exposed area of the gauge section was either masked with the clear fingernail polish or left bare. For those samples with the clear fingernail polish, only two imperfections were introduced into the polish before it completely dried. After the polish had dried for approximately 10 minutes, the sample was glued into the electrochemical cell as shown in Figure 6 and allowed to dry for 1 hour.

After the glue had dried, the cell was filled with 5-10 milliliters of 0.1 M NaCl. Four of the samples were immersed in the 0.1 M NaCl solution for a period of 2 weeks. All other samples were subjected to the same potentiostatic scheme. The initial potential was set at -450mV (vs. SCE) for 10 minutes. Then the potential was changed to -520 mV (vs. SCE) for the remainder of the experiment. The length of polarization for each sample is shown in Table 1.

The sample was promptly removed from the electrochemical cell after the pitting experiment and dried in a stream of air. The pit morphology and pit depth measurements were determined using optical microscopy, SEM and WLIM. The samples were then fatigued within 24 hours of being removed from the electrochemical cell.

All the fatigue tests were conducted using the same machine. The machine is a servo-hydraulic system utilizing hydraulic grips and precision alignment. All fatigue tests were conducted in laboratory air under the same conditions at a stress ratio of 0.1, maximum stress of 256 MPa and a frequency of 15 Hz.

Table 1

Test matrix for the electrochemically pitted fatigue samples. Polarization time refers to the length of time the sample was corroded.

Set number	Sample Number	Fingernail polish applied?	Time Immersed	Polarization Time (hrs)
1	1	No	0	0
	2	No	0	0
	3	No	0	0
	4	No	0	0
2	5	Yes	2 weeks	0
	6	Yes	2 weeks	0
	7	Yes	2 weeks	0
	8	Yes	2 weeks	0
3	9	No	0	4
	10	No	0	4
	11	No	0	4
	12	No	0	4
4	13	No	0	8
	14	No	0	8
	15	No	0	8
	16	No	0	8
5	17	No	0	12
	18	No	0	12
	19	No	0	12
	20	No	0	12
6	21	Yes	0	4
	22	Yes	0	4
	23	Yes	0	4
	24	Yes	0	4
7	25	Yes	0	8
	26	Yes	0	8
	27	Yes	0	8
	28	Yes	0	8
8	29	Yes	0	12
	30	Yes	0	12
	31	Yes	0	12
	32	Yes	0	12
9	33	Yes	0	16
	34	Yes	0	16
	35	Yes	0	16
	36	Yes	0	16
10	37	Yes	0	20
	38	Yes	0	20
	39	Yes	0	20
	40	Yes	0	20
11	41	Yes	0	24
	42	Yes	0	24
	43	Yes	0	24
	44	Yes	0	24

CHAPTER 4

RESULTS AND DISCUSSION

4.1 DEVELOPMENT OF ACCELERATED CONTROLLED PITTING TECHNIQUE

4.1.1 Chemical Techniques

A method for creating accelerated controlled pitting was developed as the first goal of this study. All tested samples were made of Al 2024-T3. This alloy is one of the main airframe materials and comprises over 50% of most aircraft structures.⁶ Table 2 lists the elements present in this aluminum alloy.

Table 2
Chemical composition limits for aluminum alloy 2024-T3.¹⁹

Element	Cu	Mg	Mn	Si	Fe	Zn	Cr	Al
%	3.8-4.9	1.2-1.8	0.3-0.9	0.5	.05	0.25	0.1	remainder

Initially, conventional chemical techniques were investigated to create pitting corrosion. Regular and alternate immersion tests were conducted in a large variety of aggressive environments including CASS solution²⁰ to selectively grow deep pits. External heating up to 150 °F and mechanical stirring were also used to accelerate the kinetics of pitting corrosion. General corrosion or high density pitting was the main outcome of these types of experiments. This general corrosion was the result of the formation of numerous small shallow pits over the entire exposed surface. Such shallow

surface pitting is caused by the alloying elements present in the aluminum matrix. As seen in Table 2, a significant percentage of copper is present in Al 2024-T3. The cathodic behavior of copper in the presence of aluminum results in pitting corrosion over the exposed surface. This process was discussed in Chapter 2. The CASS solution produced the most adverse conditions, and resulted a few pits measuring approximately 200 μm . The pitting generated by these chemical methods was very difficult to reproduce.

The chemical techniques also required a substantial amount of time to produce pits with minimum depths of 100 μm . In some cases, the samples were left in a 97% humidity chamber for up to one month to create these deep pits. It was concluded that these chemical techniques required too much time, and did not produce the deep pits that were needed for the fatigue experiment. Therefore, several kinds of polarization techniques were investigated to accelerate the pitting process, and create deeper, more selective pitting.

4.1.2 Polarization Techniques

Various polarization schemes were used in an attempt to control the number and depths of the pits produced. Anodic polarization techniques were investigated because it was thought that the time needed to create the desired pitting corrosion would be much less than the time required for the chemical techniques. An explanation of anodic polarization schemes begins with the anodic and cathodic reactions of a corrosion process. These reactions are known to proceed at a finite rate under open circuit conditions, and if a set voltage is applied to the system, the rates of the corrosion redox reactions will change. This is shown in Figure 10. Figure 10 is an Evan's Diagram of a corrosion process. An Evan's Diagram is a plot of potential versus current density. E_{equil} is the equilibrium potential. If a positive potential is imposed on the metal, the rate of the oxidation reactions will increase, and the rate of the reduction reactions will decrease. Therefore, the rate of the oxidation reaction that dissolves the metal substrate will increase causing the corrosion process to accelerate with respect to its equilibrium rate.

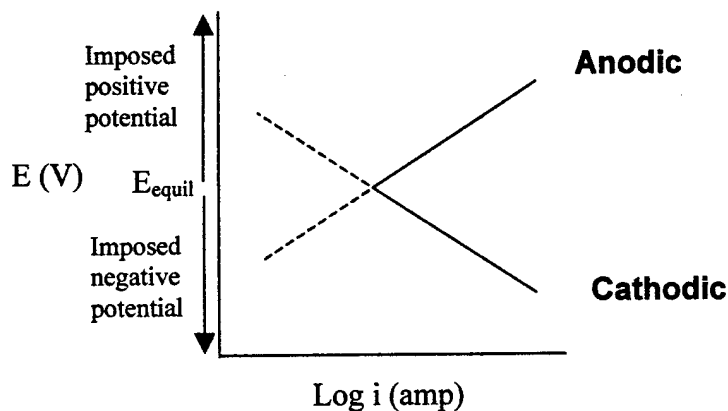


Figure 10. Evan's Diagram.

Initially, small bare coupons of Al 2024-T3 were placed in electrochemical cells using 3.5 % NaCl as an electrolyte. This concentration of NaCl closely represents the concentration of salt in ocean water. The term "bare" refers to the surface of the coupon which does not have any kind of external coating on it. The first polarization scheme used to create pitting corrosion was a potentiodynamic experiment. A representative plot is shown in Figure 11. Current is monitored as a function of potential. The potential increases at a user defined rate, such as one mV/sec, and the current is recorded as the potential changes. In this region, the sample surface is protected by the passive aluminum oxide film, preventing any corrosion. The measured current that is required to maintain this passive film is known as i_{pass} . The sudden increase in current at the top of the plot is indicative of the initiation of pitting corrosion. The potential at which this increase occurs is known as the pitting potential. The rise in current is representative of the increase in flow of electrons from the anode to the cathode. This part of the pitting process discussed in section 2.1.

A large number of experiments using this type of anodic polarization were conducted with various concentrations of NaCl. The potential scan rate and hold time above the pitting potential were also varied to better control the pitting process. All of these experiments resulted in numerous small and shallow pits on the specimen surface like those created by the chemical techniques mentioned in section 3.1, and there was little control over the depth and distribution of the pits. However, the amount of time needed to produce these pits was less than 24 hours, compared to the weeks or months required for the chemical techniques.⁶

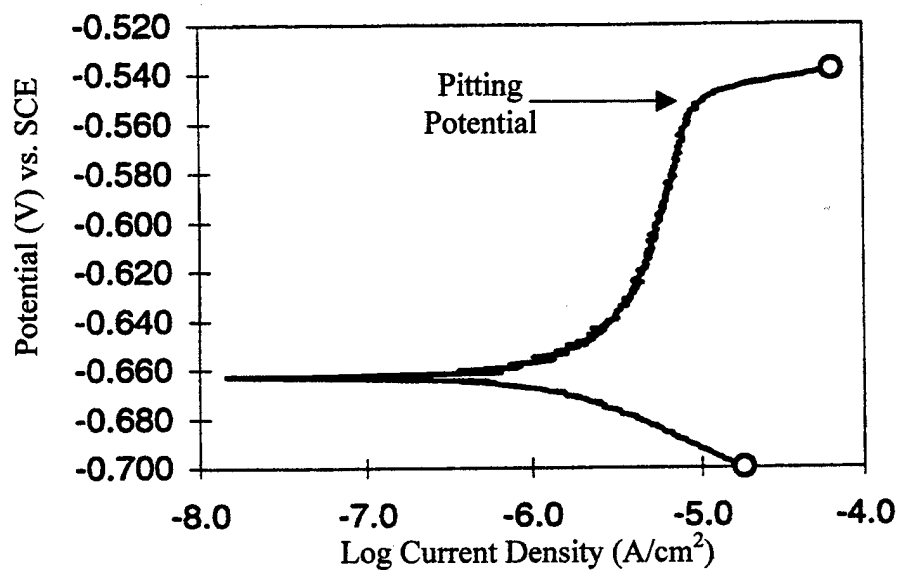


Figure 11. Potentiodynamic plot showing behavior of Al 2024-T3.⁶ SCE refers to the saturated Calomel reference electrode.

The next polarization experiment explored was a galvanostatic scheme. In a galvanostatic experiment, the current is held constant and potential is monitored as a function of time. The value for the current is defined by the user. A representative galvanostatic plot is shown in Figure 12. The initial experiments were run with lower currents starting at 2 μA . The current was raised in following experiments up to 100 μA . All of these experiments produced results similar to the potentiodynamic experiments. The higher current resulted in a high density of pits instead of a few deep pits, and again, there was no control on the depth or number of pits produced.

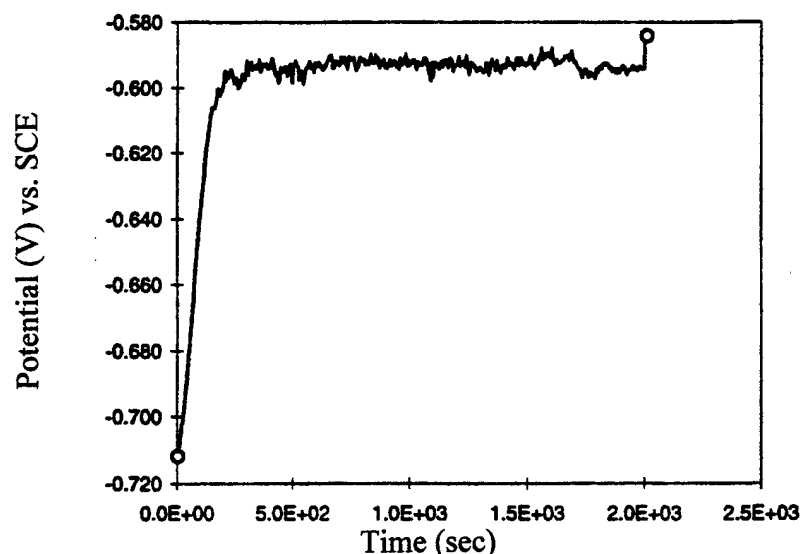


Figure 12. A representative galvanostatic plot used to create pits on Al 2024-T3 sample.⁶

A final attempt was made to control the pitting process using a potentiostatic scheme. In this method, the potential is held constant, and the current is monitored as a function of time. Figure 13 shows a representative plot of this type of anodic polarization technique. For the first five hours, the current remains very low. No pitting takes place during this induction period. The length of the induction period varies widely between samples. After this period, the current increases rapidly, indicating the initiation of pitting. The current then decreases, showing that some of the pits passivated, or stopped growing.

The potential for this kind of scan is set by the user. The user also has the option to change the potential during the experiment, such as stepping from a high potential to a lower potential part way through the experiment. For example, the first few minutes of the scan could be set at a high potential to initiate a few pits. After this time, the potential could be set at a lower value to foster the growth of the pits initiated in the first few minutes. In addition, the reduction in potential helps prevent new pits from initiating in

the latter part of the experiment. This aids in controlling the pitting process. This two-step process produces pitting much more quickly than waiting for an induction period of an undetermined length. After several experiments, however, the method was abandoned because the pit depth and distribution could not be adequately controlled.

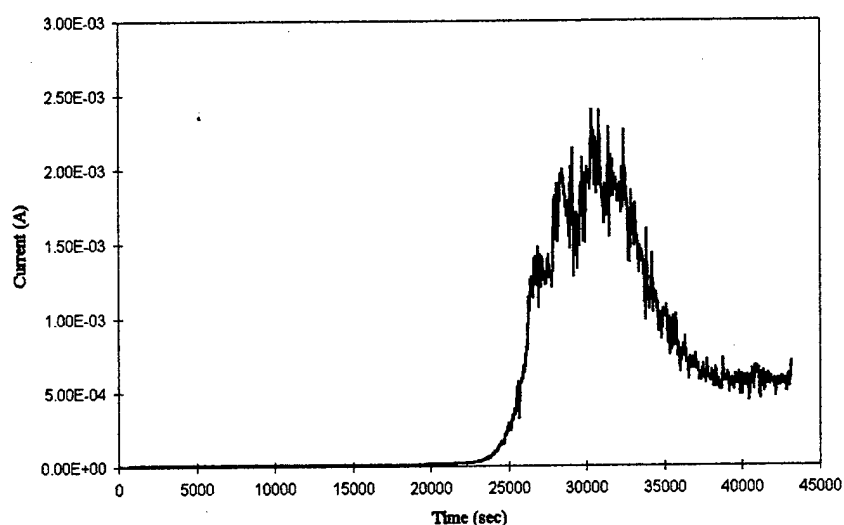


Figure 13. Potentiodynamic plot used to create pits on Al 2024-T3 sample.

After exploring all of these methods, it became obvious that the presence of numerous precipitates in the alloy was responsible for initiating a large number of surface pits as seen with the chemical techniques. No electrochemical or chemical method seemed to preferentially excite a small number of nucleation sites and maintain the growth of the subsequent pit. A method was devised to reduce the number of initiation sites exposed to the electrolyte in order to decrease the amount of shallow pitting.

This work was initially conducted at the In-House Coating and Corrosion Prevention Group at the Material Directorate at Wright Patterson Air Force Base (WPAFB). Corrosion inhibiting sol-gel films were being developed by this coatings group at Wright Labs on WPAFB. The study showed that pits mainly initiated at cracks or pores in the sol-gel film.²¹ The sol-gel layer acted as a protective barrier and restricted

the number of nucleation sites exposed to the electrolyte. An optical micrograph of the surface of a vinyl-silane sol-gel coated sample is shown in Figure 14. The sol-gel layer has a grain-like structure clearly seen in Figure 14, which allowed only the small sections of the aluminum surface to be exposed to the electrolyte. This prompted the next series of experiments to be conducted with Al 2024-T3 specimens coated with a 200 μm thick vinyl-silane sol-gel coating. The initial electrolyte used was 3.5% NaCl.

The sol-gel coated samples were subjected to the same polarization scheme mentioned previously. After many experiments, the potentiostatic polarization scheme was found to produce better results in controlling the number and depth of the pits. Initially, various potentials above the pitting potential were investigated. Different hold times at these potentials were tried to better control the pitting, as the depths of the pits depend on the hold time above the pitting potential.

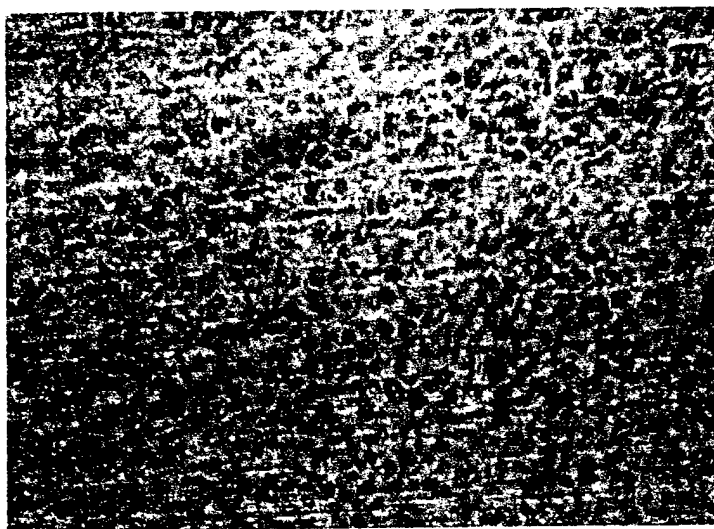


Figure 14. Optical micrograph of the top surface of a vinyl-silane sol-gel film.

The electrolyte was also varied to obtain a better control on the pitting process. The 3.5% concentration of NaCl was too aggressive causing high density pitting on the sample surface. The concentration was reduced in following experiments to 0.1M NaCl.

This dilute concentration produced the best controlled pitting in conjunction with the potentiostatic scheme, and was used in all subsequent experiments.

Standard fatigue dog-bone samples were used after confidence was gained with this technique. The most difficult part of this method development was determining the lengths of the potentiostatic scans, and the potentials at which to conduct the scans. Using the same potentiostatic scheme for two samples does not guarantee similar pit morphology for Al 2024-T3 due to the complex nature of this alloy. Figure 15 shows several micrographs of pitted sol-gel coated dog-bone samples. The pits were created using the potentiostatic scheme described previously. The shiny appearance of the metal surface is due to the transparent sol-gel coating on the surface. Figure 15(d) shows the waterproof tape that is used to mask most of the sample, except for a small portion of the gauge section.

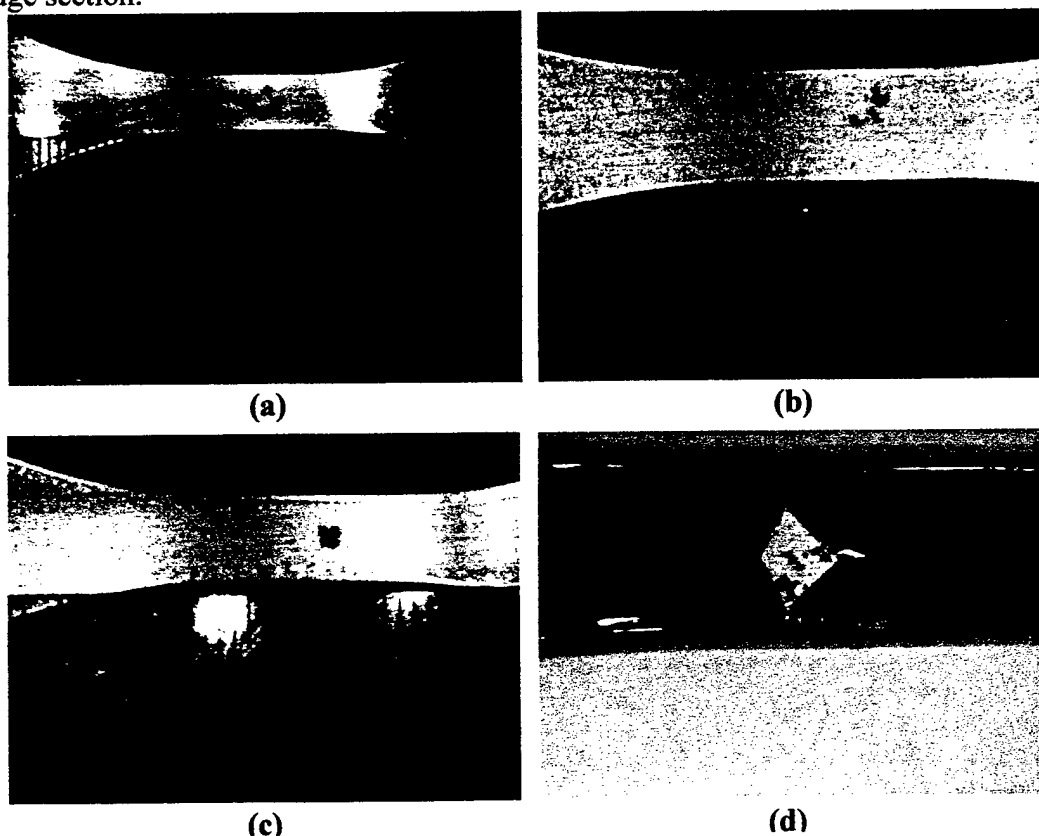


Figure 15. (a)-(c) Optical micrographs of sol-gel coated pitted dog-bone samples at different magnifications (d) Sol-gel coated pitted dog-bone sample covered with waterproof tape.

A problem was encountered with the use of the sol-gel. It could not be removed from the sample without destroying the pitted surface because the sol-gel chemically bonded with the aluminum substrate. It was necessary that the sol-gel should be removed for further surface characterization. Therefore, a clear fingernail polish was used instead to mask the gauge section of the dog-bone samples. This polish could be easily removed after the pits were created.

The nail polish could be easily removed with a small amount of acetone after the sample was pitted. After several scans, it was found that the nail polish did not crack like the sol-gel, and longer potentiostatic scans were required to create the desired pitting. This problem was resolved by introducing several small flaws into the nail polish using the tip of a needle before the sample was polarized. Special care was taken not to scratch the metal surface underneath the polish.

4.1.3 Characterization Techniques

Optical microscopy, scanning electron microscopy and white light interference microscopy were the techniques used in this study to characterize the pitted sample surface. Figures 16 and 17 show optical micrographs of two samples that were pitted using the potentiostatic scheme described in section 4.1.2.

Three tiny holes were made in the nail polish before the sample was polarized. Three pits were initiated and grown to the desired size using a specific potentiostatic scan, as seen in Figures 16 and 17. The sample shown in Figure 16 was polarized twice over a 24-hour period. The first scan lasted one hour, and several small pits were initiated on the surface in the vicinity of the three imperfections. A second, longer polarization scan was used to grow only a few of the initiated pits. A lower potential of approximately -525mV (vs. SCE) was used in the second scan to restrict the initiation of new pits and ensure the growth of the pits started in the first polarization scan.



Figure 16. First optical micrograph of pitted dog-bone sample.

The sample shown in Figure 17 was also polarized twice within 24 hours. The first scan was run for one hour at a single potential. The second scan differed from the one described for the sample in Figure 16 because the potential was varied within the same scan. For the first hour of the eleven hour scan, the potential was set at -450 mV vs. SCE. After this hour, the potential decreased automatically to -475 mV vs. SCE for the remaining 10 hours.

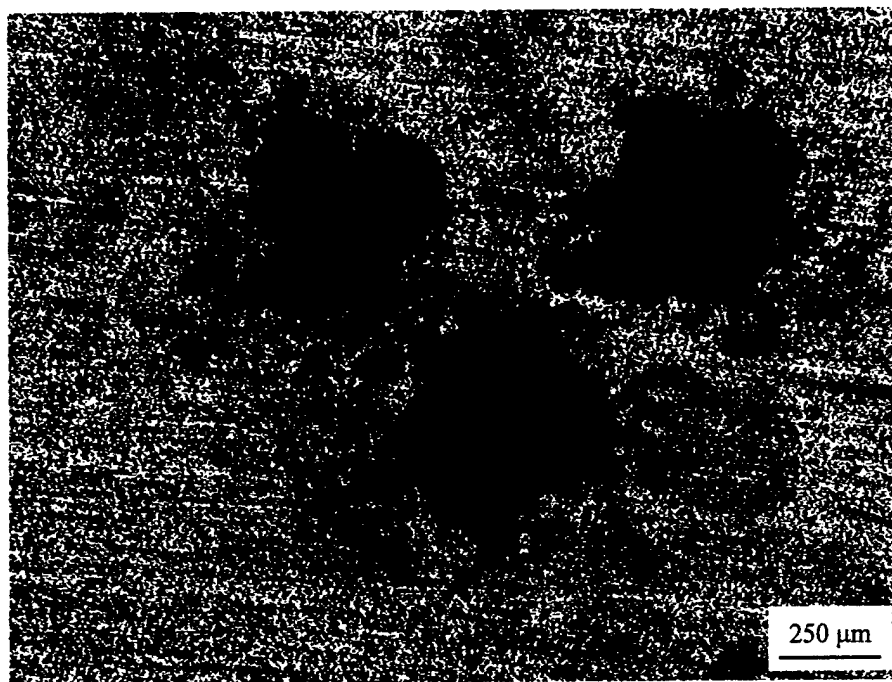
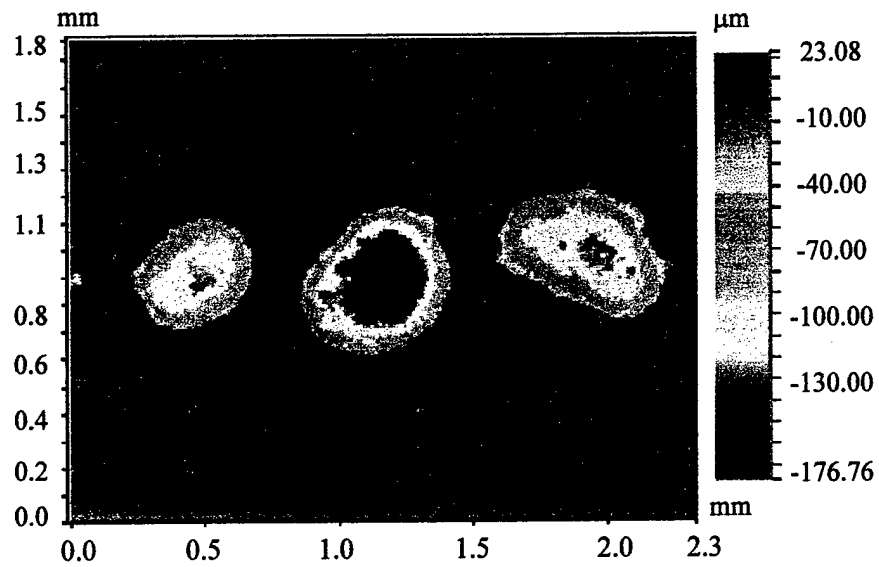


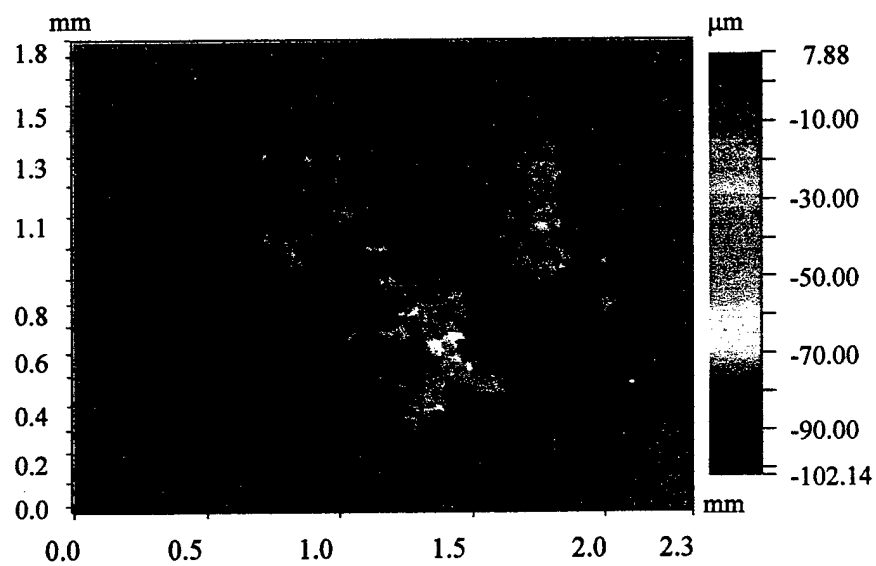
Figure 17. Second optical micrograph of pitted dog-bone sample.

An optical micrograph only offers qualitative information about the surface features of a pitted sample. No quantitative data, such as pit depth, can be accurately determined from such an optical micrograph. Therefore, white light interference microscopy (WLIM) was used to fully characterize the pitted sample surface.

Figure 18(a) shows the surface profile for the sample illustrated in Figure 16, and Figure 18(b) is the surface profile of the sample shown in Figure 17.



(a)



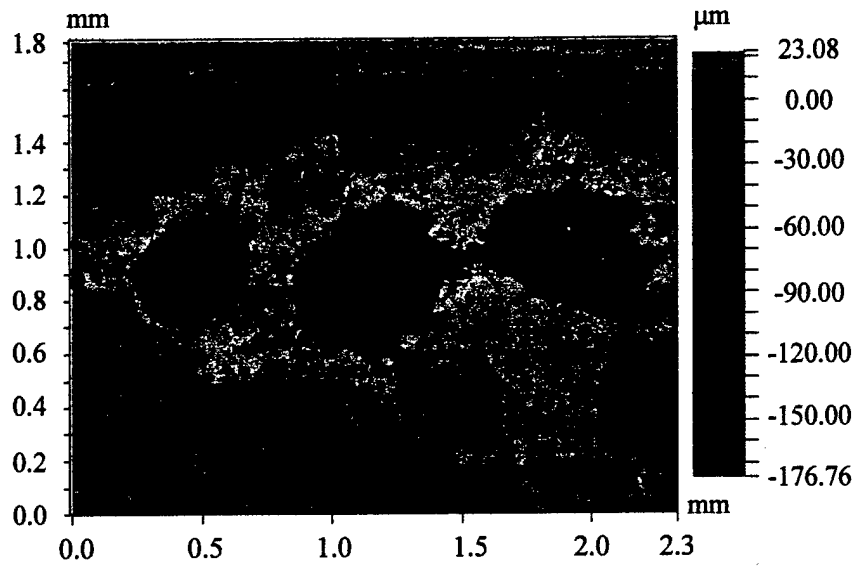
(b)

Figure 18. (a) WLIM surface profile of sample shown in Figure 16. (b) WLIM surface profile of sample shown in Figure 17.

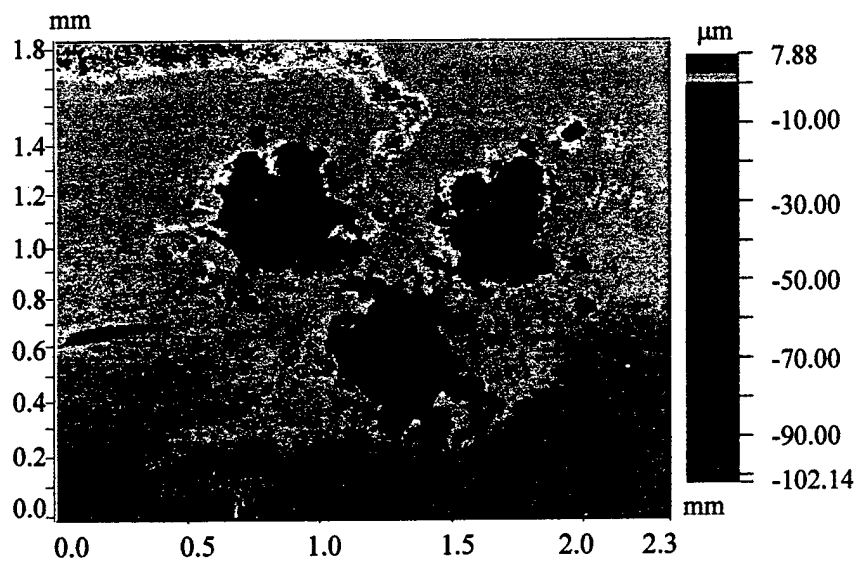
The color scale at the right indicates the various depths of the pits. The WLIM method gives quantitative information, unlike the optical micrograph, because a color scale is used to show depth

Another type of WLIM surface profile used in this study was the maximum contrast profile. This type of profile was used to view the shallow surface features of the sample, since they are not displayed well with the surface profiles shown in Figure 18. The maximum contrast surface profiles corresponding to Figure 18 are shown in Figure 19. As can be seen, the color scale is manipulated to bring out the contrast in surface morphology. These profiles were used to look at the shallow surface features and not to determine depth. When Figure 19 (a) is compared to Figure 16 and Figure 19(b) is compared to Figure 17, a better resemblance in pit shape was seen compared to the surface profiles shown in Figure 18. The shallow surface features were more pronounced in the maximum contrast profiles due to the rearrangement of the color scale.

Three-dimensional models of the pitted surfaces were also generated to obtain detailed information about the pit morphology. The three-dimensional images corresponding to the samples shown in Figures 16 and 17 are represented in Figures 20 (a) and (b), respectively. The data has been inverted, so the pits look like mountains instead of valleys. Only the pit mouth can be seen before the data is inverted. Therefore, inverting the data allows the pit morphology to be viewed from a much better perspective. In addition, the software package that runs the equipment provides the means to rotate the three-dimensional image in many directions. This allowed the shape of each pit to be viewed from many different angles.

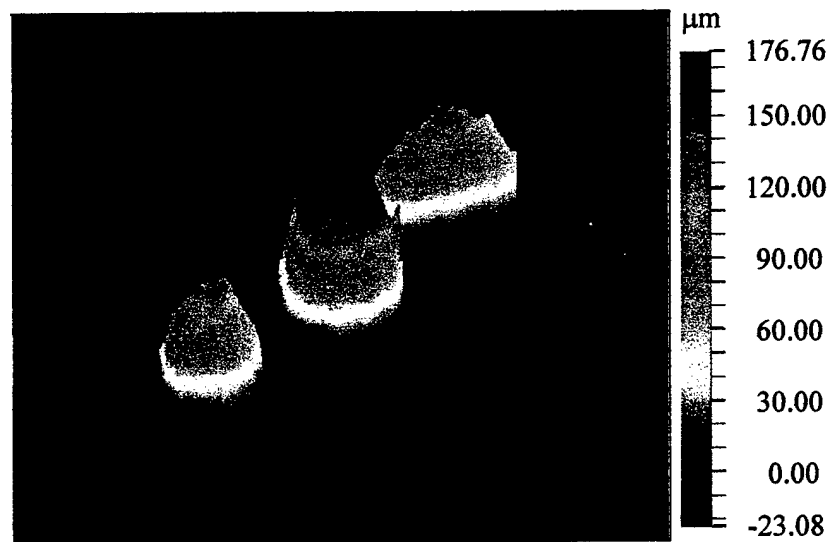


(a)

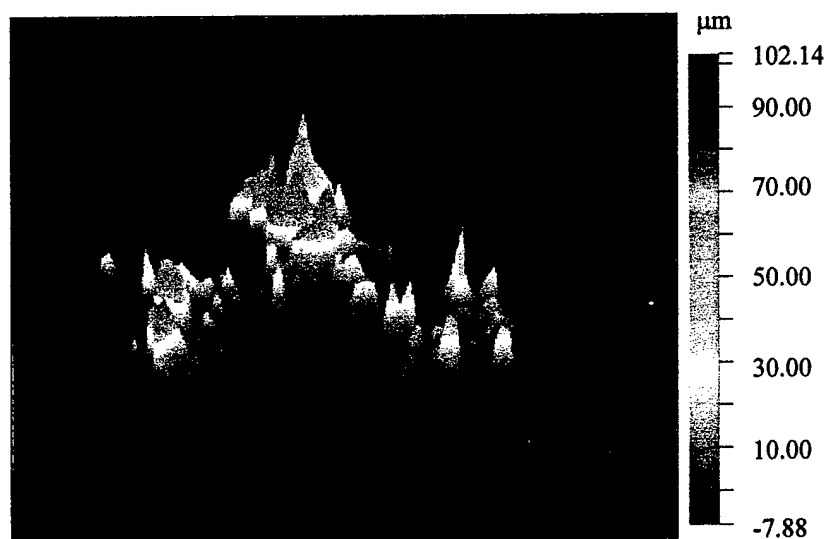


(b)

Figure 19. (a) WLIM maximum contrast profile of sample shown in Figure 16 and 18(a). (b) WLIM maximum contrast profile of sample shown in Figure 17 and 18(b).



(a)



(b)

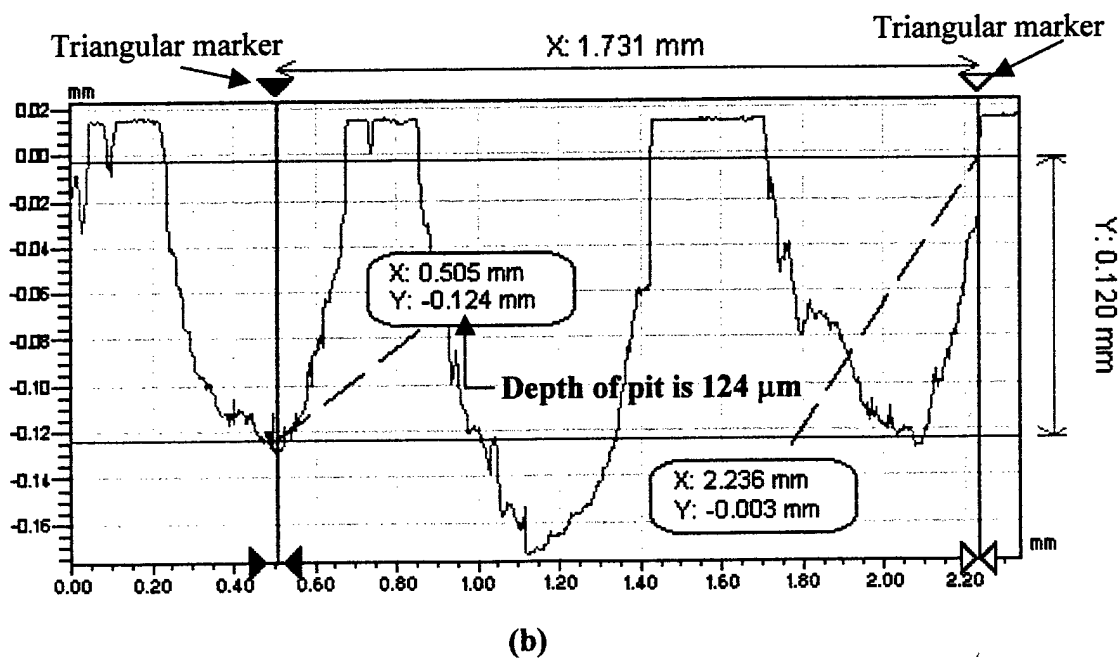
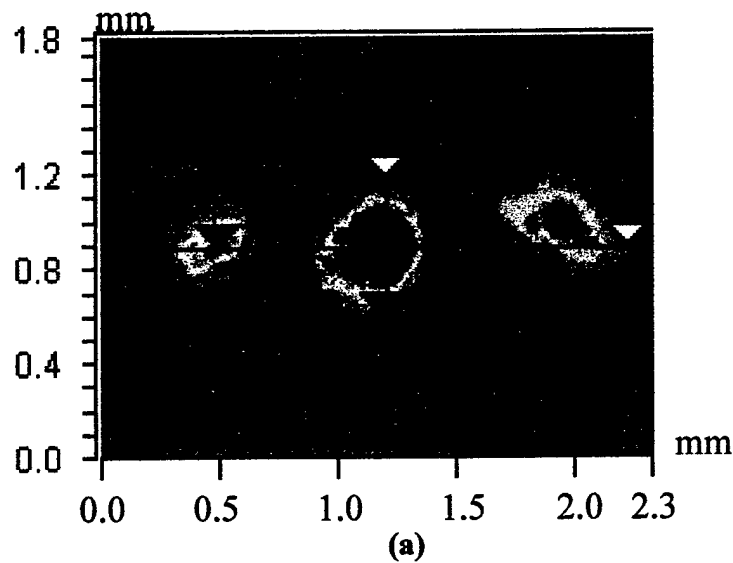
Figure 20. (a) WLIM 3-dimensional profile of sample shown in Figures 16, 18(a) and 19(a). (b) WLIM 3-dimensional profile of sample shown in Figure 17, 18(b) and 19(b)

Specific pit parameters, such as pit depth and diameter, were required in the analysis for the fatigue study mentioned in Chapter 3. All previous WLIM profiles provided only general information about the pitted surface. For example, the deepest point in Figure 17(b) is 120 μm , but it was difficult to determine exactly where this point was located on the profile. Therefore, a two-dimensional analysis was performed to more exactly determine these pit parameters.

Figure 21 illustrates this two-dimensional analysis. Figure 21(a) is the surface profile shown in Figure 18(a). The horizontal and vertical crossbars on Figure 21(a) are used in conjunction with Figures 18(b) and (c). The red horizontal crossbar in Figure 21(a) corresponds to the X profile shown in Figure 21(b). This red crossbar can be moved up and down over the entire surface of the profile. This allows the entire two-dimensional surface profile to be viewed in the X direction. The black and white triangular markers on Figure 21(a) correspond to those on the X profile in Figure 21(b). These triangular markers can be moved right or left across the entire X profile shown in Figure 21(b), and the exact X and Y coordinates of each point appear in the balloon attached to the marker. Figure 21(b) illustrates how the depth of a pit is exactly determined. The marker is moved to the bottom of the pit, and the exact Y coordinate is automatically given. Therefore, Figure 21(b) shows that the depth of the left pit at that particular point is 124 μm .

The Y profile shown in Figure 21(c) corresponds to the blue vertical line shown in Figure 21(a). The Y profile was used in the same manner as the X profile described above. Figure 21(c) illustrates how the diameter of a pit is accurately determined. One marker is moved to the left side of the pit mouth, and the other marker is moved to the

right side of the pit mouth. The distance between these two points is automatically calculated and was found to be 597 μm at that point. Using this accurate WLIM two-dimensional analysis, the pit parameters required for the analysis of fatigue data were determined non-destructively.



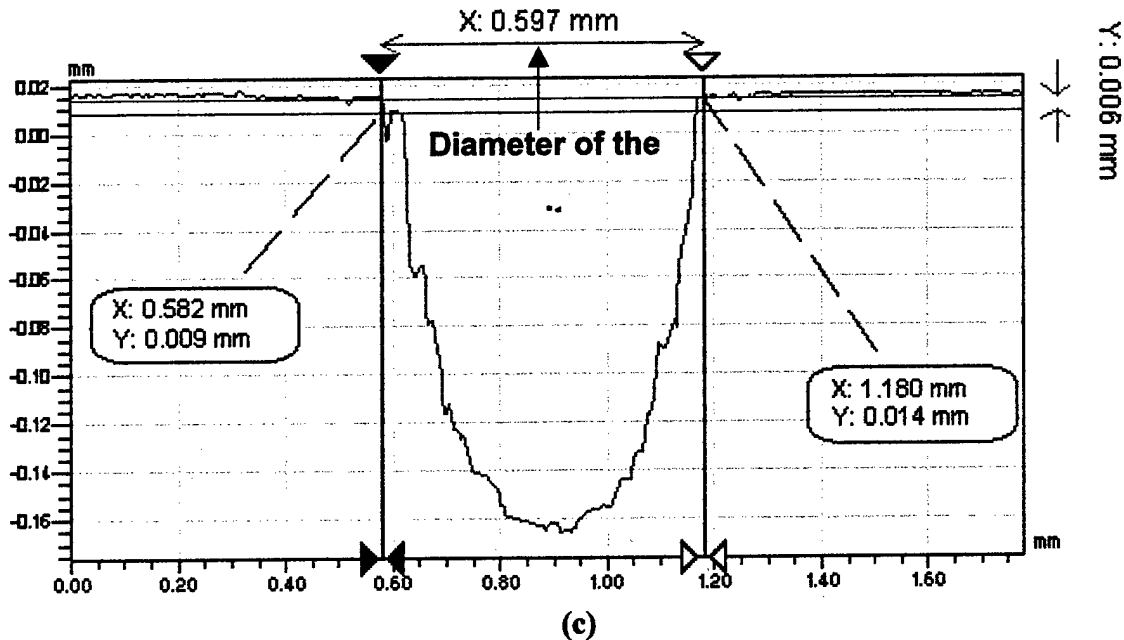


Figure 21. (a) Surface profile used in two-dimensional analysis. (b) X profile in two-dimensional analysis illustrating the determination of pit depth. (c) Y profile in two-dimensional analysis illustrating the determination of pit diameter.

Often, a closer inspection of a specific area of the surface profile is required. This is done by obtaining a subregion of the area in question. This option of creating a subregion is very useful for obtaining minute details of specific areas of the pitted surface that cannot be seen on the overall profile. Figure 22 illustrates the center pit as a subregion of the surface profile shown in Figure 18(a).

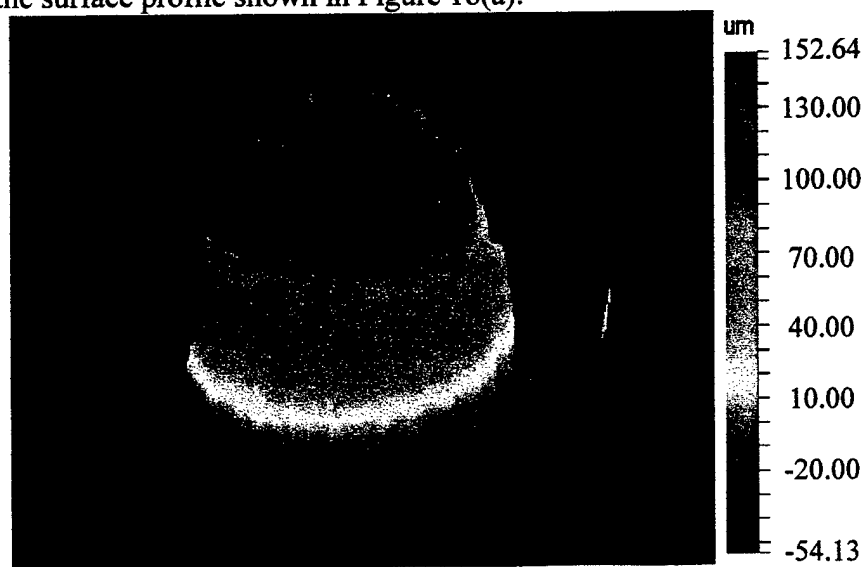


Figure 22. Center pit as a subregion of the surface profile shown in Figure 18(a).

In addition to the profiles shown previously, the WLIM software is capable of calculating other parameters. Several quantitative pitting parameters were of interest for this project because they are required to complete the fatigue analysis. These parameters include root-mean-square (rms) roughness, average roughness, average pit depth, deepest point and total pit volume.

The average roughness is the mean height as calculated over the entire measured array. Mathematically, it is the arithmetic average of the absolute values of the measured height deviations taken within the evaluation length or area and measured from the mean line of surface. The average roughness is a useful parameter for detecting general variations in the overall profile height characteristics of the surface. The average roughness cannot detect differences in spacing or the presence or absence of infrequently occurring high peaks and deep valleys. These irregularities will be averaged out and will result in only a small influence on the final roughness value.²²

The rms roughness is obtained by squaring each value over the evaluation length or area, then taking the square root of the mean. Compared with average roughness, rms roughness has the effect of giving extra weight to the higher values.

The total pit volume was calculated using the volume profile provided by the WLIM software. The total pit volume is estimated as the space between a surface and a plane parallel to the reference plane of the surface. This volume parameter can be visualized as the volume of liquid the surface must hold to be completely submerged, as shown in Figure 23.

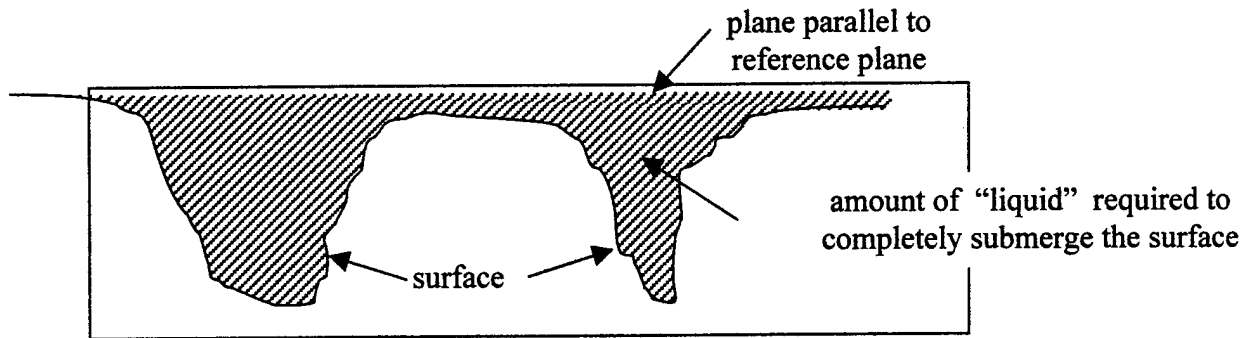


Figure 23. Illustration of volume calculation.

The actual volume calculation is determined using an interactive volume profile, such as the one shown in Figure 24. The position of the plane parallel to the reference plane is adjusted using the scale at the right of the surface profile. The initial position of this plane is at the highest point on the surface. The surface is masked as the position of this plane is lowered. The background appears black because most of this flat surface is masked so that a better pit volume can be measured. The volume is automatically calculated and displayed in the box below the profile.

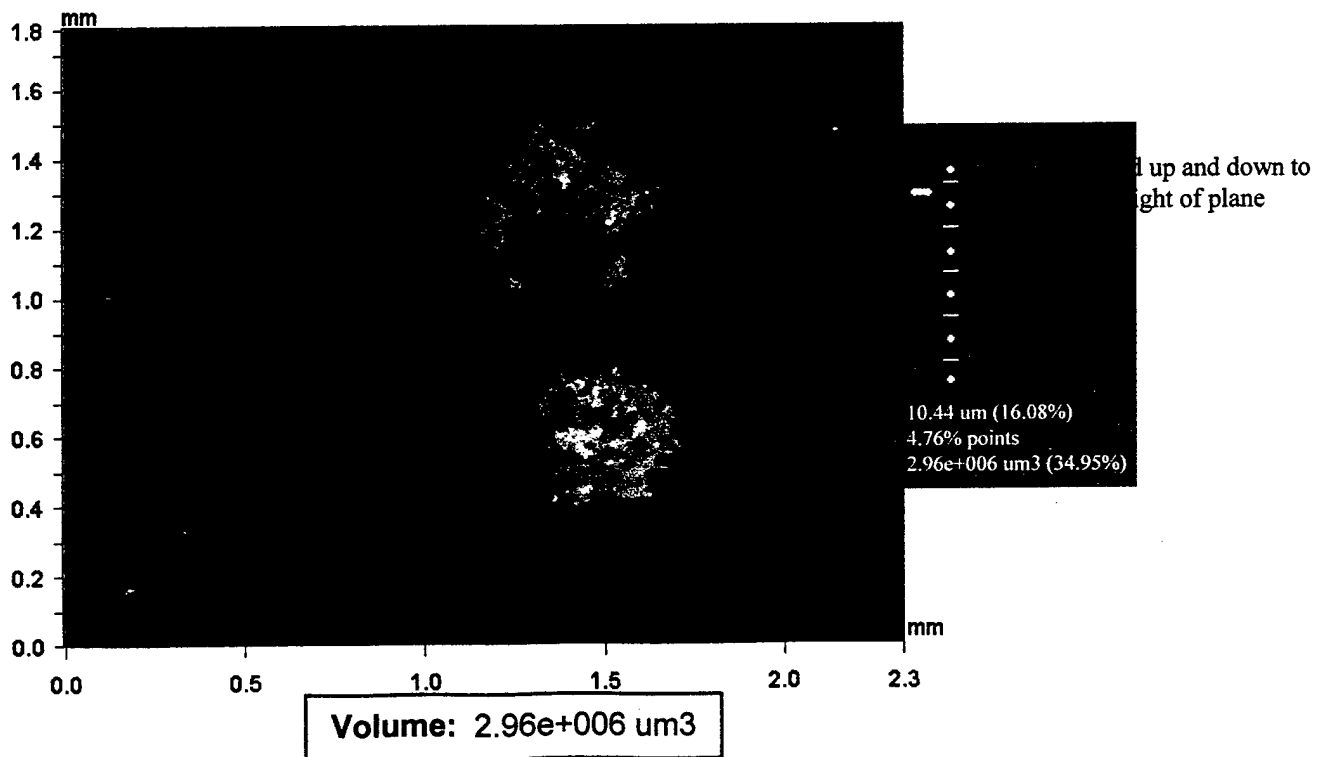


Figure 24. Interactive volume profile used to determine total pit volume.

The amount of total material lost due to the pitting was then calculated. The pit volume was multiplied by the density of Al 2024-T3, which provided the total amount of metal that was dissolved during the pitting process.

4.2 FATIGUE EXPERIMENT AND RESULTS

This section explains the results from the fatigue experiment described in section 3.3 in Chapter 3. Clayton L. Harmsworth in 1961.²³ had conducted a fatigue study to determine the effect of corrosion pitting on the fatigue behavior of Al 2024-T4 and to establish a method of measuring pitting corrosion damage with respect to fatigue. Harmsworth found surface roughness measurements to be a useful indication of the expected fatigue life of a corroded structural member of Al 2024-T4.

There were some differences between Harmsworth's study and this MURI project. The heat treatments for the metal of interest were slightly different, with Harmsworth's samples having a T4 treatment and this project's heat treatment being T3. A rotating beam configuration was used for the dog-bone samples in the 1961 study, and the samples made for this investigation were of the tensile configuration. In addition, this is only the first set of samples to be run for the MURI study, so only preliminary results have been reported.

4.2.1 Production of Pits

The test matrix shown in Table 1 in Chapter 3 was designed to generate a wide range of pit sizes and depths. The use of the polarization scheme allowed a wide range of pit sizes to be produced in a relatively short amount of time. Figures 25 and 26 show optical micrographs of a representative sample from each of the nine sets that were subjected to an anodic polarization scheme (see Chapter 3, Table 1).

Figure 25 shows examples from the three sets of samples that were anodically polarized without the fingernail polish coating on the surface. As the optical micrographs show, the surfaces are covered with numerous shallow pits. Very few deep pits were observed because there were too many active sites on the surface exposed to the electrolyte.

Figure 26 shows examples from the other six sets of samples that were anodically polarized with the substrate coated with the imperfect layer of fingernail polish. A large difference in the pitting distribution can be seen when comparing the micrographs in Figures 25 and 26. The polarization times range from four hours to twenty-four hours for the six samples shown in Figure 26. The pits are much deeper and there are only two on the sample surface. For longer polarization times, larger and deeper pits were obtained. As a result, the mixture of bare and fingernail polish coated samples provided a wide range of pit sizes and distributions.

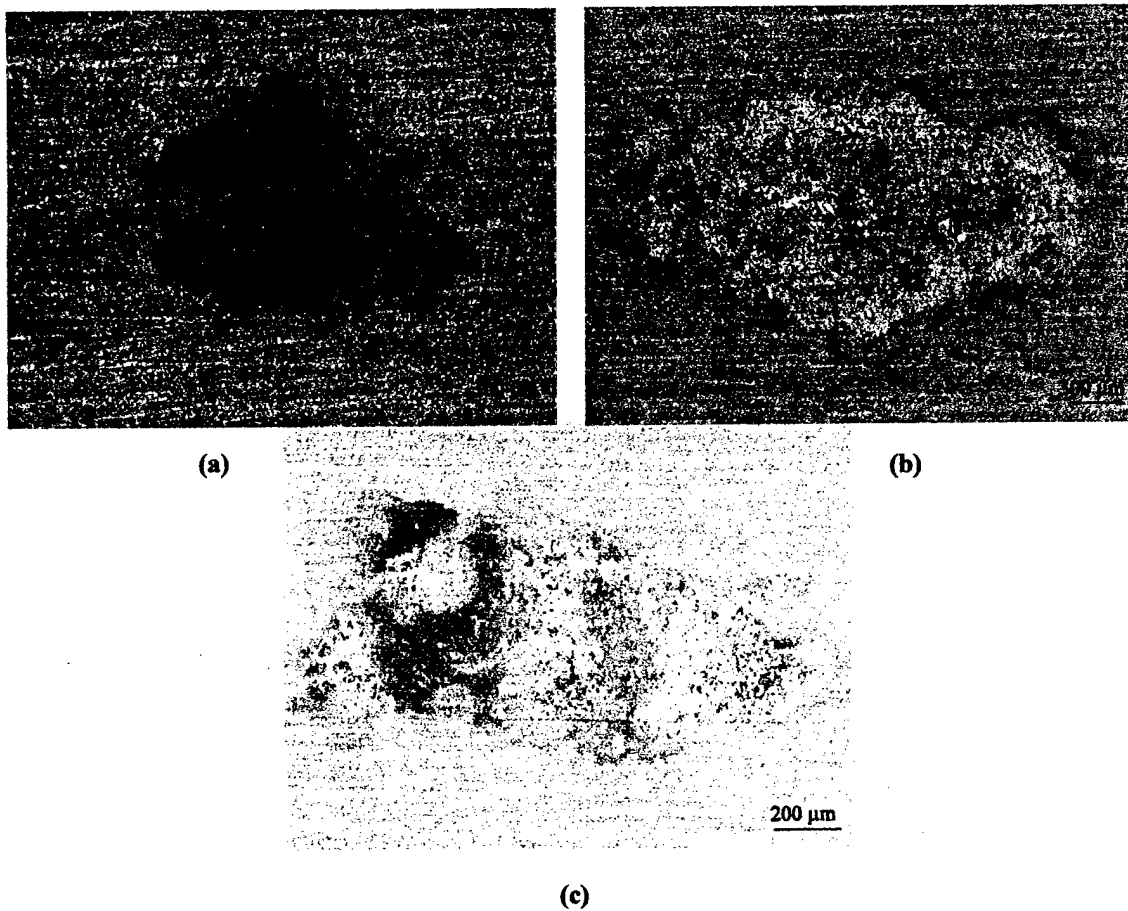
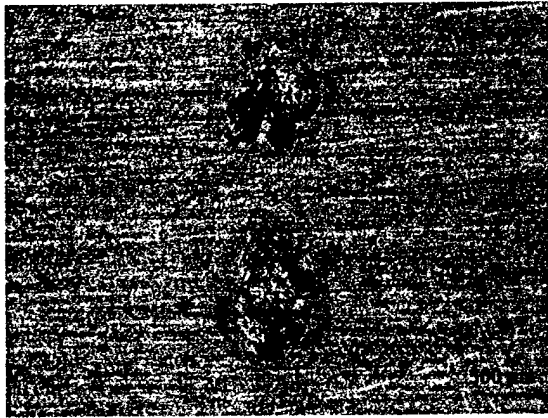


Figure 25. Representative examples of dog-bone samples polarized without the fingernail polish coating. (a) 4 hours of polarization (b) 8 hours of polarization (c) 12 hours of polarization



(a)



(b)



(c)



(d)



(e)



(f)

Figure 26. Six examples of dog-bone samples polarized with the fingernail polish coating. (a) 4 hours of polarization (b) 8 hours of polarization (c) 12 hours of polarization (d) 16 hours of polarization (e) 20 hours of polarization (f) 24 hours of polarization.

4.2.2 Characterization of Pitted Samples

The pit morphology was characterized using WLIM, as explained in the section 4.1.3. SEM was also used to characterize a few select samples. Since SEM is a well established method, it was used to mainly compare the qualitative surface features with those shown in the WLIM surface profiles. Figures 27-33 show several scanning electron micrographs, optical micrographs and WLIM profiles of a few samples used in this fatigue experiment. These profiles were taken before the samples were fatigued. Figures 27 and 28 show bare dog-bone samples that have been pitted, and Figures 29-33 show samples that were coated with the fingernail polish and then pitted.

The bare samples shown in Figures 27 and 28 have a large number of small shallow pits covering the entire exposed surface. As was expected, the sample that was polarized for twelve hours shows deeper pits than the sample polarized for four hours. The twelve-hour polarization scan provided the extra time needed for a few of the shallow pits to grow deeper. However, the deepest pit only reached approximately 25 μm .

In comparing these samples with those shown in Figures 29-33, the pit morphology is quite different. The samples shown in Figures 29-33 were coated with the fingernail polish to restrict the number of sites for pit nucleation and to allow formation of a few large pits. The polarization times for the samples shown in Figures 29-33 range from 4 hours to 24 hours. The longer polarization time produced larger pits. As the polarization times increased, the pit depths also increased. The sample shown in Figure 32

was polarized for twenty hours, yet the pits are deeper than the sample polarized for twenty-four hours, which is shown in Figure 33. However, the pits in Figure 33 (24 hours of polarization) have a larger diameter than those shown in Figure 32 (20 hours of polarization), so instead of growing deeper, the pits expanded during the extra polarization time.

A two-dimensional analysis was performed for each sample as described in the section 4.1.3. The pitting parameters described in section 4.2.1 were recorded for each sample. The pitting parameters for each sample are listed in Appendix A.

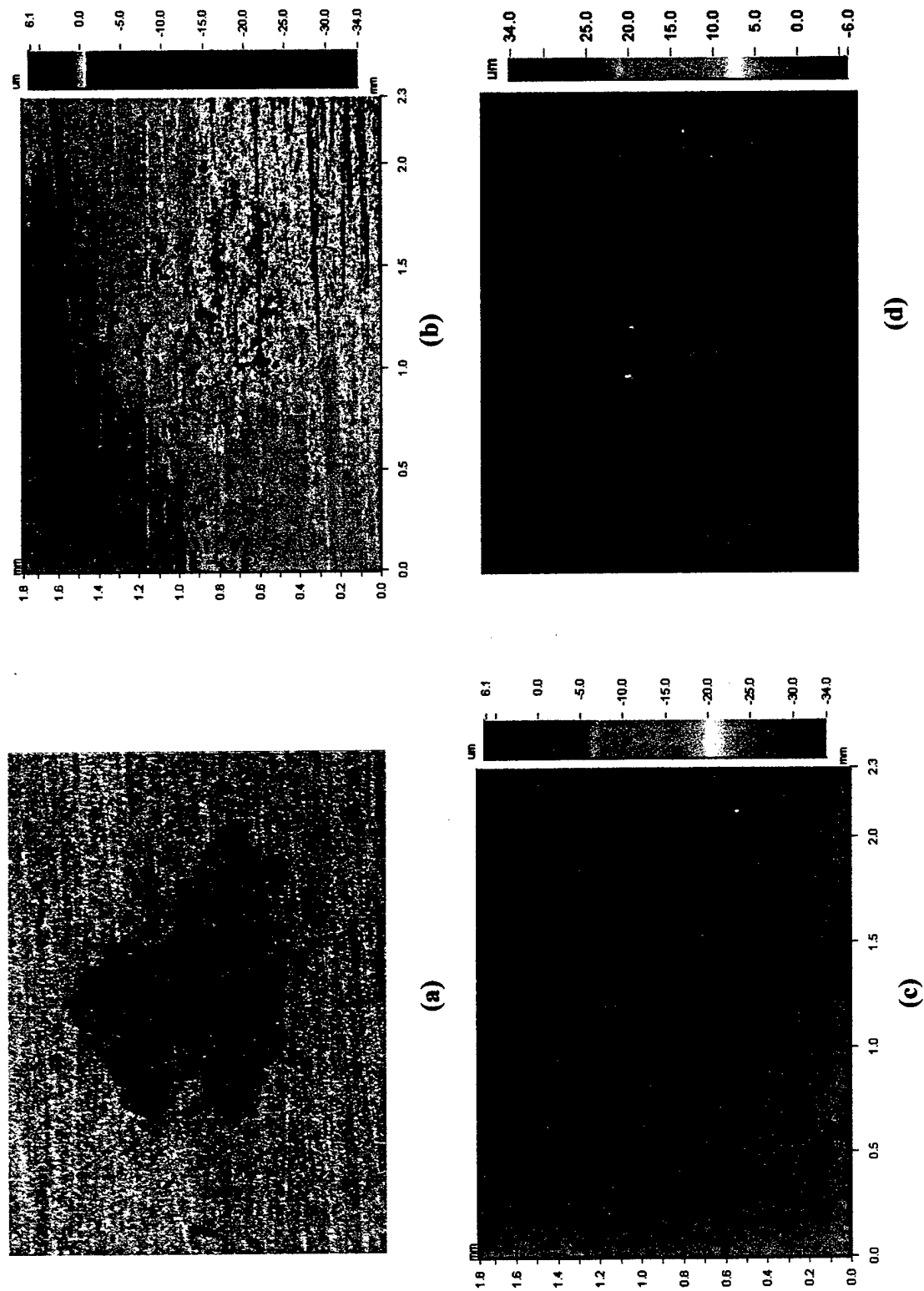


Figure 27. Bare dog-bone sample polarized for 4 hours: (a) Optical micrograph of pitted surface (b) WLIM maximum contrast profile showing shallow surface features (c) WLIM surface profile (d) WLIM 3-D profile showing pit contour and shape.

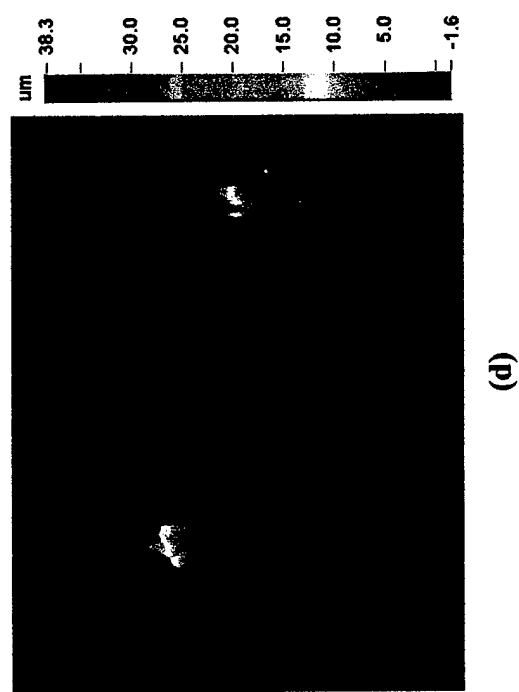
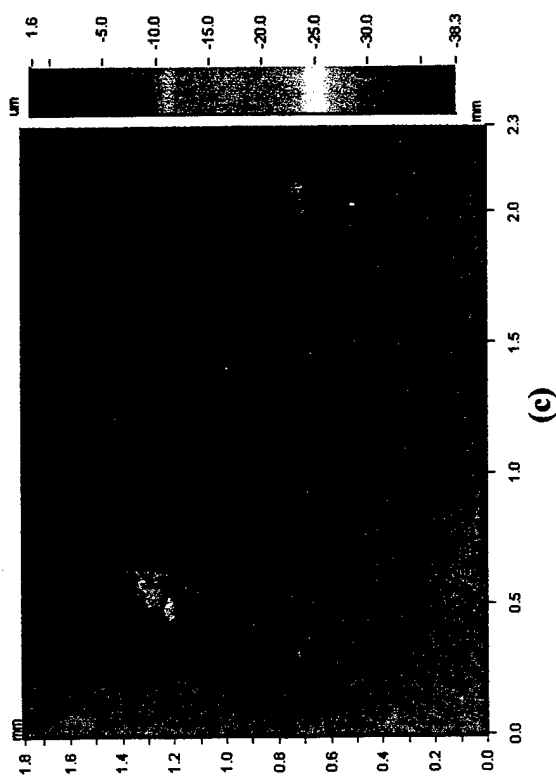
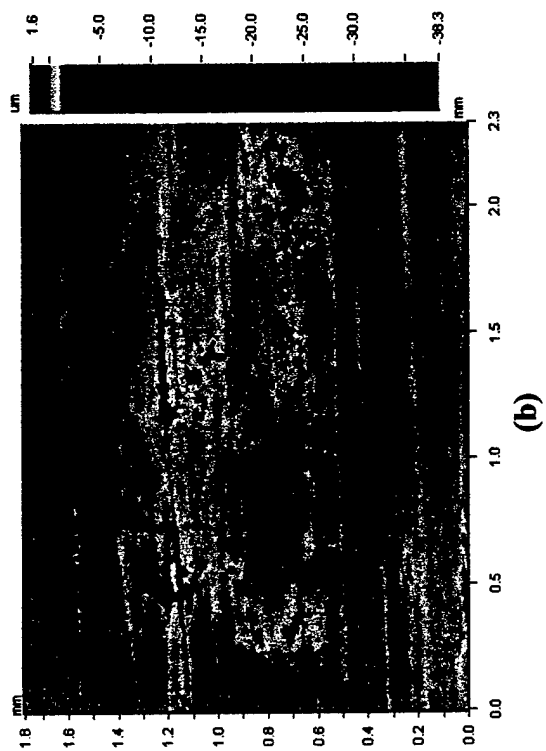


Figure 28. Bare dog-bone sample polarized for 12 hours: (a) Optical micrograph of pitted surface (b) W LIM maximum contrast profile showing shallow surface features (c) W LIM surface profile (d) W LIM 3-D profile showing pit contour and shape.

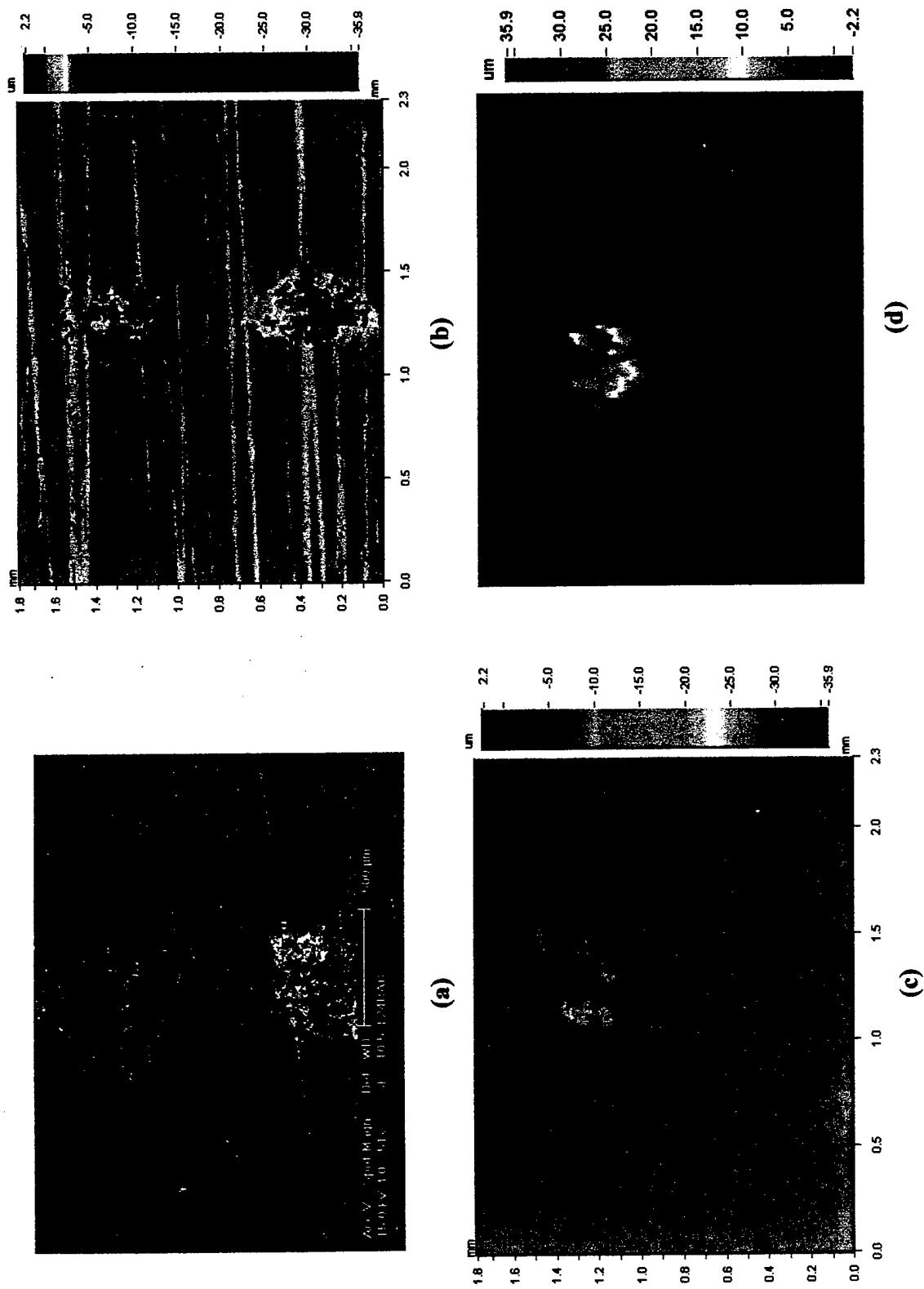


Figure 29. Fingernail polish coated dog-bone sample polarized for 4 hours: (a) Scanning electron micrograph of pitted surface (b) WLIM maximum contrast profile showing shallow surface features (c) WLIM surface profile (d) WLIM 3-D profile showing pit contour and shape.

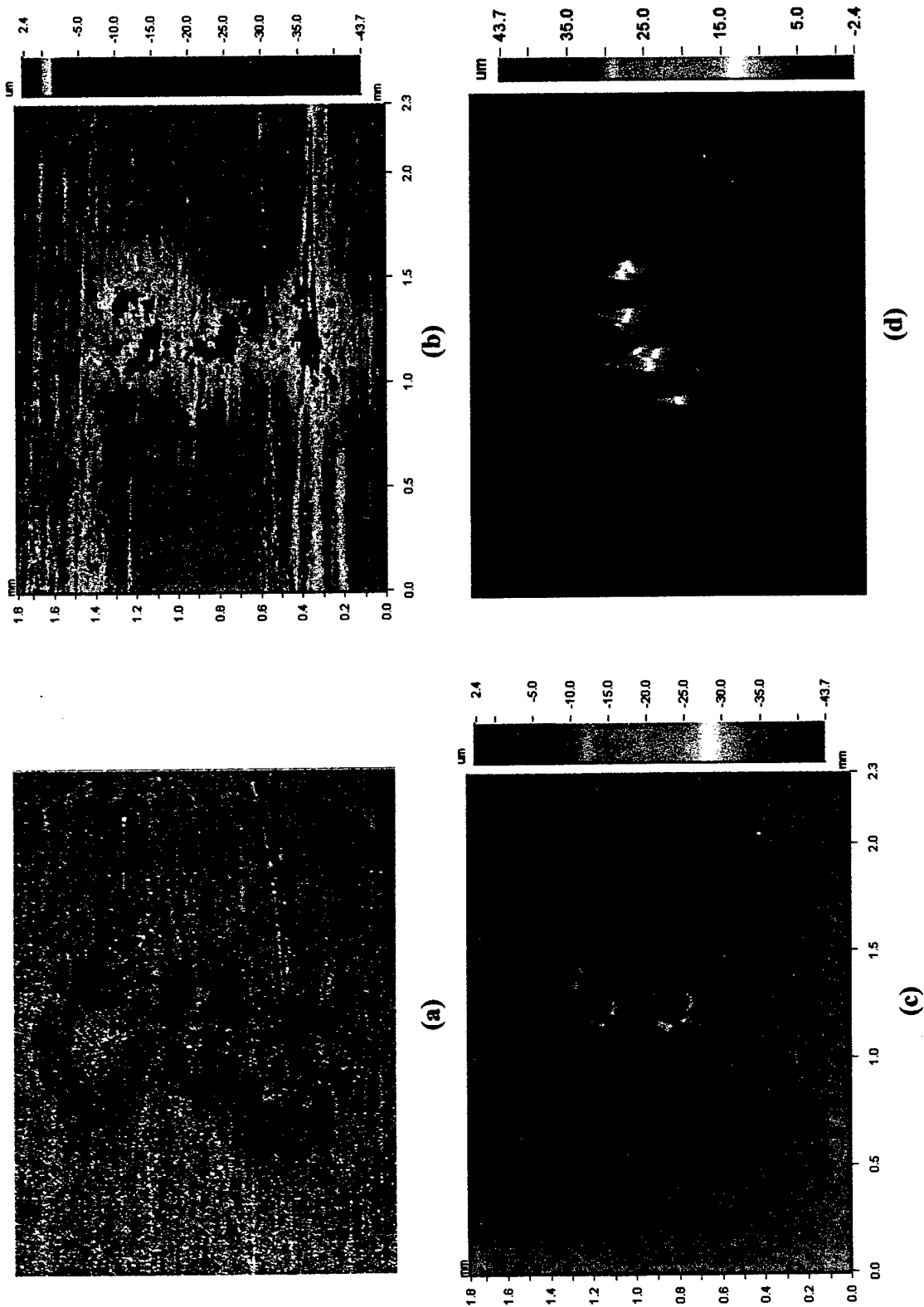
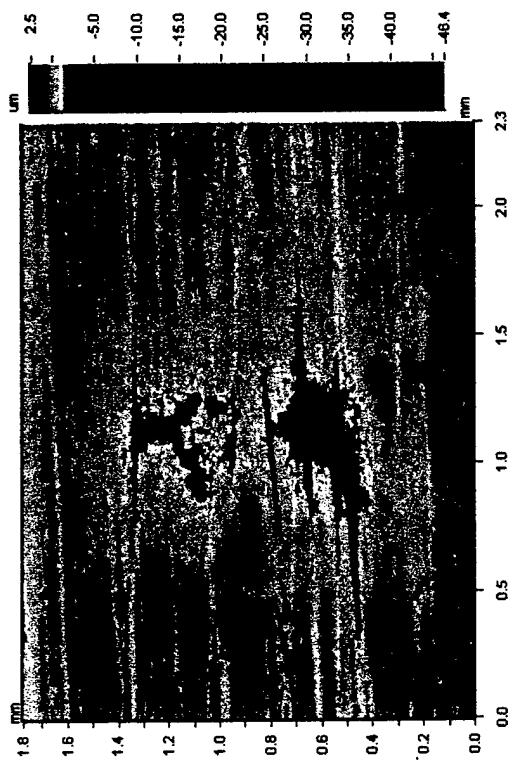


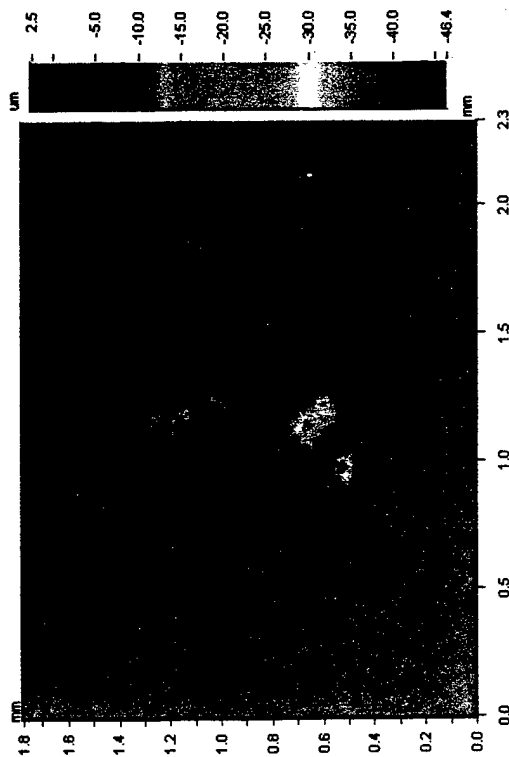
Figure 30. Fingernail polish coated dog-bone sample polarized for 12 hours: (a) Optical micrograph of pitted surface (b) WLM maximum contrast profile showing shallow surface features (c) WLM surface profile (d) LIM 3-D profile showing pit contour and shape.



(a)



(b)

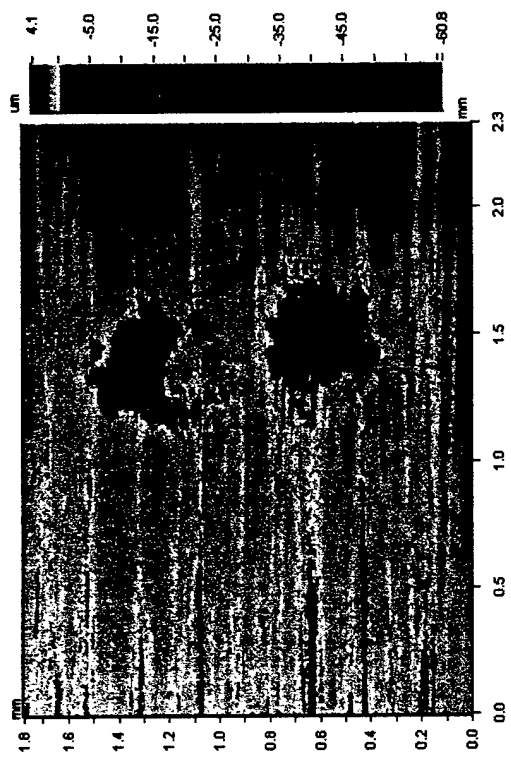


(c)

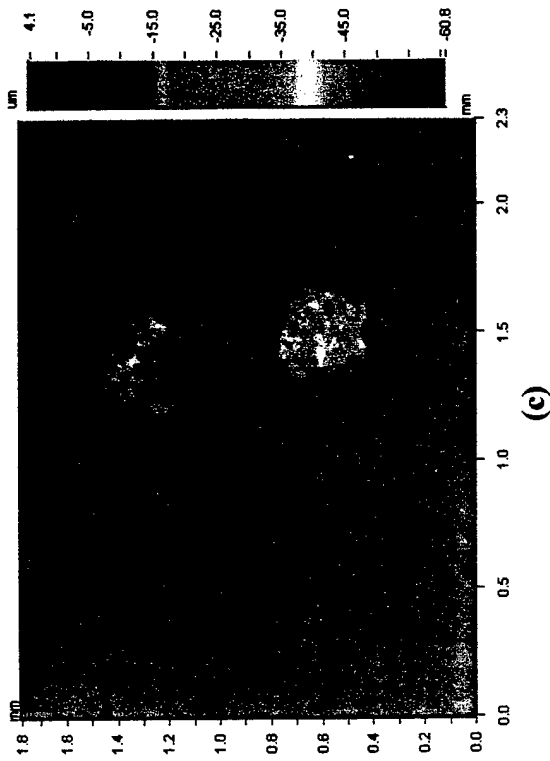


(d)

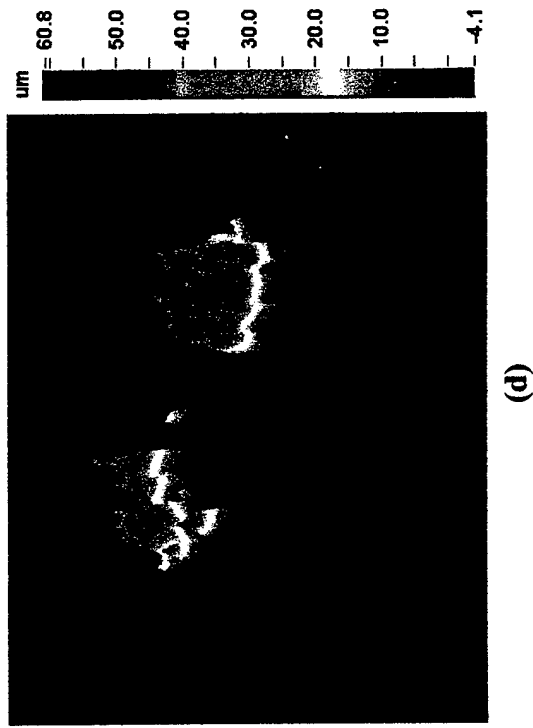
Figure 31. Fingernail polish coated dog-bone sample polarized for 16 hours: (a) Optical micrograph of pitted surface (b) WLI maximum contrast profile showing shallow surface features (c) WLI surface profile (d) WLI 3-D profile showing pit contour and shape.



(b)

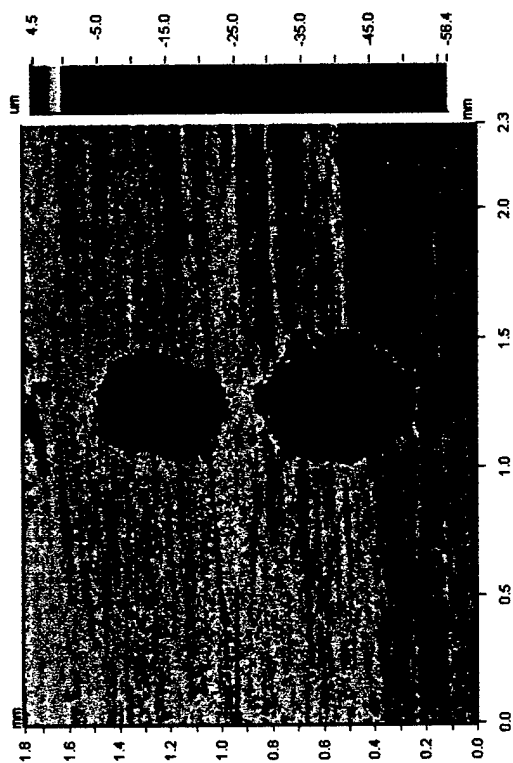


(c)

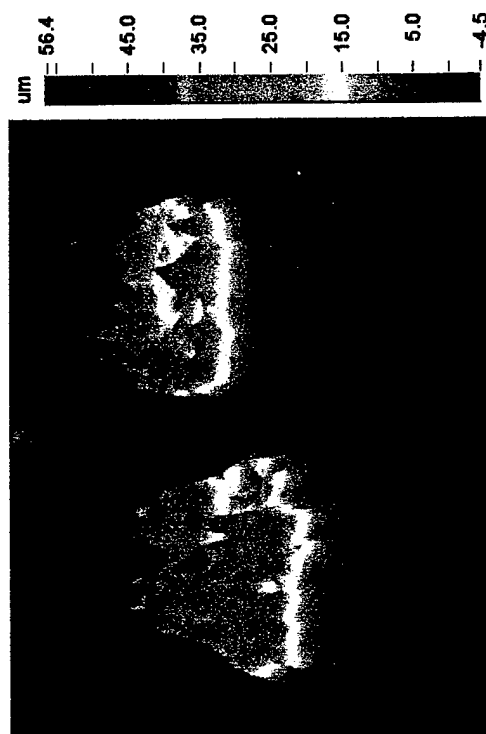


(d)

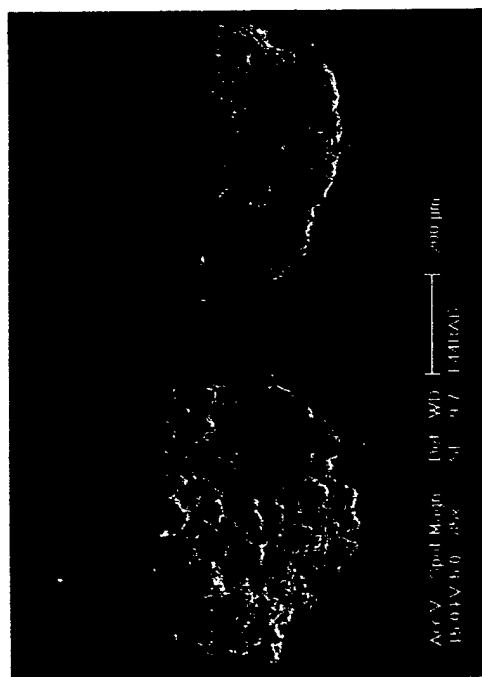
Figure 32. Fingernail polish coated dog-bone sample polarized for 20 hours: (a) Scanning electron micrograph of pitted surface (b) WLIM maximum contrast profile showing shallow surface features (c) WLIM 3-D profile showing pit contour and shape.



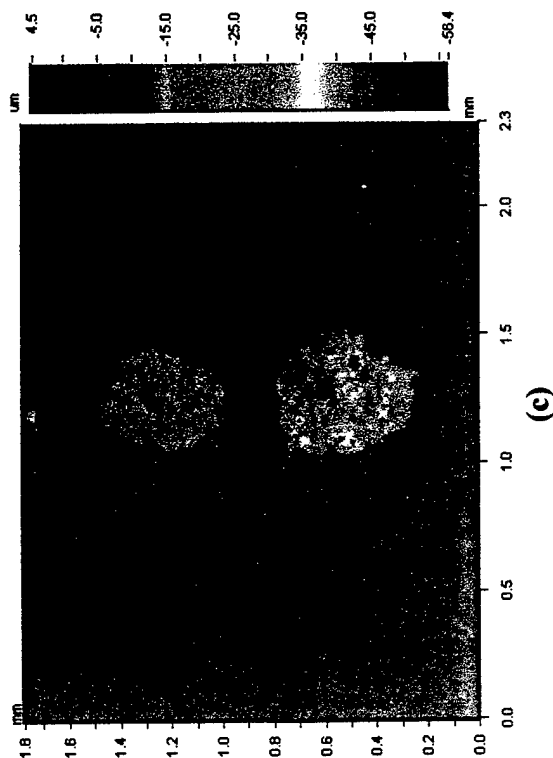
(b)



(d)



(a)



(c)

Figure 33. Fingernail polish coated dog-bone sample polarized for 24 hours: (a) Scanning electron micrograph of pitted surface (b) WLM maximum contrast profile showing shallow surface features (c) WLM surface profile (d) WLM 3-D profile showing pit contour and shape.

4.2.3 Fatigue Testing

The pitted samples previously described were fatigued after the surface pit morphology was characterized completely. The samples were subjected to fatigue with the parameters listed in section 3.3. The main goal of this study was to determine the critical pit size. The critical pit size is the size of the pit that initiates the crack that caused the sample to fail. Figure 34 schematically illustrates the fatigue crack initiation and growth process.

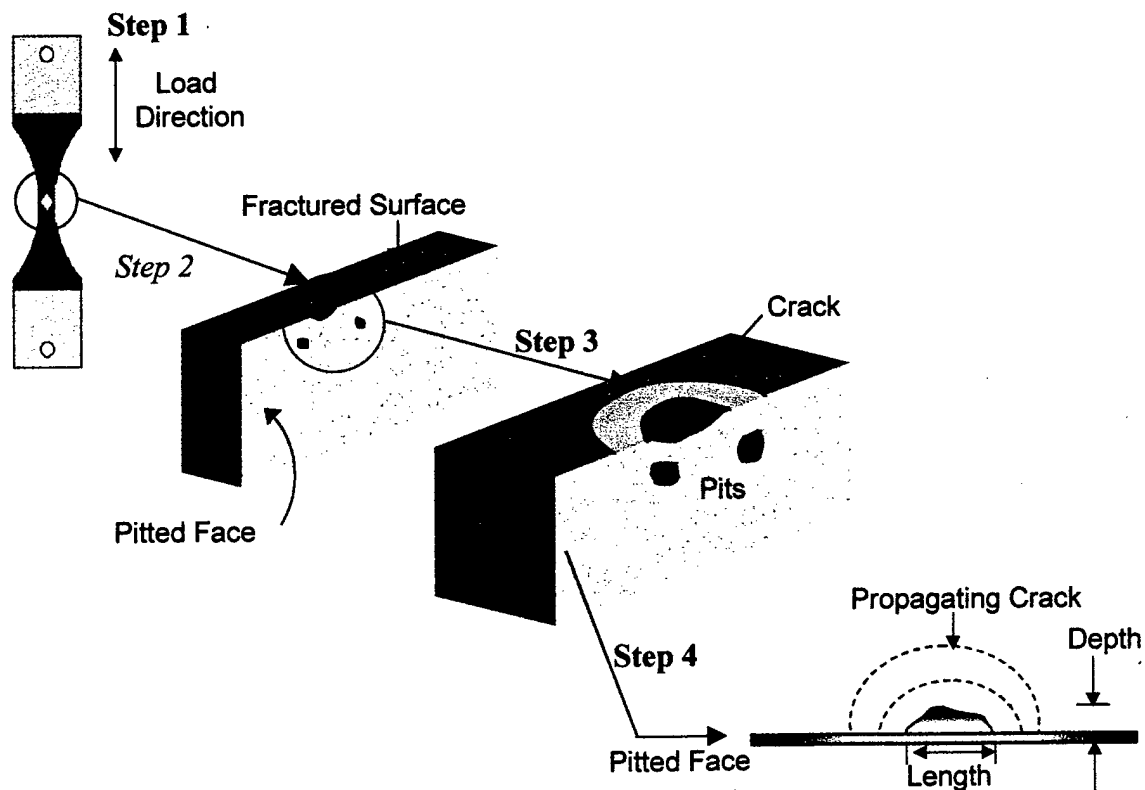
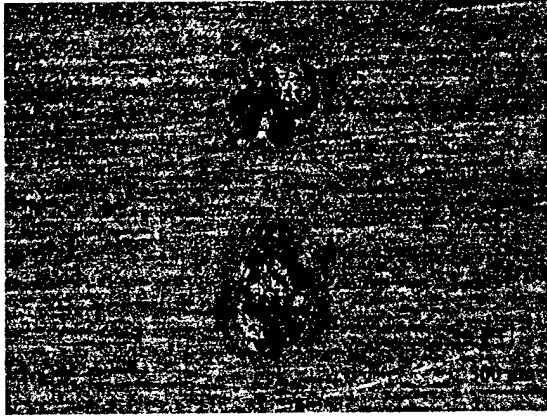


Figure 34. Fatigue crack growth schematics of pitted sample.

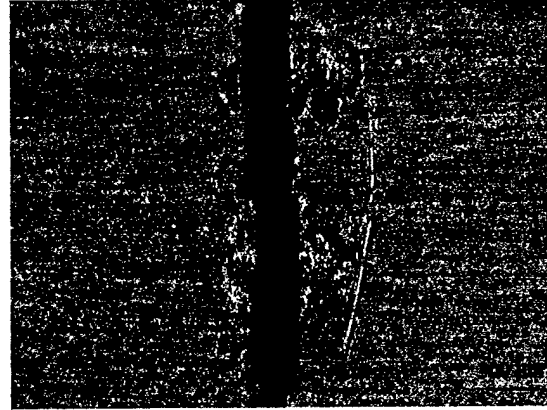
The crack growth schematics illustrated in Figure 34 begin with a pitted dog-bone sample. The sample is fatigued to failure with the load direction parallel to the tensile axis of the sample. In Step 2, the fractured surface of the gauge section of the sample is inspected to determine which pit initiated the crack. A single semi-elliptic surface crack develops from the critical pit, which is shown in Step 3. This surface crack is identified by its lighter color compared with the aluminum matrix. Such a crack, once initiated, grows, as the sample is fatigued until final failure occurs. Step 4 is a two-dimensional representation of Step 3 showing the propagation of the surface crack. Step 4 also shows that the maximum pit depth is considered as the initial crack length.

Figures 35-37 show several samples before and after they were fractured under fatigue. The pitted face for each sample was examined first to determine the area where the crack developed. For the sample in Figure 35, it appeared that the crack progressed from both of the pits on the surface. Therefore, the fractured surface was examined for the initiation site of the single semi-elliptic crack. Since the single semi-elliptic crack is centered from one specific pit, as noted in Figure 35(c), this pit was determined to be the critical pit for this sample. The depth and diameter of this critical pit were calculated using the WLIM two-dimensional analysis

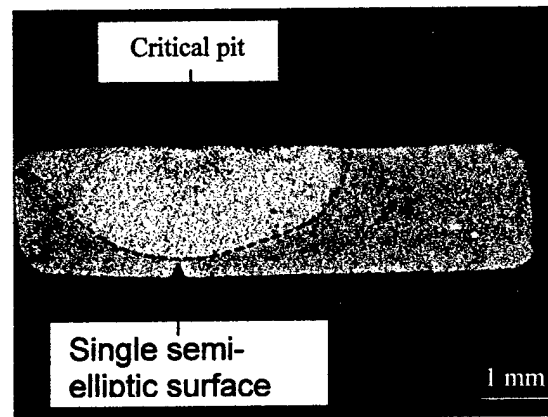
The sample in Figure 36 better illustrates crack initiation from a pit. The crack initiates from both pits on the surface similar to that shown by the sample in Figure 35. When the fractured surface was examined, as shown in Figure 36(c), both pits could be seen, but the crack was centered around the left pit. This corresponds with the top pit shown in Figure 36(a). Therefore, this pit was considered as the critical pit, and its dimensions were determined.



(a)

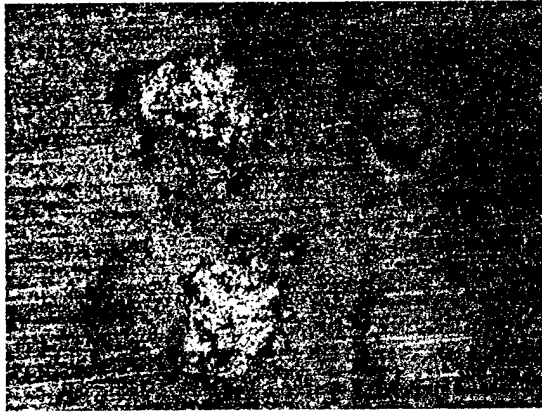


(b)

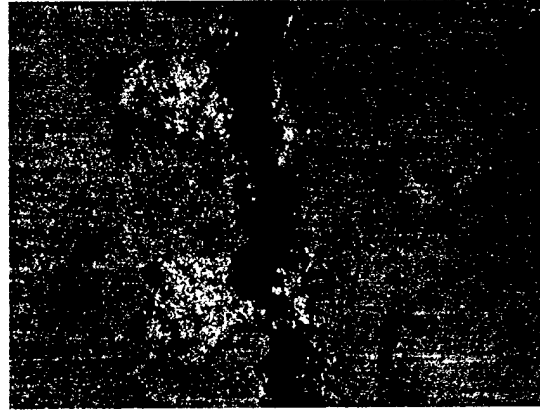


(c)

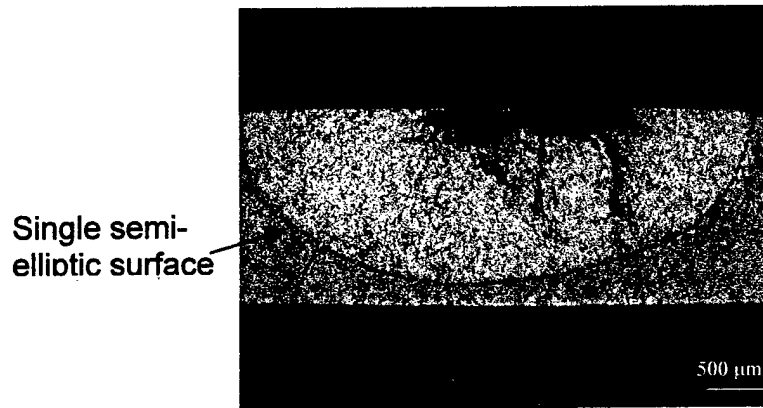
Figure 35. Fingernail polish coated dog-bone sample polarized for 4 hours (a) Optical micrograph of pitted surface before fracture (b) Optical micrograph of pitted surface after fracture (c) Fractured surface showing semi-elliptic crack.



(a)



(b)



(c)

Figure 36. Fingernail polish coated dog-bone sample polarized for 20 hours (a) Optical micrograph of pitted surface before fracture (b) Optical micrograph of pitted surface after fracture (c) Fractured surface showing semi-elliptic crack.

Another situation is shown in Figure 37. Two pits are present on this surface, and the crack progresses through both of them. This is an example where two adjacent pits coalesce to initiate a crack. The combined diameter and deepest point are recorded using the WLIM two-dimensional analysis.

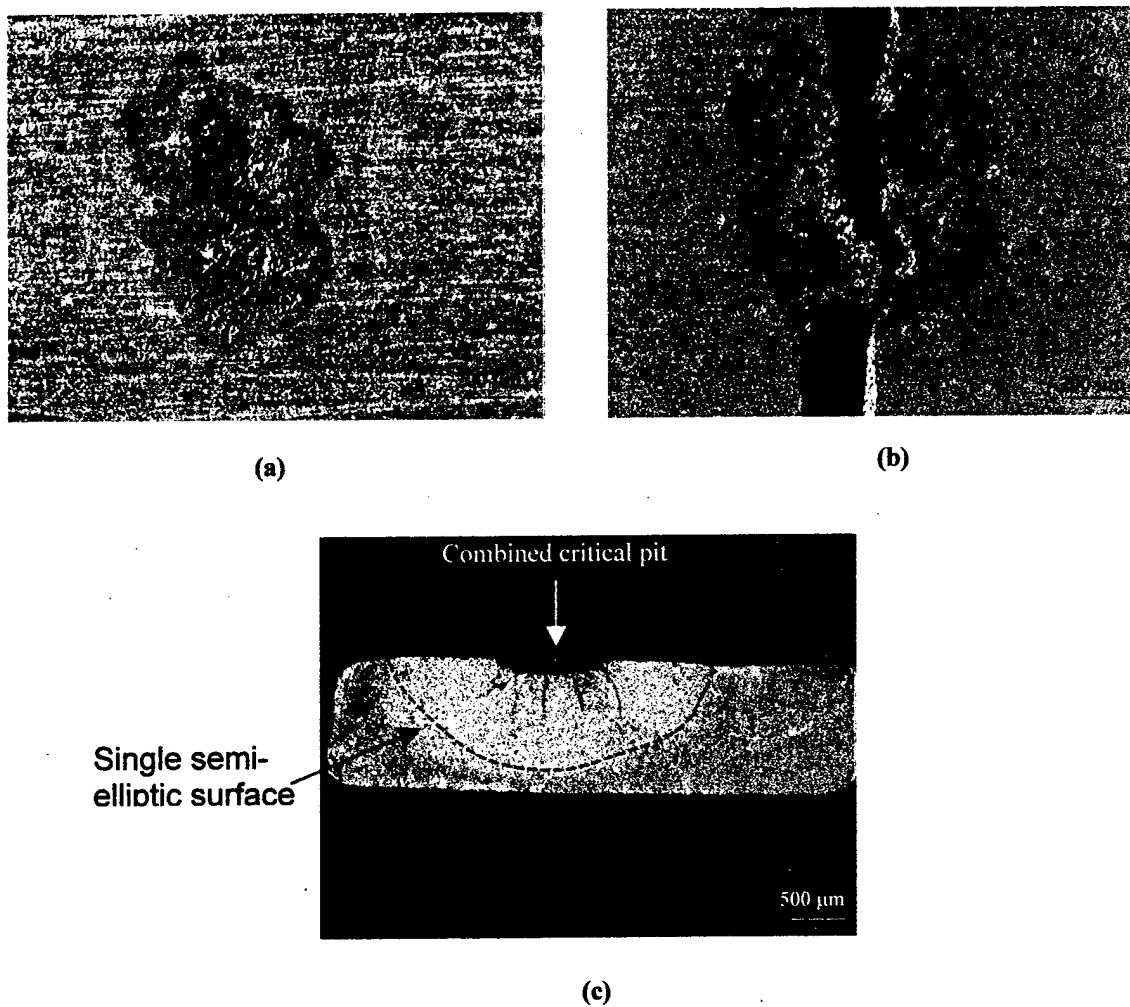


Figure 37. Fingernail polish coated dog-bone sample polarized for 8 hours (a) Optical micrograph of pitted surface before fracture (b) Optical micrograph of pitted surface after fracture (c) Fractured surface showing semi-elliptic crack.

4.2.4 Stress Intensity Factor Calculation

All samples were examined as described above, and all data is shown in Appendix

A. Once all the required parameters were obtained using WLIM, the stress intensity factor for each specimen was calculated. This parameter was used in the determination of a relationship between the pitting and fatigue parameters, as mentioned at the end of Chapter 1.

The stress intensity factor for each sample was calculated using a program developed at the University of Dayton Research Institute²⁴. The program is based on the work done by Newman and Raju.²⁵ Empirical equations used to calculate stress-intensity factors for a variety of three-dimensional crack configurations are discussed in this paper. The configuration used in this investigation treated the pit as a semi-elliptical surface crack. This configuration is illustrated in Figure 38.

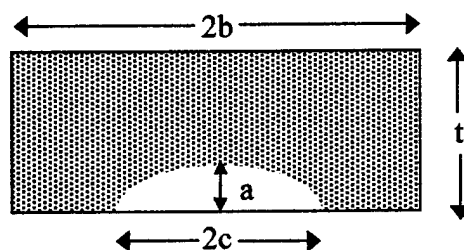


Figure 38. Semi-elliptical surface crack configuration, where dimension a is the crack depth, t is half-thickness of plate, b is half-width of cracked plate, and c is half-length of crack.²⁵

The following is an outline of the equations used in the WPAFB program to calculate the stress intensity factor. The equations for the stress intensity factors were based on finite-element analyses conducted by Newman and Raju.²⁵

The stress intensity factor, K , at any point along the semi-elliptical surface crack front in a finite-thickness plate is shown in Equation 4²⁵:

$$K = S \sqrt{\frac{\pi a}{Q}} F_s \left(\frac{a}{t}, \frac{a}{c}, \frac{c}{b}, \phi \right) \quad \text{Eq. 4}$$

The variables a , b , c and t were defined in Figure 37. The parameter Q is the shape factor for an ellipse. In this study, the ratio of crack depth to crack length (a/c) was always less than unity. Therefore, the following expression was used in calculating Q ²⁵:

$$Q = 1 + 1.464 \left(\frac{a}{c} \right)^{1.65} \quad \left(\text{for } \frac{a}{c} \leq 1 \right) \quad \text{Eq. 5}$$

The maximum error in the stress-intensity factor by using this equation for Q was about 0.13% for all values of a/c ²⁵. The parameter ϕ in Equation 4 is the parametric angle of the ellipse. Figure 39 illustrates how ϕ is determined when the ratio of crack depth to crack length (a/c) is less than one.

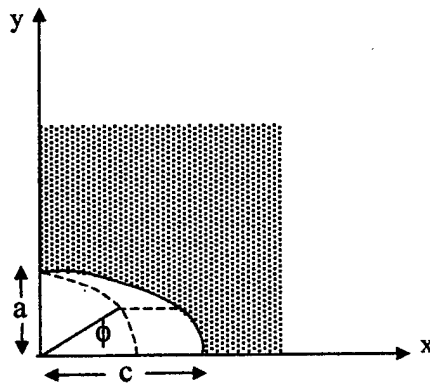


Figure 39. Coordinate system used to define parametric angle for $a/c \leq 1$.

The function F_s accounts for the influence of crack shape (a/c), crack size (a/t), finite width (c/b), and angular location (ϕ), and was represented by Newman and Raju as:

$$F_s = \left[M_1 + M_2 \left(\frac{a}{t} \right)^2 + M_3 \left(\frac{a}{t} \right)^4 \right] g f_\phi f_w \quad \text{Eq. 6}$$

The following definitions of the parameters in Equation 4 are applicable when $a/c \leq 1$ and

$$M_1 = 1.13 - 0.09 \left(\frac{a}{c} \right) \quad \text{Eq. 7}$$

$$M_2 = -0.54 + \frac{0.89}{0.2 + \left(\frac{a}{c} \right)} \quad \text{Eq. 8}$$

were taken from reference 25:

$$M_3 = 0.5 - \frac{1}{0.65 + \frac{a}{c}} + 14 \left(1 - \frac{a}{c} \right)^{24} \quad \text{Eq. 9}$$

$$g = 1 + \left[0.1 + 0.35 \left(\frac{a}{t} \right)^2 \right] (1 - \sin \phi)^2 \quad \text{Eq. 10}$$

$$f_\phi = \left[\left(\frac{a}{c} \right)^2 \cos^2 \phi + \sin^2 \phi \right]^{\frac{1}{4}} \quad \text{Eq. 11}$$

$$f_w = \left[\sec \left(\frac{\pi c}{2b} \sqrt{\frac{a}{t}} \right) \right]^{\frac{1}{2}} \quad \text{Eq. 12}$$

4.2.5 Relationships Resulting From Controlled Fatigue Experiment

After the stress intensity factor was calculated using the method described above, an attempt was made to correlate the pitting parameters with this fatigue parameter.

It is generally known that fatigue life at a constant stress approximates a log normal distribution.²⁶ Therefore, the average values used in the following relationships were based on a log normal distribution.

Several initial relationships were investigated to observe the behavior of the data resulting from the fatigue analysis. The first plot is shown in Figure 40. The plot shows the variation of the fatigue life with the length of the polarization scan for the samples not coated with the fingernail polish. The trend appears to show that the lives of the samples decrease as the polarization times increase. This can be explained by the fact that the longer polarization allows more reaction time for pit growth. These larger pits seem to initiate cracks more quickly than the smaller pits, resulting in a more rapid failure and shorter fatigue life.

A similar trend is also observed for the samples coated with the fingernail polish, as seen in Figure 41. The fatigue life decreases as the polarization time increases for samples with a polarization length up to 16 hours. However, this trend changes after 16 hours of polarization. The fatigue lives of the samples increase with increasing polarization time. Also, there is a much wider scatter in life cycles for the samples that

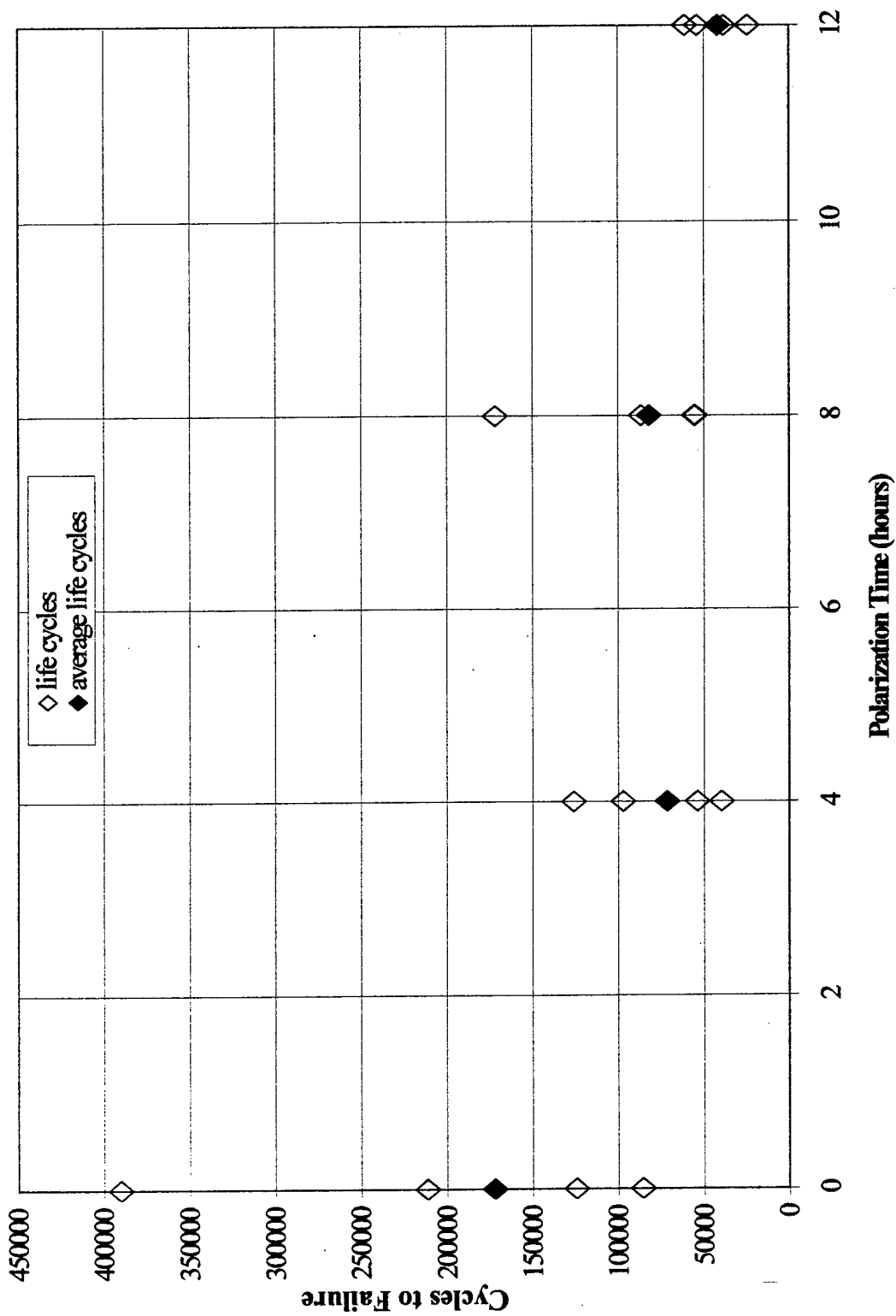


Figure 40. Cycles to failure versus polarization time for samples not coated with the fingernail polish.

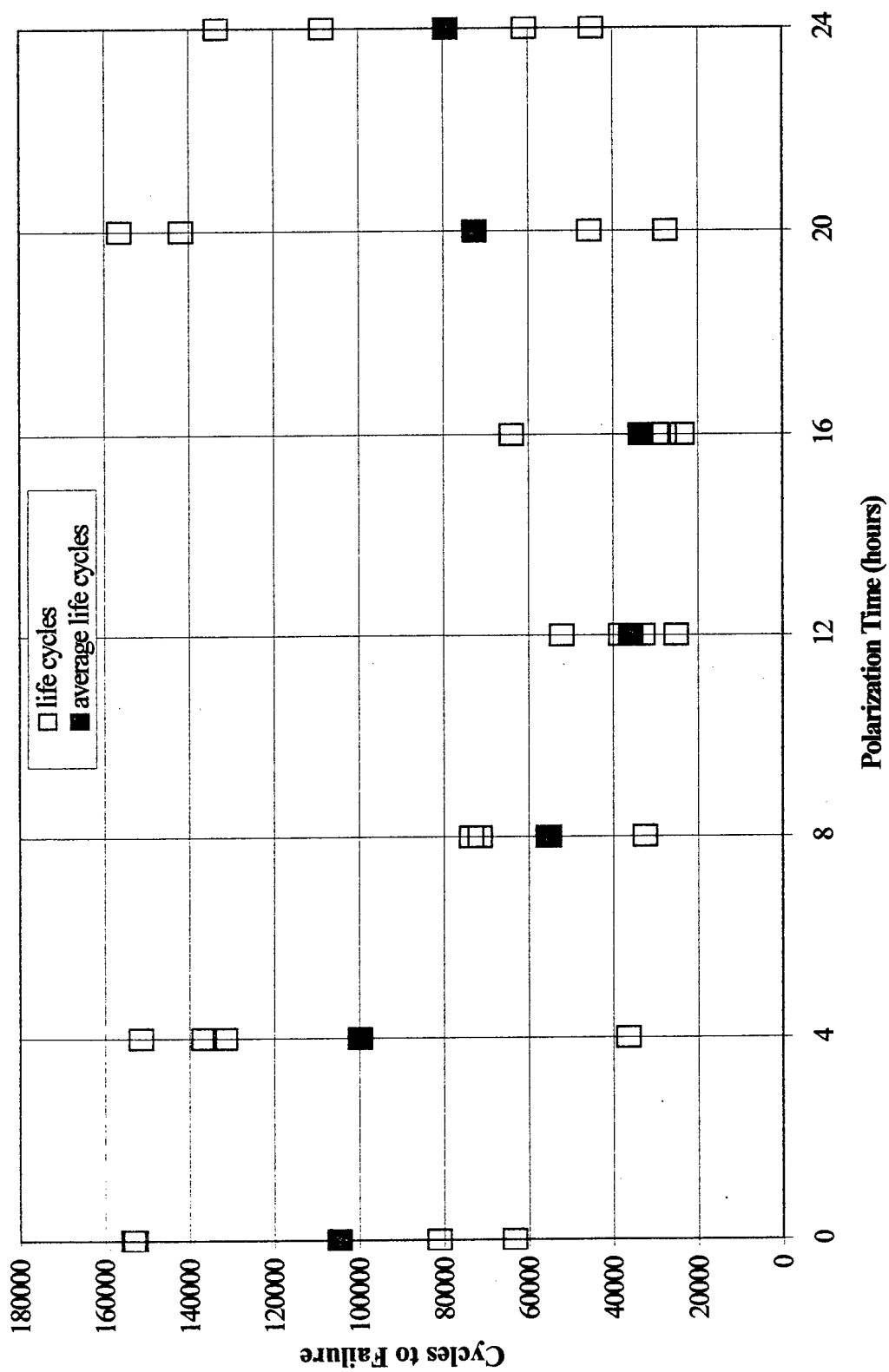


Figure 41. Cycles to failure versus polarization time for samples coated with the fingernail polish.

were polarized for 20 and 24 hours. The average deviation method²⁶ was used to test the statistical significance of possible outliers, but all data was found to be valid.

A possible cause for the trend change may be due to the long length of these polarization schemes. The pits begin to grow larger in diameter rather than deeper over this longer a period of polarization. Therefore, the pits are not high stress concentrators. This would account for the longer life of these samples compared to the samples that were pitted using the shorter polarization schemes of 16 hours or less. More tests should be run at the longer polarization times of 20 hours and greater to determine if this hypothesis is true.

Another observation was made that may account for the longer life for the 20 and 24 hour scanned samples. The pits appear to repassivate after a certain length of time for these samples. This length of time varied between samples. One explanation for the repassivation may be the coalescence of hydrogen bubbles on the surface of the samples. Small hydrogen bubbles are released as part of the pitting process. If the reaction is allowed to proceed sufficiently long, these bubbles may stay on the surface, blocking the electrolyte. This prevents the pitting process from taking place, and the pit stops growing although a potential is still applied to the system. Again, more testing must be performed to accurately determine if this is the true cause of the change in trend shown in Figure 41.

This unexplained change in the trend was also observed for the critical pit depth, as shown in Figure 42. All data points were determined to be statistically valid using the average deviation method. The initial trend is as expected: the critical pit depth increases as the polarization time increases. However, for the longer polarization times, the critical pit depth begins to decrease, which corresponds to the tendency shown for the higher

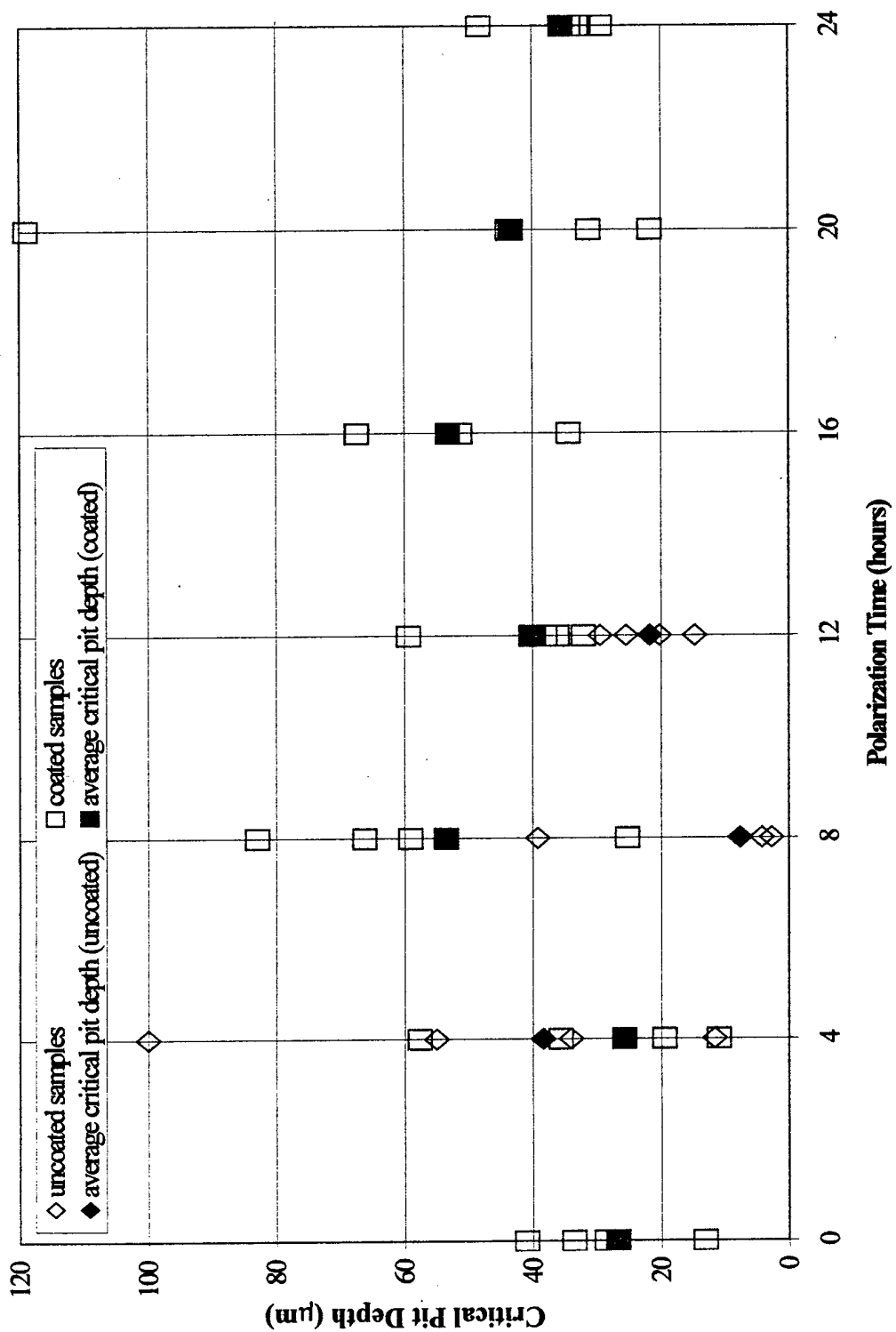


Figure 42. Critical pit depth versus polarization time.

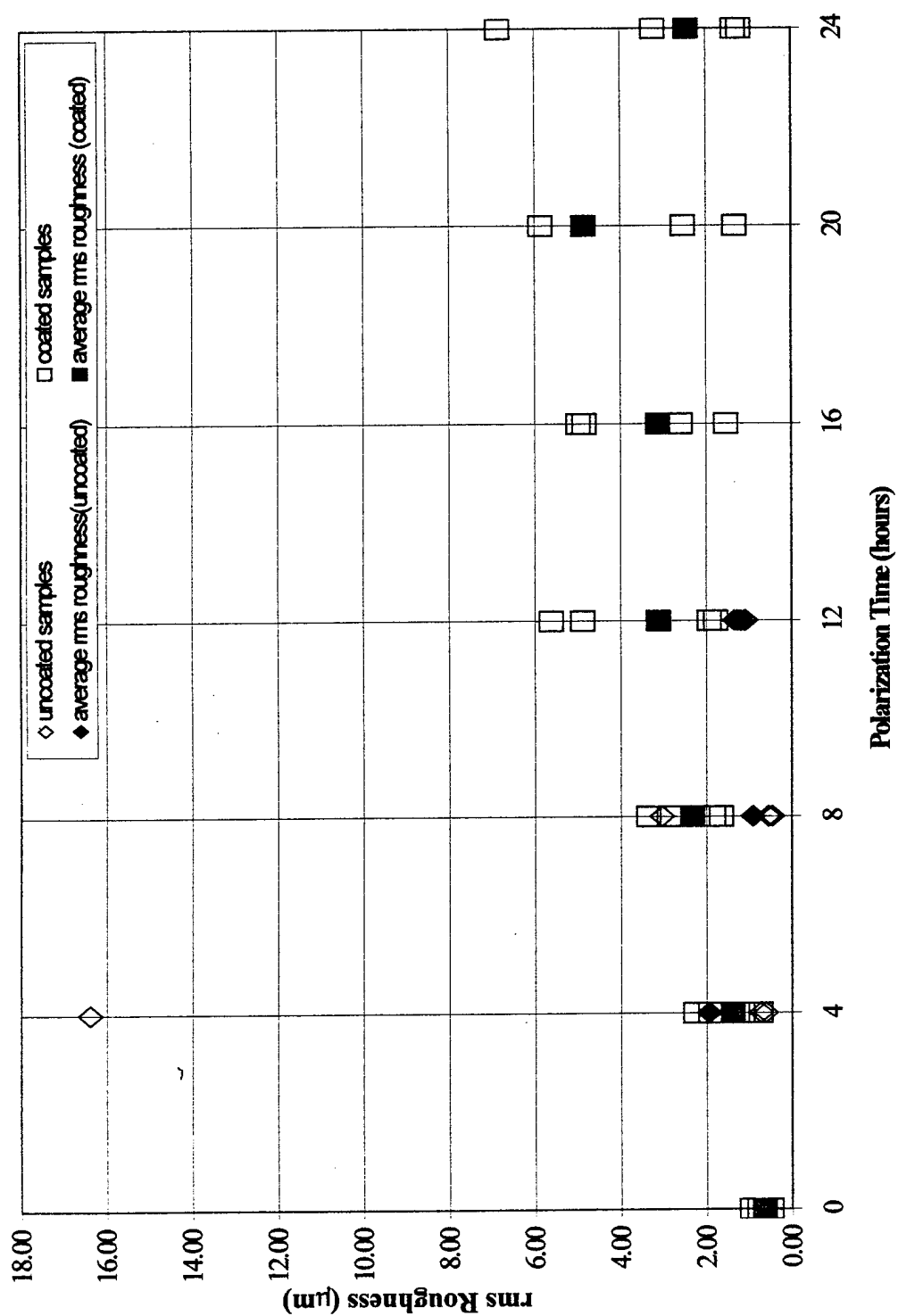


Figure 43. Rms roughness versus polarization time.

polarization times in Figure 41. Since pitting is such a random process, several experiments need to be run to determine if this is the actual behavior of the samples, or just the behavior of this first set.

The change in rms roughness with time is shown in Figure 43. The rms roughness is an important NDE parameter that can be determined in the field during an inspection. Therefore, a relationship between the rms roughness and a fatigue parameter will be very useful in predicting the fatigue life of a structure. As seen in Figure 43, the rms roughness slowly increases with increasing polarization time, until the last set of data point representing the 24-hour scan. Here, the rms roughness decreases for no apparent reason. Further investigation of the behavior during long polarization scans is required before any speculation about the cause can be offered.

The very same trend shown in Figure 43 is seen in Figure 44. The loss of mass due to the pitting process was plotted against polarization time. The behavior closely resembles that of the rms roughness. As the polarization time increased, an increasing amount of mass was lost due to metal dissolution. However, the data for the longer scan times show a wider spread than that for the rms roughness, but the behavior of the average values is closely related. The trend is understandable up to the 24-hour polarization time. Again, more controlled experiments are needed to determine the behavior at longer polarization times before accurate conclusions can be drawn.

One of the main objectives of this study was to find a relationship between a structural integrity parameter and a pitting parameter. Such a relationship is shown in Figure 45. The stress intensity factor was plotted against critical pit depth. There appears to be a linear relationship between the two parameters. This relationship can be

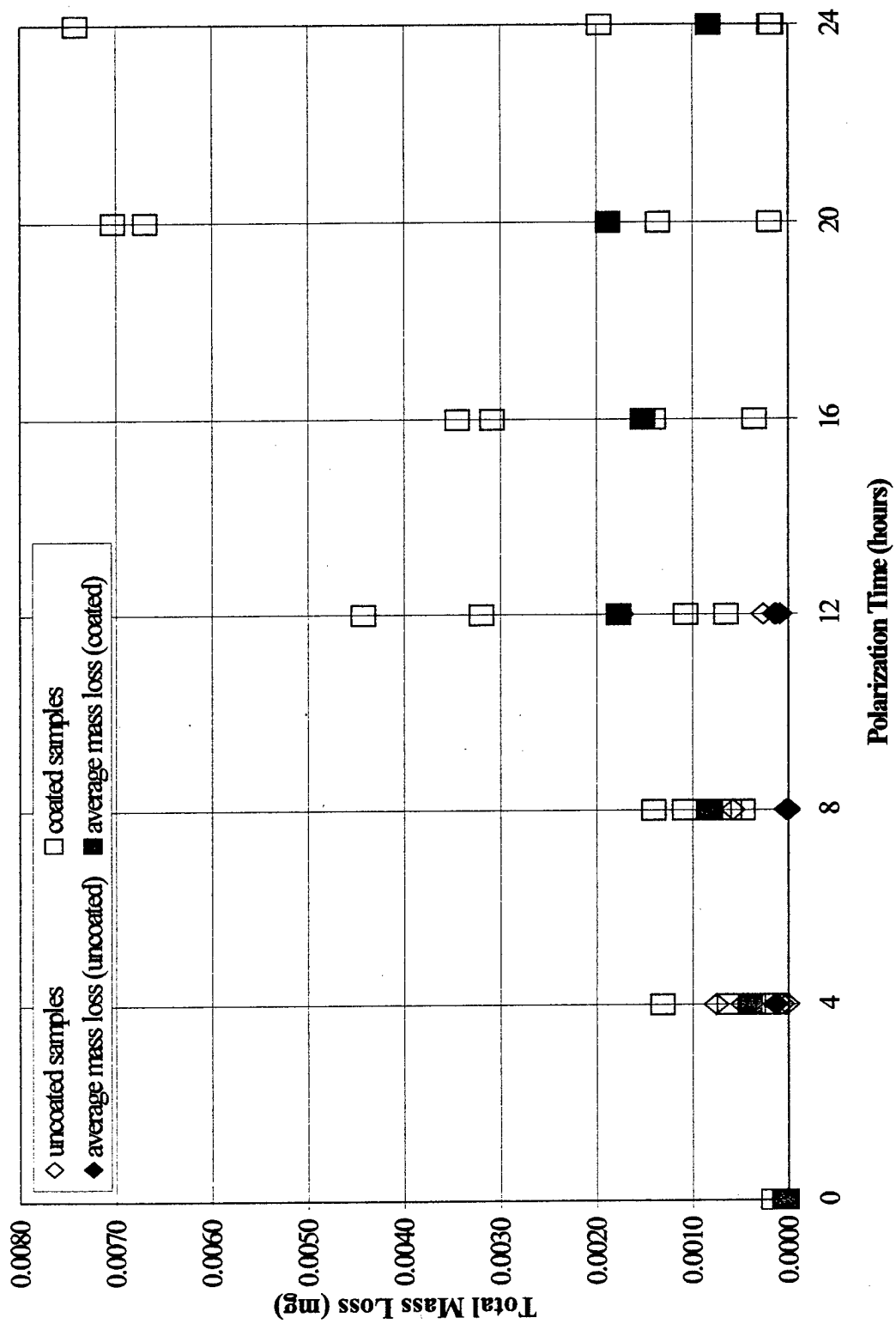


Figure 44. Mass loss versus polarization time.

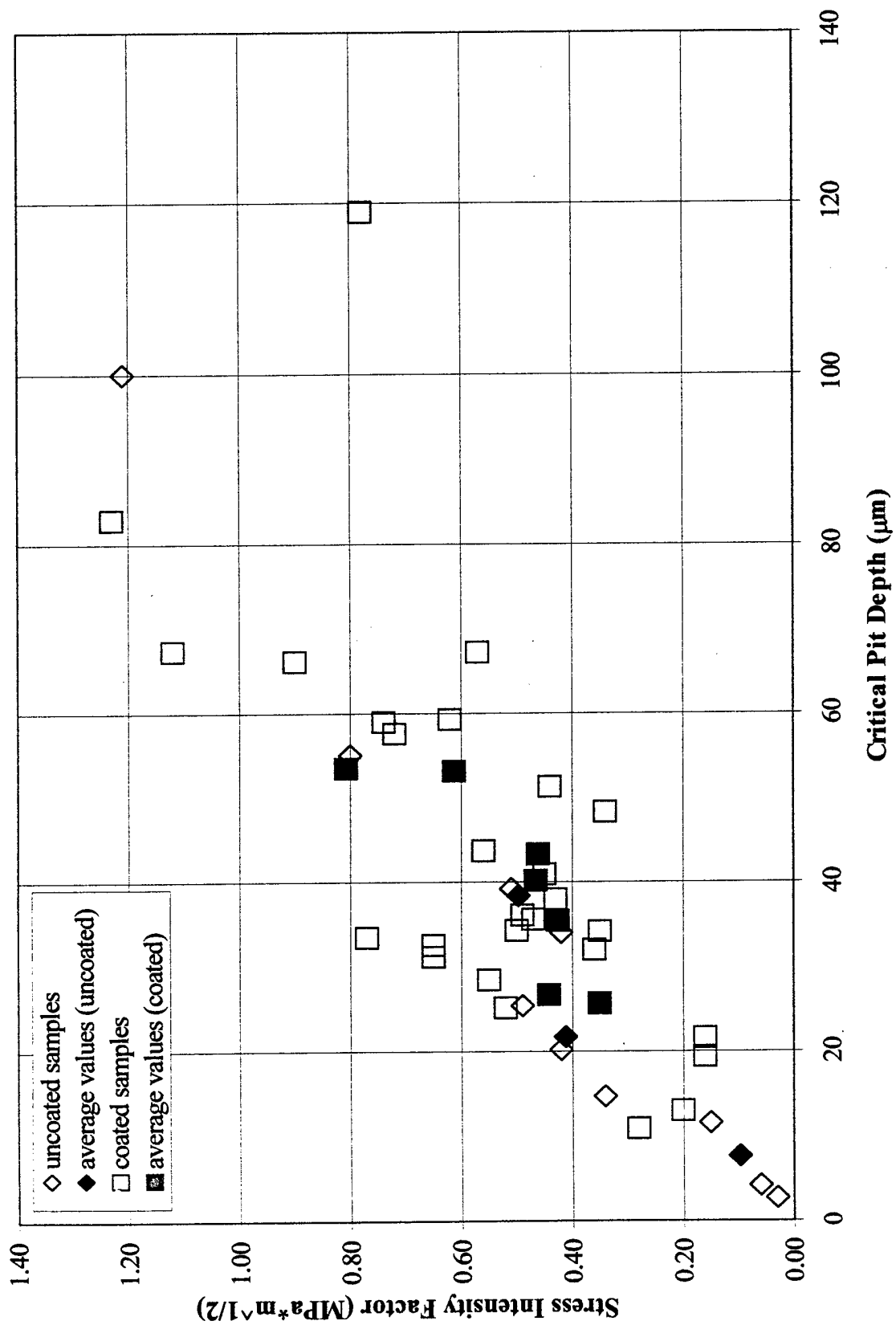


Figure 45. Stress intensity factor versus critical pit depth.

used in comparison with data from a field test to determine if this type of pitting is comparable to the actual pitting that takes place on a plane in the field.

The other sought after relationship was between a structural integrity parameter and a NDE parameter. This relationship can be used during a field inspection. The NDE parameter is determined from the inspection, and the structural integrity parameter can then be predicted from this relationship. In this way, the life of the structure could be predicted and appropriate measures could be taken to insure its stability and safety.

One of the common NDE parameters that is measured in the field is rms roughness. Figure 46 shows a plot of the stress intensity factor and rms roughness. Unfortunately, there appears to be no relationship between these two parameters. However, due to the random nature of the pitting process, more controlled experiments similar to this one should be run before conclusions are drawn.

Lastly, the crack growth data was examined. Figure 47 shows a plot of the crack growth rate versus ΔK . Both of these parameters were calculated using a University of Dayton Research Institute proprietary computer program called CRACK. The white squares represent long crack behavior from notched samples. This data was obtained from reference 27. The black squares represent the crack growth behavior of the samples from this study. As Figure 47 shows, the crack growth rate from the samples with shallow pits were almost an order of magnitude larger than the notched sample data. However, as the pit depths increased, the behavior transitioned into the long crack behavior. Therefore, it appears that the samples from this study exhibit short crack behavior when the critical pit depths are shallow. This should be investigated further in future studies, so that the crack growth behavior can be fully modeled.

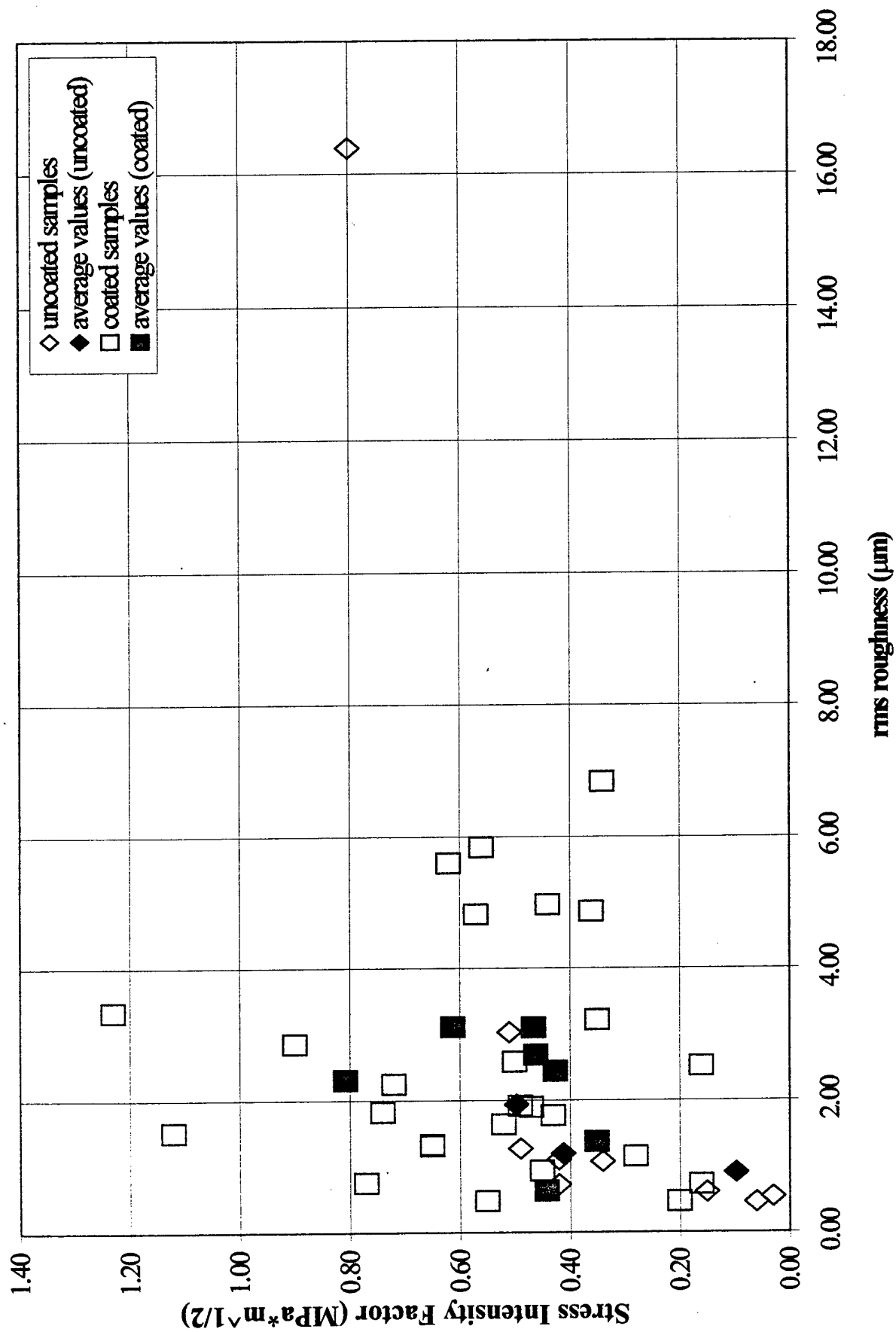


Figure 46. Stress intensity factor versus rms roughness.

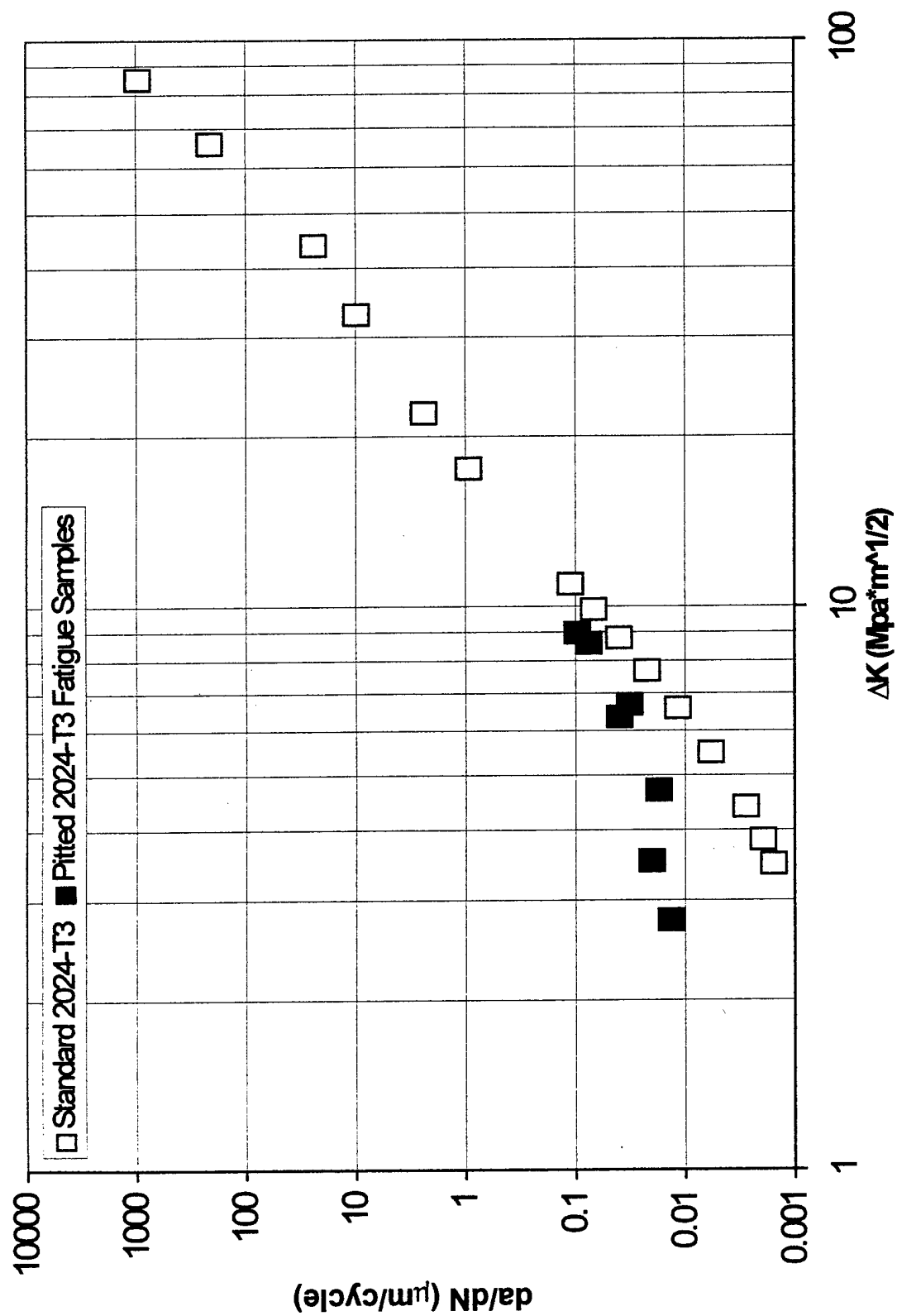


Figure 47. Crack growth rate versus ΔK .

CHAPTER 5

SUMMARY

The results reported in the last chapter were only the initial findings in an ongoing investigation.²⁸ In summary, a technique for creating an accelerated controlled pitting corrosion damage was developed for Al 2024-T3. First, the dog-bone fatigue samples were prepared by masking off most of the sample surface with a waterproof tape. This controlled the number of active sites available where pitting corrosion could occur. The samples were placed in an electrochemical cell using 0.1M NaCl as an electrolyte. The electrochemical cell was attached to a potentiostat and a potentiostatic polarization scheme was used to create the pitting corrosion. All polarization schemes produced the desired pitting damage in less than 24 hours.

The pitted surface of each dog-bone sample was characterized using optical microscopy, WLIM and SEM. Several surface parameters were also calculated, including rms roughness, total pit volume and total mass loss due to pitting.

The samples were then fatigued to failure using high cycle fatigue. The cross section of the fractured surface was examined, and the critical pit depth was determined. The stress intensity factor was also calculated for each sample. A linear relationship between the stress intensity factor and the critical pit depth was established, fulfilling the objective of finding a relationship between a structural integrity parameter and a pitting parameter. The crack growth data initiating from a pit was also modeled. However, the objective of finding a relationship between a structural integrity parameter and an NDE parameter was not realized with this initial controlled experiment.

5.1 FUTURE WORK

The NDE-MURI program is an ongoing work, so presented here are several recommendations for future work.

More experiments similar to the one described in this report must be performed so the behavior of this pitting data can be more accurately modeled. One suggestion is to change the fatigue testing parameters in future experiments. This study was done at one stress range and frequency. If these parameters are varied, the results may lead to the answers of the questions proposed in this report.

Another suggestion would be to vary the pit density and distribution of the samples included in the study. This set of samples did have a variety of pit morphologies, but a wider range should be studied so the pitting process can be thoroughly understood.

The short crack- long crack effect should also be more extensively investigated. This could yield a more accurate model of the crack growth behavior of a crack initiating from a pit.

A final recommendation would be to run many polarization schemes longer than 20 hours. The behavior of the data beyond this point would be very important in answering some of the questions posed in this report.

The data from these experiments may be the key to finding that important relationship that can be used in the field to help predict and prolong the life of this growing aging aircraft fleet.

APPENDIX A

PROJECT DATA

Electrochemical Parameters				Fatigue Parameters		WLM Parameters			
Sample #	coating?	Polarization Time (hrs)	Eoc (mV)	Sample #	cycles to failure	Number of pits	magnification	total mass loss (mg)	total pit volume (µm) ³
L01	no	0	0	L01	85478	0	2.5	0	0
L02	no	0	0	L02	211143	0	2.5	0	0
L03	no	0	0	L03	124333	0	2.5	0	0
L04	no	0	0	L04	390137	0	2.5	0	0
L05	yes	0	N/A	L05	152785	2	2.5	0.0002828	10100
L06	yes	0	N/A	L06	63323	2	2.5	0.0003724	13300
L07	yes	0	N/A	L07	153355	2	2.5	0.0001781	6360
L08	yes	0	N/A	L08	81154	2	2.5	0.00015456	55200
L09	no	4	-561	L09	125825	1	2.5	0.00047320	169000
L10	no	4	-571	L10	96970	1	2.5	0.00075040	268000
L43	no	4	-571	L43	53622	10+	2.5	0.0006552	23400
L12	no	4	-542	L12	39591	6+	2.5	0.0001288	4600
L13	no	8	-571	L13	55230	10+	2.5	0.00057680	206000
L14	no	8	-570	L14	86497	1	2.5	0.0000128	456.56
L15	no	8	-654	L15	54764	10+	2.5	0.0001089	3890
L16	no	8	-541	L16	171681	1	2.5	0.0000138	491.79
L17	no	12	-593	L17	53790	20+	2.5	0.00173880	621000
L45	no	12	-578	L45	60794	10+	2.5	0.00026096	93200
L19	no	12	-544	L19	38175	10+	2.5	0.00012684	45300
L20	no	12	-554	L20	24230	20+	2.5	0.0008988	32100
L21	yes	4	-546	L21	36400	2	2.5	0.00011760	42000
L22	yes	4	-536	L22	151436	7	2.5	0.00026488	94600
L23	yes	4	-504	L23	131662	2	2.5	0.00130760	467000
L24	yes	4	-520	L24	136576	2	2.5	0.00061320	219000
L25	yes	8	-577	L25	55129	10+	2.5	0.00107800	385000
L26	yes	8	-600	L26	73425	1	2.5	0.00140000	500000
L27	yes	8	-552	L27	32461	10+	2.5	0.00047040	168000
L28	yes	8	-560	L28	71480	20+	2.5	0.00061040	218000
L29	yes	12	-481	L29	38171	1	2.5	0.00106680	381000
L30	yes	12	-561	L30	52091	20+	2.5	0.00319200	1140000
L31	yes	12	-618	L31	25084	2	2.5	0.00442400	1580000
L32	yes	12	-586	L32	32961	5	2.5	0.00064680	231000
L33	yes	16	-574	L33	23611	3	2.5	0.00308000	1100000
L34	yes	16	-557	L34	63859	3	2.5	0.00035280	126000
L46	yes	16	-512	L46	27840	2	2.5	0.00140000	500000
L47	yes	16	-575	L47	29688	2	2.5	0.00344400	1230000
L37	yes	20	-566	L37	27555	1	2.5	0.00702800	2510000
L38	yes	20	-591	L38	141808	2	2.5	0.00019320	69000
L39	yes	20	-528	L39	156406	2	2.5	0.00135240	483000
L40	yes	20	-583	L40	45492	2	2.5	0.00669200	2390000
L41	yes	24	-568	L41	60790	10+	2.5	0.00196280	701000
L42	yes	24	-632	L42	133452	10+	2.5	0.00017360	62000
L44	yes	24	-575	L44	108632	2	2.5	0.00742000	2650000
L48	yes	24	-553	L48	44983	10+	2.5	0.00018620	66500

WLIM Parameters				
Sample #	average roughness (μm)	rms roughness (μm)	average pit depth (μm)	deepest point (μm)
L01	0.25661	0.33474	0.000	-2.530
L02	0.17529	0.23388	0.000	-1.660
L03	0.23862	0.30601	0.000	-5.790
L04	0.26091	0.34508	0.000	-7.370
L05	0.31324	0.48276	-10.390	-32.270
L06	0.34317	0.47341	-8.700	-13.000
L07	0.57412	0.75876	-11.240	-34.020
L08	0.64912	0.93686	-15.010	-53.820
L09	14.36000	16.39000	-69.260	-73.520
L10	21.01000	29.14000	-121.670	-126.590
L43	0.37471	0.61126	-14.270	-21.590
L12	0.55402	0.72225	-13.210	-34.000
L13	1.25000	3.03000	-45.000	-58.570
L14	0.45751	0.54006	-3.340	-5.990
L15	0.32306	0.45675	-6.150	-9.970
L16	0.45751	0.54006	-3.340	-5.990
L17	0.77488	1.34000	-19.990	-29.450
L45	0.68526	1.27000	-20.090	-29.370
L19	0.77522	1.10000	-21.820	-44.080
L20	0.76667	1.07000	-16.480	-20.350
L21	0.39960	0.73068	-18.280	-36.270
L22	0.71681	1.15000	-24.340	-32.190
L23	0.82476	2.25000	-47.830	-58.790
L24	1.04000	1.90000	-29.770	-36.210
L25	1.52000	2.86000	-50.360	-66.460
L26	0.62000	3.34000	-80.670	-93.990
L27	0.72642	1.83000	-39.970	-62.950
L28	0.91571	1.64000	-29.000	-40.660
L29	0.62098	1.92000	-41.490	-65.340
L30	3.42000	4.87000	-35.750	-41.120
L31	2.32000	5.61000	-60.840	-64.010
L32	0.87647	1.77000	-33.950	-43.240
L33	2.50000	4.97000	-58.130	-67.040
L34	0.46131	1.52000	-43.990	-69.550
L46	1.12000	2.59000	-40.260	-46.700
L47	1.62000	4.83000	-60.910	-67.940
L37	17.25000	28.37000	-123.600	-134.080
L38	0.92646	1.32000	-19.900	-31.230
L39	1.24000	2.52000	-29.320	-37.760
L40	2.40000	5.85000	-54.870	-60.450
L41	1.15000	3.22000	-39.010	-55.160
L42	0.70762	1.34000	-28.980	-39.430
L44	3.74000	6.84000	-57.060	-51.950
L48	0.81602	1.21000	-20.690	-29.300

BIBLIOGRAPHY

1. Rokhlin, S. I., and Kim, J. -Y. "Fracture Mechanical Analysis of Fatigue Crack Initiation and Growth from Pitting Corrosion", *Second Annual Report for DARPA-MURI under AFOSR grant number F49620-96-1-0442*, (1998) p. A24-2.
2. Alcott, John. "An investigation of Nondestructive Inspection Equipment: Detecting Hidden Corrosion on USAF Aircraft", *Materials Evaluation*, January (1994) p. 64.
3. Chen, G. S., Gao, M., and Wei, R. P. "Microconstituent-Induced Pitting Corrosion in Aluminum Alloy 2024-T3", *Corrosion Science*, Vol. 52, No. 1, (1996) p. 8.
4. Chen, G. S., Wan, K. -C., Gao, M., Wei, R. P., and Flournoy, T. H. "Transition for pitting to fatigue crack growth-modeling of corrosion fatigue crack nucleation in a 2024-T3 aluminum alloy", *Materials Science and Engineering*, A219, (1996) p. 126.
5. Piascik, R. S., and Willard, S. A. "The Growth of Small Corrosion Fatigue Cracks in Alloy 2024", *Fatigue and Fracture of Engineering Materials and Structures*, Vol. 17, No. 11, (1994) pp. 1247-1248.
6. Khobaib, M., Crouch, L. B., Jeffcoate, C. S., Matikas, T. E. "The Role of Corrosion Damage on Crack Initiation", *First Annual Report for DARPA-MURI under AFOSR grant number F49620-96-1-0442*, (1997) p. A16-2-A16-9.
7. Fontana, Mars G. Corrosion Engineering, McGraw-Hill Book Company: New York, (1986) pp. 63-73.
8. Akid, R. "The Role of Stress-Assisted Localized Corrosion in the Development of Short Fatigue Cracks", Effects of the Environment on the Initiation of Crack Growth ASTM STP 1298, (1997) p. 4.
9. Goswami, Tarun K and Hoepfner, David W. "Pitting Corrosion Fatigue of Structural Materials", Structural Integrity in Aging Aircraft, ASME, AD-vol. 47, (1995) pp. 129-130.
10. Frankel, G. S. "Pitting Corrosion of Metals", *Journal of the Electrochemical Society*, Vol. 145, (1998) pp. 2188-2190.
11. Corrosion Mechanisms in Theory and Practice, Marcus, P. and Oudar, J. (Eds.), Marcel Dekker, Inc.: New York, (1995) pp. 201-237.
12. Callister, William D. Jr. Materials Science and Engineering, An Introduction, John Wiley and Sons, Inc.: New York, (1997) pp.185-186.

13. Chen, G. S., Liao, C. M., Wan, K. C., Gao, M., and Wei, R. P. "Pitting Corrosion and Fatigue Crack Nucleation", Effects of the Environment on the Initiation of Crack Growth ASTM STP 1298, (1997) pp. 18-19.
14. Kondo, Y. "Prediction of Fatigue Crack Initiation Life Based on Pit Growth", *Corrosion*, Vol. 45, no. 1, (1989) p. 7.
15. Gamry Instruments, Inc. 734 Louis Dr. Warminster, PA 18974.
16. WYKO Corporation, 2650 East Elvira Rd. Tucson, AZ 85706.
17. Philips Electron Optics, 85 McKee Drive Mahwah, NJ 07430-2121
18. Philips XL DX4I Training Course Manual, April 6-10, 1998, p. 1
19. *Metals Handbook: Properties and Selection*, Vol. 1., 8th Edition, Taylor Lyman (Ed.), American Society for Metals, (1961) p. 917.
20. ASTM B-368, "CASS Solution Composition for Corrosion Pitting Exposure Specimens", American Society for Testing and Materials, Philadelphia, PA.
21. Khobaib, M. "Corrosion Prevention Technology for Advanced Aircraft Coating Systems", *Final Report for U. S. Air Force contract number F33615-94-C-5804*, (1997).
22. Surface Profilers, *Technical Reference Manual*. WYKO Corporation, (1996) pp.4-10.
23. Harmsworth, Clayton L. "Effect of Corrosion on the Fatigue Behavior of 2024-T4 Aluminum Alloy", ASD Technical Report 61-121, (1961).
24. John, Reji. Personal communication.
25. Newman, J. C., Raju, I. S. "Stress-Intensity Factor Equations for Cracks in Three-Dimensional Finite Bodies", *Fracture Mechanics: Fourteenth Symposium-Volume 1: Theory and Analysis*. ASM STP 791, (1983) pp. I-238-I-265.
26. Wilson, Larry. Quantitative Analysis: Gravimetric, Volumetric and Instrumental Analysis, 3rd Edition, Mohican Textbook Publishing Co.: Loudonville, Ohio, (1995) pp. 50-58.
27. Skinn, D. A., Gallagher, J. P., Berens, A. P., Huber, P. D., Smith, J. WL-TR-94-4054, Damage Tolerant Design Handbook, University of Dayton Research Institute, (1994)
28. L. B. Simon, M. Khobaib, T. Matikas "Effect of Pitting Corrosion to Loss of Structural Integrity in Aluminum Alloys" Nondestructive Evaluation of Aging Materials and Composites III, Proceedings of SPIE, 3-5 March, 1999, Newport Beach, CA. pp. 40-47.

ABSTRACT

USE OF WHITE LIGHT INTERFERENCE PROFILOMETRY TO DEVELOP A NONDESTRUCTIVE METHOD TO PREDICT INSTABILITY OF LOADED CRACKS

Schroeder, Jody Lynn
University of Dayton, 2000

Research Advisors: D. Eylon and T. E. Matikas
Faculty Advisor: D. Eylon

A method to characterize the depression zone at a crack tip and predict upcoming fracture under static load using white light interference microscopy was developed and studied. Cracks were initiated in notched Ti-6Al-4V flat specimens through fatigue loading. Following crack initiation, specimens were subjected to static loading during in-situ observation of the deformation area ahead of the crack. Nondestructive in-situ observations were performed using white light interference microscopy. Profilometer measurements quantified the surface area, volume, and shape of the depression ahead of the crack front. Results showed an exponential relationship between the area of the crack tip deformation and volume of the crack tip depression with the stress intensity factor of the cracked sample. This exponential relationship was common to a variety of microstructural conditions such as mill-annealed, duplex, and β -annealed microstructures.

The findings of this study indicate that it is possible to determine a critical rate of change in surface deformation at a crack tip versus the stress intensity factor that can be used to predict oncoming catastrophic failure. This rate measurement can be developed into a new inspection method for predicting impending fracture in cracked loaded aircraft components. Additional

observations from this study include time dependent crack tip depression zone enlargement under sustained load, crack tip deformation relaxation following load release and discrepancies between surface deformation and theoretical plastic deformation shapes.

LIST OF FIGURES

1. 3-dimensional image of depression (often referred to as deformation zone) preceding a statically loaded crack tip.B-101
2. Illustration of grain size affect on plastic zone: (a) deformation area smaller than grain size, (b) same size as grain, and (c) much larger than grain size.B-106
3. Shape of theoretical plastic deformation.B-108
4. Dimensions of Ti-6Al-4V dogbone specimen.B-109
5. Microstructure of Ti-6Al-4V specimens (a) mill-annealed sheet, (b) duplex microstructure forged plate, and (c) β -annealed sheet material.B-110
6. Experimental setup: white light interference profilometer and portable load frame.
.....B-112
7. Schematic of a white light interference profilometer.B-114
8. Determination of zero level by masking higher level data until desired area remains....
.....B-115
9. Profilometer images of accumulating deformation in a mill-annealed specimen (images were taken under load).B-117
10. Profilometer images of accumulating deformation in a β -annealed specimen (images were taken under load).B-118
11. Comparison of 3-dimensional damage zone of mill-annealed specimen prior to static load and after 3114 N.B-119
12. Optical images of depression near crack tip. Mill-annealed material (a) prior to loading and (b) after unloading from 3425 N. β -annealed material (c) prior to loading and (d) following unloading of 2890 N.B-121
13. Deformation and stress factor relationship of Ti-6Al-4V for (a) area of deformation and (b) volume of depression for a variety of microstructures and test orientations.B-124
14. Illustration of microstructure affects on depression size and stress intensity relationship.
.....B-126

15. The highlighted region of this 2-dimensional profile represents the reduced area (A_{red}) of the sample due to surface deformation. This image was taken from a 2-D analysis of the crack tip where the red green and blue lines are representative of a grid over the image (Reference Figure 10).....B-127
16. Theoretical plastic zone compared to surface depression at 3114 N load (image is of mill-annealed material).....B-129
17. Detection of time dependent room temperature deformation at the crack tip zone (mill-annealed Ti-6Al-4V) (a) images taken at initiation of load and (b) images taken after designated elapsed time.B-131
18. Deformation area and depression volume as a function of time (under a static load of 3000 N, duplex material).B-132
19. Depression relaxation after release of load for mill-annealed material.B-133
20. Criteria for failure: critical rate of depression growth with respect to change in stress intensity factor (a schematic).....B-134

CHAPTER 1

INTRODUCTION

Current economic circumstances and policies often require that both military and civilian aircraft remain in service well beyond their design life. Such extended use requires nondestructive testing of key components and application of fatigue crack damage tolerance models to predict the residual life of critical components with detectable flaws. The current damage models used to determine the remaining life of a component are extremely conservative¹. These conservative models, known as "fail safe" standards prevent failures, but also lead to a lower level of component utilization or more frequent and costly inspection.

Nondestructive testing provides important information required for life prediction models. The importance of nondestructive evaluation is indicated in the 1997 NAS/NRC Aging Aircraft Report². In this report, nondestructive evaluation was identified as a priority recommendation. Nondestructive evaluation became a funding priority for the Air Force when the United States developed the ambitious goal to extend the life of several aging aircraft fleets to 80 years of service.

1.1 Use of Titanium in High Performance Aircraft Components

High performance aerospace components are often made of titanium alloys. Thus, titanium alloys are regularly evaluated using nondestructive methods. Prominent components made of titanium alloys include the aircraft fuselage, gas turbine engine disks and blades, landing gears, lower wing skins, and windshield frames³. Many of these components are key structural components that require high strength and damage resistant alloys.

Titanium alloys are used in high performance primary structures because of their toughness, fatigue strength, and corrosion resistance ^{4,5}. Titanium is a high specific strength metal that provides weight savings over steel and aluminum alloys³. Titanium was first used as a structural metal in 1947⁶. Today, titanium is used extensively in high-performance aerospace applications. Titanium is relatively expensive due to high-energy requirements involved in releasing it from its ore⁶. Its high strength, stiffness, toughness, low density, and corrosion resistance often justify the added cost of titanium.

There are a vast range of structural titanium alloys, phases, and microstructures. Titanium exists in two crystal structures: hexagonal closed packed (α -phase) and body centered cubic (β -phase). The β -phase is the more formable phase, while the α -phase is the stronger phase. The two phases often exist together in α - β alloys. The relative amount of each phase is controlled by the presence of alloying elements or interstitial elements. The presence of aluminum, oxygen, nitrogen, and carbon in titanium alloys causes the β transition temperature to raise above the pure allotropic transformation temperature of 885°C. Interstitial hydrogen and alloying elements, including Mo, V, Nb, Cr, and Fe act as β stabilizers and lower the β transus temperature⁷.

Throughout the 50 year existence of the titanium industry, Ti-6Al-4V has been the most used alloy. This alloy accounts for about 45% of industrial applications of titanium and 80-90% of the titanium used on airframes^{3,7}. Ti-6Al-4V is more formable than most other titanium alloys while still maintaining moderate to high structural properties. Ti-6Al-4V is used in gas turbine disks and blades, airframe structural components, and other applications requiring strength and operating temperatures up to 315°C.

The mill-annealed microstructure is the most common condition of Ti-6Al-4V. Duplex and β -annealed microstructures though less common, are used in applications where improved fatigue strength and damage tolerance are required. β -annealed titanium has a high damage tolerance because crack propagation temporarily stops when the crack encounters colony boundaries⁸. This high damage tolerance is required on the critical fittings attaching the composite empennage to the fuselage of the Boeing 777³. Duplex microstructures with similar amounts of equiaxed primary α -phase and fine lamellar transformed α -plates are valued for their high fatigue strength. The equiaxed area is particularly resistant to crack initiation and the lamellar areas resist crack propagation⁹. Duplex microstructures are often used in demanding fatigue critical tasks including fan blade applications.

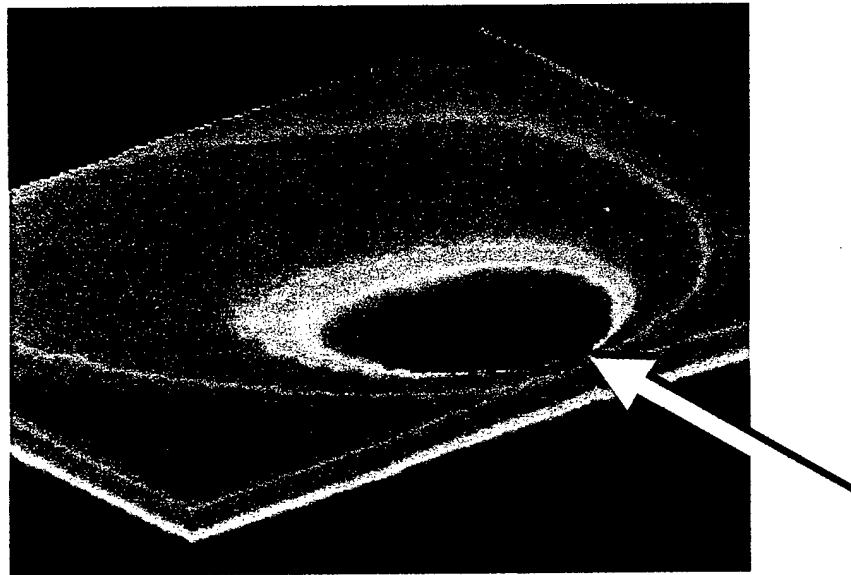


Figure 1. 3-dimensional image of depression (often referred to as deformation zone) preceding a statically loaded crack tip. The arrow point indicates the end of the crack tip.

1.2 Significance of Deformation Zone and Crack Propagation

The three-dimensional deformation zone ahead of a crack tip represents the stress condition of the crack front¹⁰. Many believe that this deformation preceding a crack increases the effective length of the crack and must be considered in life prediction models¹¹. The deformation is a result of complex stresses and strains at the crack tip. The presence of these stresses and strains is exemplified by necking of the material. The localized necking creates a depressed volume in front of the crack tip as shown in Figure 1. When the stresses and strains in the deformation area combine to reach a critical level the conditions for crack propagation are satisfied. The crack extends through microcrack coalescence or increased necking, which causes voids to grow larger¹¹. Through the conditions of its existence the deformation zone can be considered to measure the load history of the material ahead of the crack following its last propagation step.

The deformation zone is a combination of elastic and plastic deformations. The elastic deformation can be recovered while the plastic deformation is permanent. The plastic deformation zone is caused by a stress concentration at the crack tip that exceeds the material's yield strength.

1.3 Fracture Mechanics and Crack Tip Deformation

The Griffith Theory can reasonably predict the onset of rapid fracture in somewhat brittle materials, but fails when applied to ductile materials that experience plastic deformation. In ductile materials, stress states and energy at the crack tip differ greatly from the conditions predicted by Griffith¹². These differences can be related to the amount of plastic deformation present at the point of fracture of a ductile material.

Plastic deformation represents absorbed energy. This absorbed energy creates microscopic shear fracture surfaces instead of directly contributing to crack propagation^{13,14}. The Griffith Theory is based on the assumption that crack propagation occurs when an amount of energy exceeding that required for an increment of crack advance is absorbed. When plastic deformation is large in comparison to the crack length, standard fracture mechanics does not reasonably predict material failure because it fails to account for the energy absorbed by plastic deformation¹³.

The stress intensity factor, K , describes the stress state of a defect within a component. The magnitude of the stress intensity factor changes based on the amount of damage preceding a crack. Accurate determination of the stress intensity factor for cracks with large deformation is difficult. Difficulties arise when the deformation field data extends into areas of the material influenced by the geometry of the specimen. It is also difficult to ensure that the surface

deformations are representative of the displacements occurring throughout the sample bulk. This is guaranteed by taking measurements outside of the area one half of the plate thickness away from the crack tip¹⁵.

The stress intensity factor has been determined in plastically deformed materials by examination of deformations recorded by full-field optical methods. Photoelastic patterns were used by Sanford and Daily¹⁶ in a fringe order calculation method. Smith, et al.¹⁷ determined fracture parameters from moiré interferometry displacement information. Both of these methods were based on data gathered from random points along the deformation. The accuracy of the calculated fracture parameters should improve, as the range of data used in calculations is increased through use of other diagnostic methods¹⁸.

1.4 Need for Novel Surface Technique to Quantify Crack Tip Deformation

Optical stress-analysis methods are extremely important in fracture mechanics. Despite their importance, there is a lack of suitable experimental techniques providing full-field deformation measurement¹⁸. Numerous optical examinations of crack tip deformations have been performed to estimate the stress state of a crack tip. These techniques include the previously mentioned photoelastic methods and moiré interferometry^{19,20,21,22}. Holographic interferometry²³, shearing interferometry^{24,25}, computer vision²⁶, caustics, and numerical analyses²⁷ have also been used for crack tip stress calculations.

All of the procedures above contain a limitation that must be overcome. For instance, photoelasticity requires calibration of each batch of material tested at the time of testing and is limited to specific materials²⁸. In moiré interferometry, extensive surface preparation is required since a physical grating must be applied to the specimen surface prior to examination.

Holographic and speckle interferometries require two exposures of the specimen surface on the same film, one reference exposure prior to deformation and an exposure following deformation²⁹.

White light interference profilometry may become the desired experimental technique for deformation field data acquisition. White light interference profilometry measures the same physical properties as the other optical methods, but white light interference profilometry produces more interpretable topographical images. White light interference profilometry enables non-contact, real-time, high-resolution 3-D evaluation of surfaces. White light interference profilometric data can be quantified and the use of this profilometer requires a less elaborate testing setup than many of the previous techniques.

A white light interference profilometer is essentially a Michelson interferometer with a reference mirror replaced by the surface to be imaged^{30,31,32}. White light interference profilometers can evaluate surfaces with a roughness as high as 500 μm and with an accuracy of 3 nm rms. White light interference profilometry is discussed in detail in section 2.4.

1.5 Objectives of this Work

The overall objective of this study was to develop an enabling methodology to detect and quantify internal damage in materials and components through changes in surface characteristics and then predict oncoming fracture. The detailed objectives were as follows:

- Develop a technique to observe surface deformation at a crack front;
- Demonstrate that quantification of the surface deformation at a crack front is a valid methodology for predicting crack instability;
- Predict oncoming catastrophic failure;

- Report observations of time dependent deformation occurring under a sustained load;
- Investigate and develop relationships accounting for deformation relaxation following load release; and
- Examine material properties, e.g. microstructure and material orientation, which may affect the extent of surface deformation.

1.6 Application of a Novel Optical Surface Diagnostic Technique

This work is one of the first laboratory applications of white light interference profilometry in materials research. White light interference profilometry enables topographical measurements with 3 nm vertical resolution and lateral surface resolutions of up to $0.2 \mu\text{m}^{33}$. Such precision permits detailed topographic imaging. In addition, imaging cycle time for medium resolution scans up to a square millimeter in size is less than 5 minutes. Short scanning times enable in-situ measurements such as the time dependent measurements of crack front deformation performed in this work.

1.7 Shape and Size of Crack Tip Deformation

The size and shape of the deformation ahead of a crack is strongly influenced by Poisson's Ratio and the microstructure of the material. A portion of the deformation results from necking at the crack tip due to stresses perpendicular to the crack. This phenomenon is described by Poisson's Ratio, which is a ratio of lateral and axial strains.

The shape of the deformation is strongly influenced by grain size. For example, when the grain including the crack tip is larger than the deformation zone, the deformation tends to follow the orientation of the grain it is encapsulated in. When the deformation size is equivalent to the

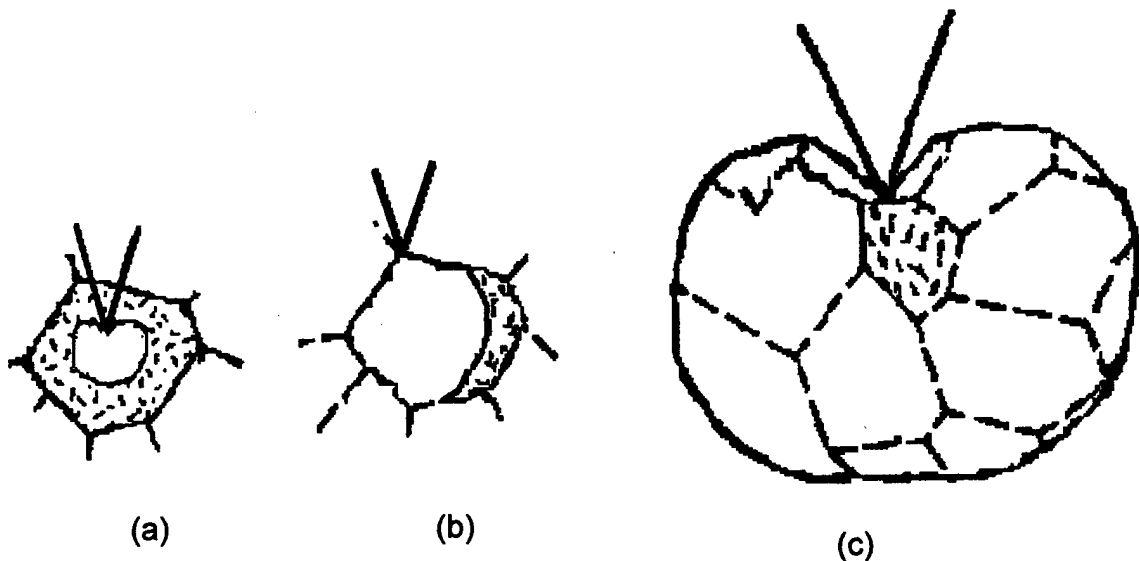


Figure 2. Illustration of grain size affect on plastic zone: (a) deformation area smaller than grain size, (b) same size as grain, and (c) much larger than grain size.

grain size, the deformation will take on the shape of the grain it is in. When the grain size of the microstructure is small compared to the size of the deformation, individual grains will have little influence on the shape of the deformation (Figure 2)¹².

1.8 Distinguishing the Components of Surface Deformation

The deformation observed on the surface of a sample is a combination of elastic and plastic deformation. To distinguish the two types of deformation a technique other than white light profilometry must be applied. Standard techniques that identify plastic deformation include isochromatic-fringe experiments, photoelastic coating methods, etch-pit techniques, electrolytic

etching, microhardness methods, electron channeling, X-ray diffraction, channeling contrast in scanning electron microscopy and stereographic techniques¹¹.

Assuming elastic deformation is negligible, the size of the deformation zone can be estimated using standard fracture mechanics equations that calculate the radius of plastic deformation (Equations 1a & b). These equations are valid for applications where monotonic stress is present. When cyclic stresses are applied the size of the plastic zone is greatly reduced. The cyclic deformation zone is estimated to be 1/5 the size of a monotonically loaded

$$r_y = \frac{K^2}{6\pi\sigma_{ys}^2} \quad (a) \qquad r_y = \frac{K^2}{2\pi\sigma_{ys}^2} \quad (b)$$

Equation 1: Plastic deformation size (a) plane strain (b) plane stress
deformation zone¹¹. A plane stress equation is used for plastic deformation radius equations in this work. The plane stress condition is valid for this work both because of the thickness of the samples and the comparison of plastic deformation calculations to surface deformation measurements. First of all, the samples were thin enough for the plane stress state to exist throughout the thickness of the sample. Secondly, this study is based on deformation measurements on the surface of the sample where the plane stress state is guaranteed to be present no matter what the sample thickness due to the lack of the 3-dimensional stress state on the sample surface.

The shape of the plastic zone also affects the life of structural components. Equations 1a and b simply supply the average radius of the plastic zone. Theoretical plastic zone shapes are not circular so an angular dependent radius of plastic deformation equation is needed. This equation is presented as Equation 2. Plotting this radius provides the theoretical plastic deformation shape for plane stress conditions of a crack at a particular stress intensity value¹². This theoretical shape resembles a butterfly as seen in Figure 3.

$$r_y = \frac{K^2}{2\pi\sigma_{ys}^2} \cos^2 \frac{\theta}{2} (1 + 3 \sin^2 \frac{\theta}{2}) \quad \text{Equation 2}$$

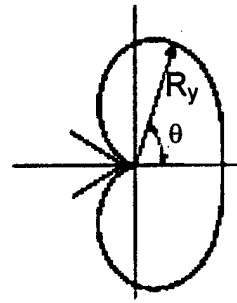


Figure 3. Shape of theoretical plastic deformation¹².

CHAPTER 2

EXPERIMENTAL PROCEDURES

Three different microstructures of Ti-6Al-4V were studied in this work to quantify the effect of microstructure on crack tip deformation size and shape. All samples were flat 79 mm long dogbone specimens (Figure 4). Through electro-discharge machining, a 0.4 mm long notch was cut into the edge of the center of the reduced section of each specimen to provide a stress concentration for crack initiation. All specimens were polished to a low surface roughness ($\text{RMS} \approx 250 \text{ nm}$) prior to testing to provide a uniform surface finish and enable detailed examination of changes in surface topography.

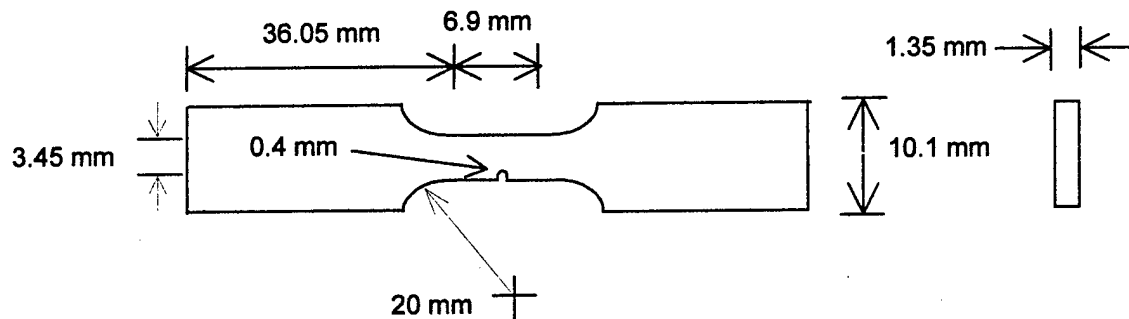


Figure 4. Dimensions of Ti-6Al-4V dogbone specimen.

2.1 Material

Ti-6Al-4V was investigated in this project. The primary microstructure was a mill-annealed sheet 1.35 mm thick annealed at 1300 °F. The microstructure of this material is shown in Figure 5a. This sheet material was cross-rolled with the final rolling direction being the direction indicated in Figure 5a. The mill-annealed microstructure had grain sizes of approximately 5 μm in the transverse direction and 20 μm in the longitudinal direction (Figure 5a). Both longitudinal and transverse orientation behavior of this material was investigated.

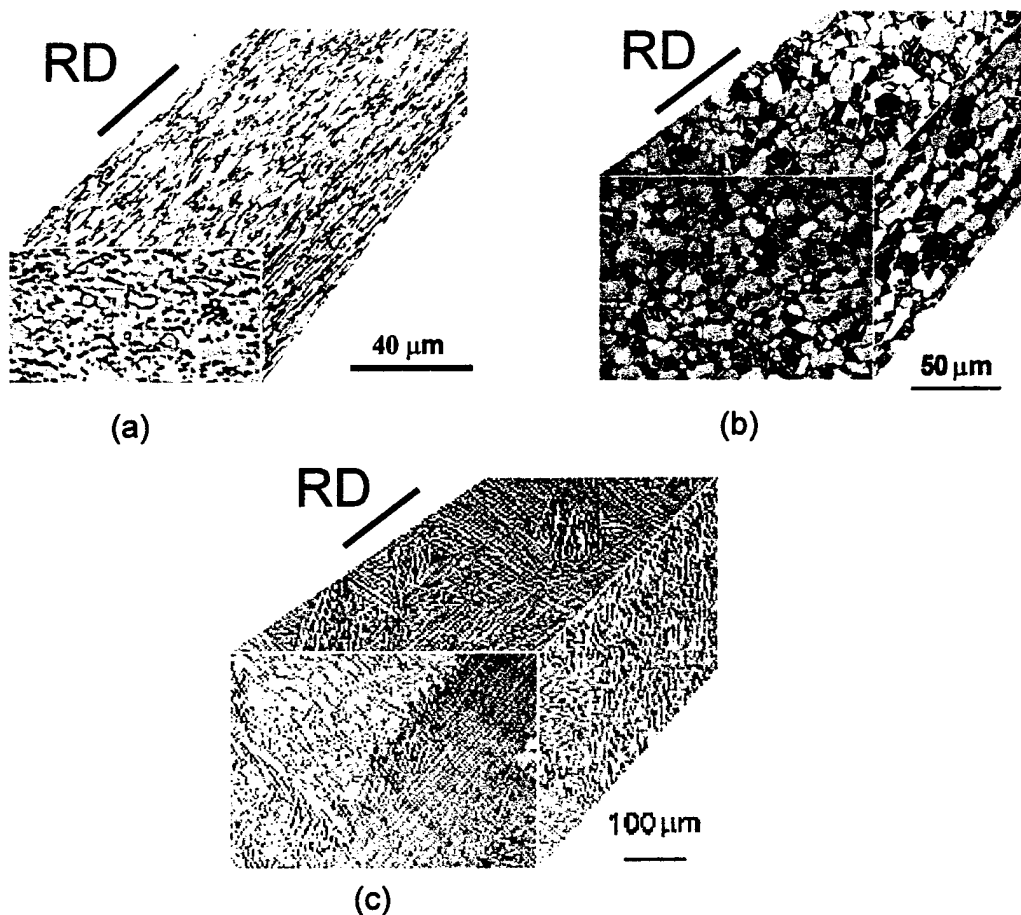


Figure 5. Microstructure of Ti-6Al-4V specimens (a) mill-annealed sheet, (b) duplex microstructure forged plate, and (c) β -annealed sheet material.

The duplex microstructure (Figure 5b) was obtained from a plate that was forged and solution treated in the $\alpha + \beta$ phase field. Solution treatment was done at 1710°F for one hour in an air furnace and then forced air convection cooled. This was followed with a 1300°F vacuum anneal. The resulting material was 60 volume percent equiaxed primary alpha and the microstructure is therefore directionally independent. The average equiaxed grain size was approximately 10-20 μm (Figure 5b).

The final microstructure examined was a β -annealed sheet. This sheet's origin was identical to the mill annealed material. It was vacuum heat treated above the β transus at 1900°F for 6 hours and then furnace cooled. It was then vacuum annealed at 1300°F for 1 hour and 40 minutes and air-cooled. Most colony sizes were between 100 and 200 μm (Figure 5c). Preparation of β -annealed specimens included etching of the specimen surface prior to crack initiation. Etching revealed the microstructure of the specimen and enabled evaluation of the influence of each large grain on surface deformation orientation and shape.

2.2 Crack Initiation

Fatigue cracks were initiated from the notch of each specimen by high cycle fatigue loading. The specimens were subjected to low stress (~25% of yield stress) cyclic loading at a stress ratio of 0.1. 10,000 cycles were run during each set to initiate a short crack. Following each set of cycles the specimen surface was examined with a traveling optical microscope. Once a visible crack was detected the stress was reduced by 10% and the specimen was subjected to additional sets of 1000 cycles. Prior to each additional set, the stress was reduced another 10%. This stress reduction was repeated several times to sharpen the crack front and reduce the initial

surface deformation area (see Equations 1a and b). The crack length ranged from 0.05 to 0.25 mm. Including the notch, effective crack length ranged from 0.45 to 0.8 mm.

2.3 Observation of Crack Tip Deformation Zone

Following crack initiation, the specimens were loaded into a portable static 4500 N (1000 lb.) load frame. The load frame was placed under a white light interference profilometer for in-situ topographical data acquisition. The combination of the profilometer and load frame, as shown in Figure 6, allowed documentation of changes in the topography of the material during application of a static load.

The presence of a depressed zone ahead of the crack tip was recorded. This depression was imaged, characterized, and quantified with white light interference profilometry.

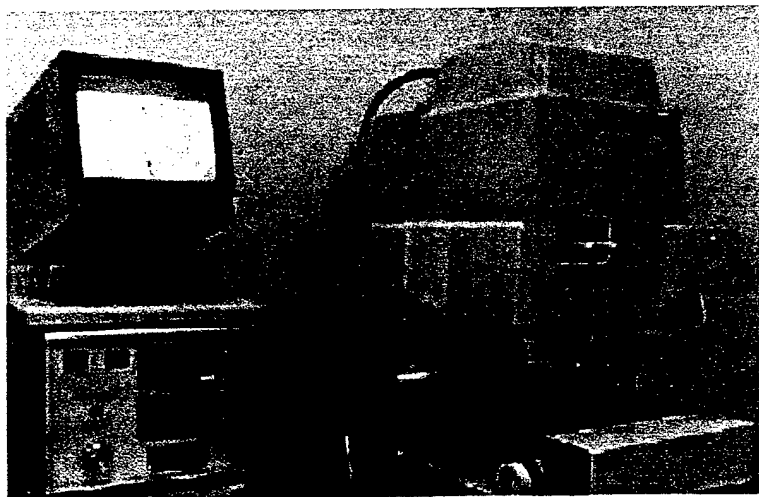


Figure 6. *Experimental setup: white light interference profilometer and portable load frame.*

Quantification included determination of the depression volume, surface area of the deformation, and aspect ratio of the deformation.

2.4 White Light Interference Profilometry

Primary material evaluation throughout this work was performed with a vertical scanning white light interference profilometer. A white light interference profilometer is essentially a Michelson interferometer with a reference mirror replaced by the surface to be imaged^{30,31,32}. Profilometers enable non-contact, real-time, high-resolution 3-D evaluation of surfaces with a roughness as high as 500 μm and an accuracy of 3 nm rms. Utilization of phase shifting measurement techniques on the profilometer can increase the accuracy to 3 Å.

White light interference profilometers provide a white light source that is split into two beams. One reflects off the surface of the sample and the other reflects off a reference mirror (Figure 7). The two reflected beams recombine to form interference fringe patterns. Fringe contrast maximizes at the minimum optical path difference between the reference and measurement beams. The fringes at this point represent the surface area of the sample that is in focus. Since the optical path difference and thus fringe modulation varies from point to point on rough surfaces, vertical scanning is required to map the entire surface. A piezoelectric transducer enables vertical scanning or precise movement up and down the z-axis. Typical transducers move the reference mirror in steps of 0.05 to 0.1 μm over a distance of nearly 1000 μm (1 mm). Throughout vertical scanning, a CCD camera captures the fringe modulation. The region of interference is then recorded for each pixel and related to the location of the reference mirror along the z-axis. Digital signal processing hardware then demodulates the fringe data in real time. The result is a fast three-dimensional profile of a surface³⁰. White light interference profilometers also enable areas of a surface to be separated by surface height without the complexity and high cost of confocal instruments³⁴.

The instrument used in this study is capable of 3 nm vertical resolution and has a lateral surface resolution of 0.2 μm . This profilometer also has an image analysis package that enables automated topographical calculations including height profiles, threshold surface area, and surface depression volume analysis, along with other calculable parameters that are not used in this analysis.

2.5 Quantification of Topographical Data

In this work, a "threshold analysis method" was used to separate surfaces of different heights. Following height separation it was possible to quantify the volume and surface area of the regions of depressed height. In threshold analysis, all pixel points representing regions lower than the threshold value are summed for calculation. The profilometer software permits image quantification based on height or separation. Height calculations provide the area of each separate height region. A third method, the separation method, can only distinguish areas that are completely separated from the rest of the image either by user masking or by a distinct drop off (step height change).

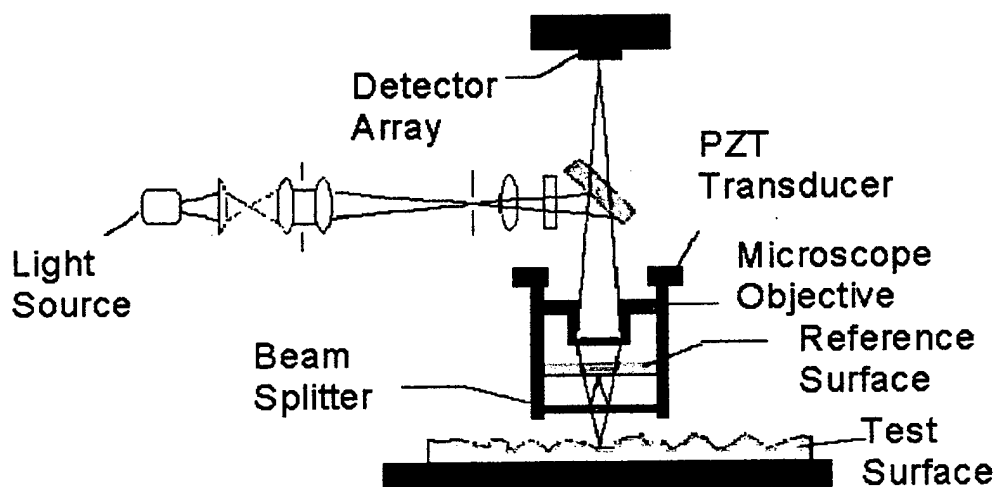


Figure 7. Schematic of a white light interference profilometer.

The threshold method was selected because it allows the user to set a numerical cutoff between the areas of depression and the gradual slope of the material into the background. A value of zero is the cutoff for evaluation of this data. The zero threshold represents the region level with the bulk sample surface. All regions below this threshold will be summed for deformation calculations. The bulk surface or zero reference was reproduced by focusing the profilometer on the same point of the bulk surface for each measurement. In this work, the focus point was the left side of the crack tip.

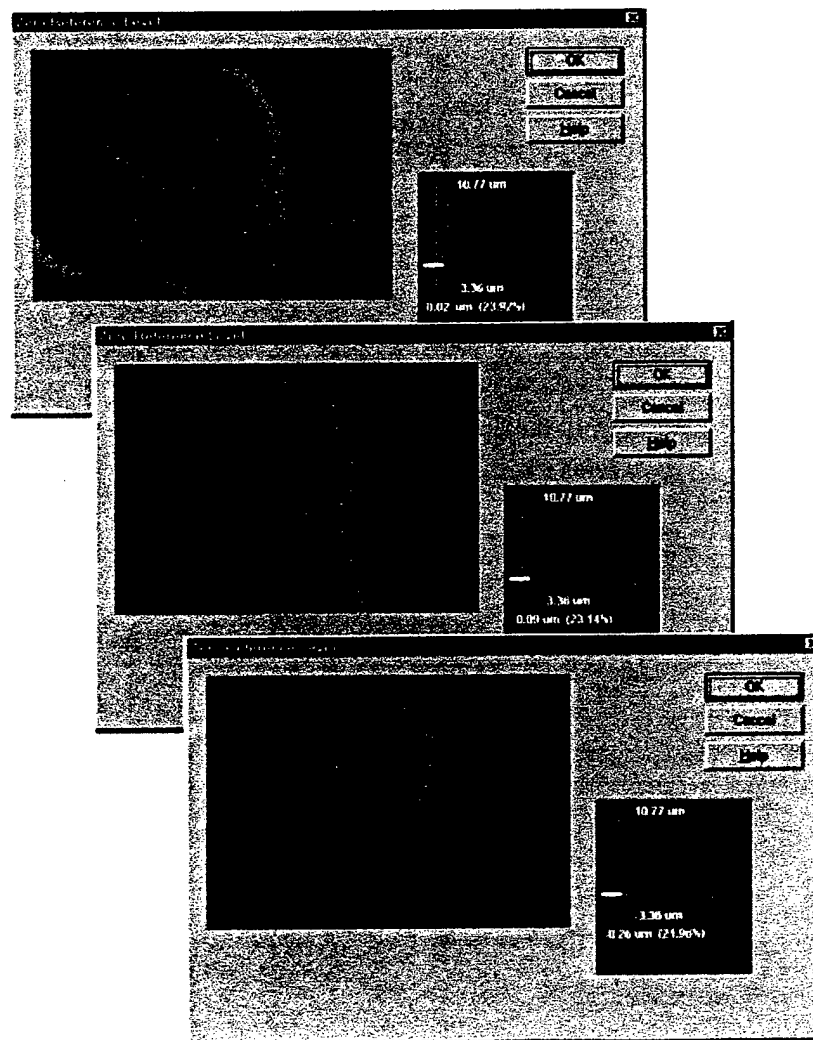


Figure 8. Determination of zero level by masking higher level data until desired area remains.

In early images, when there is little to no area of deformation, it is difficult to identify a specific area of the material surface and the point of focus may vary. This error is corrected by altering the zero-value for images of concern. The desired zero value is chosen through manual masking. The user views an image that only shows the area below the new zero threshold. When the desired area is all that remains a new zero value is selected and calculations ensue. This procedure is illustrated in Figure 8.

The threshold method provides numerical values for the surface area of the deformation or volume of the surface depression by summing up all of the points representative of data points below the threshold height. This number of points is multiplied by the unit area value per pixel for surface area calculations. Volume calculations require that the representative height of each pixel is also considered and a related pixel volume value is multiplied by the number of pixels at each height. The resulting value is presented as either the deformation surface area or volume of the depression zone.

2.6 Image Preparation for Calculations

The quantity of the deformation found through threshold calculations is extremely dependent upon the image under examination. If the image examined encompasses a large amount of the actual crack the deformation value will contain the area of the crack. It is necessary that each image examined be of a similar area of the specimen. Sample images used in deformation quantification calculations are contained in Figure 9 (mill-annealed material) and Figure 10 (β -annealed material). Images of the duplex microstructure are not included since they resemble the mill-annealed images (Figure 9). Figure 11 shows a two- and three-dimensional analysis of images of a mill-annealed specimen.

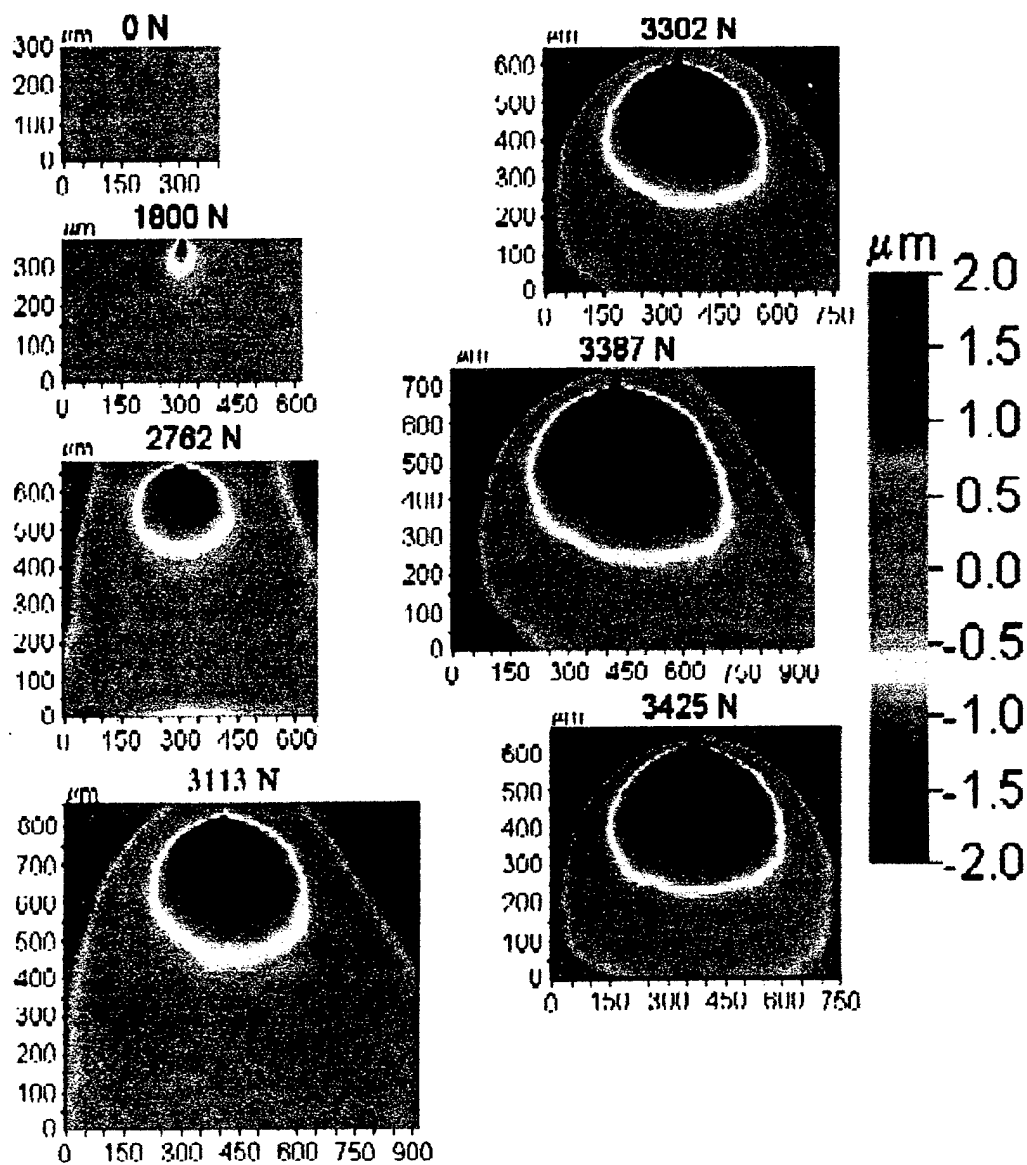


Figure 9 Profilometer images of accumulating deformation in a mill-annealed specimen (images were taken under load).

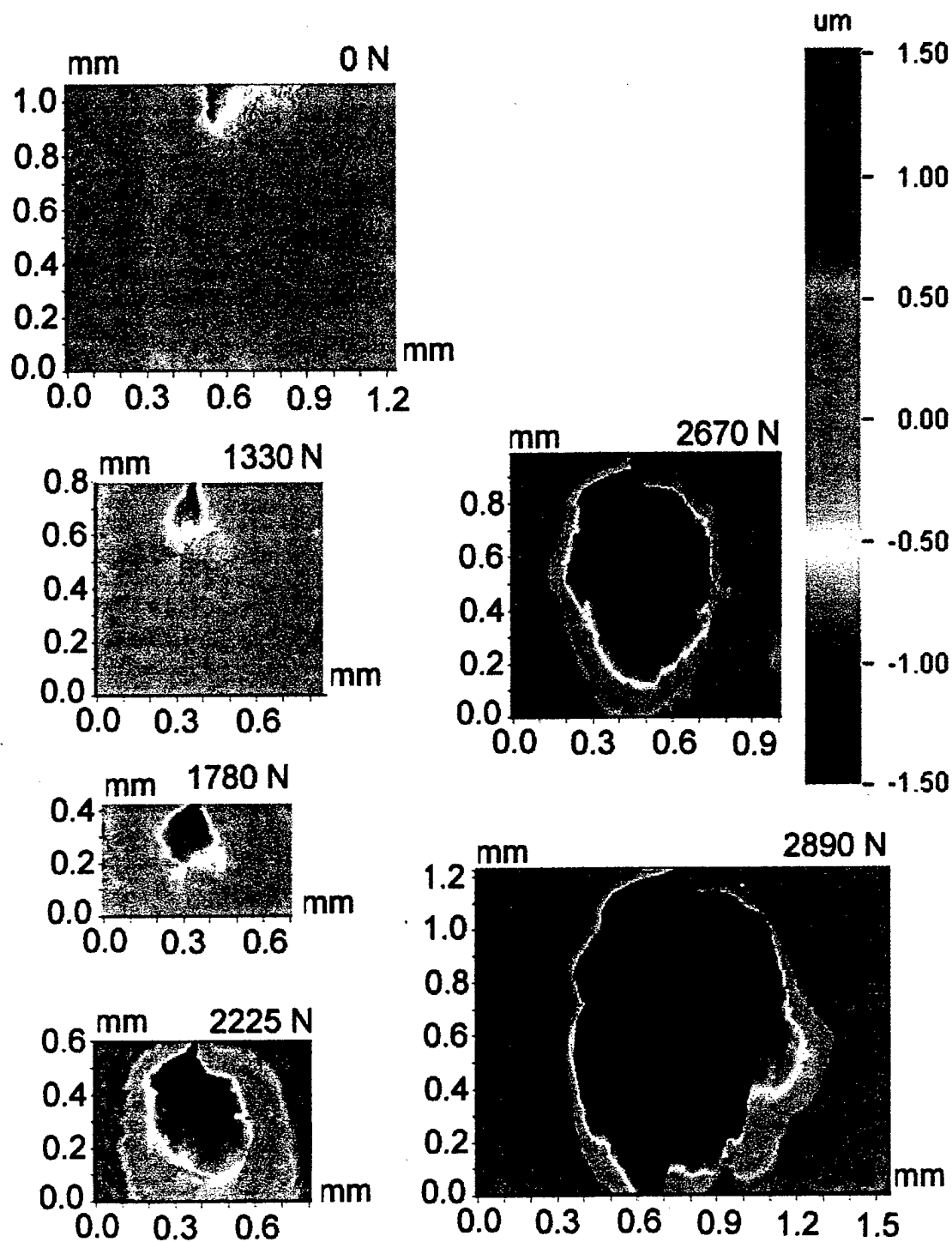
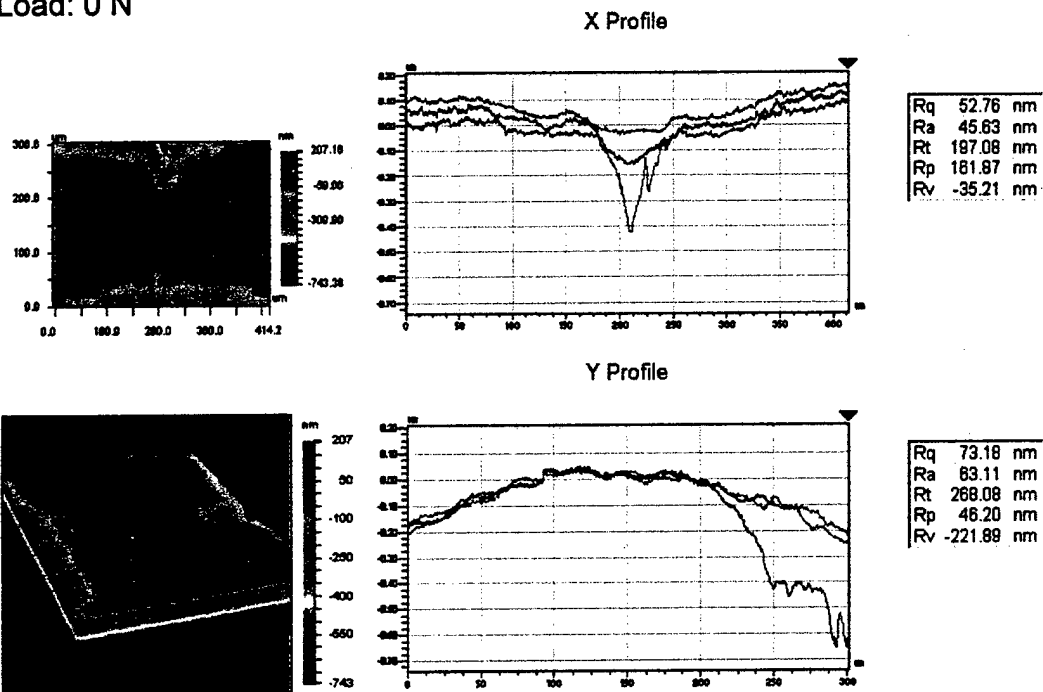


Figure 10. Profilometer images of accumulating deformation in a β -annealed specimen (images were taken under load).

Load: 0 N



Load: 3114 N

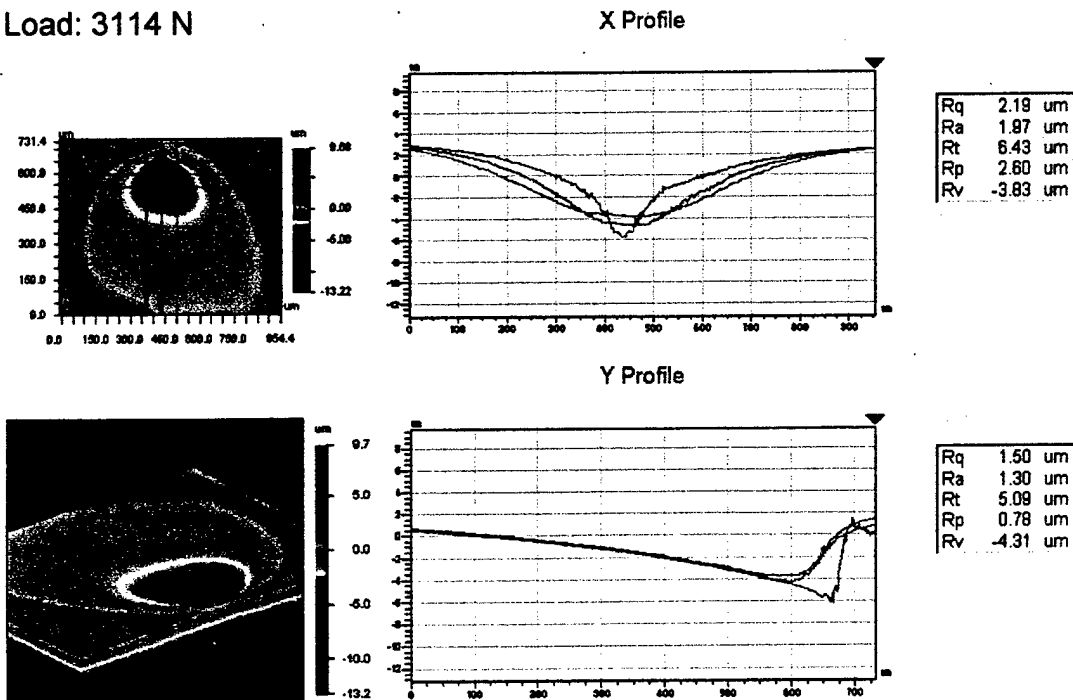


Figure 11. Comparison of 3-dimensional damage zone of mill-annealed specimen prior to static load and after 3114 N.

CHAPTER 3

RESULTS AND DISCUSSION

The scope of this work can be separated into the study of several crack tip surface deformation phenomena. These phenomena include:

- quantitative relationships observed with white light interference profilometry during incrementally increased static loading;
- dependence of deformation size and shape on microstructure;
- disagreement between crack tip surface deformation shape and theoretical plastic deformation shape;
- time dependent deformation growth; and
- elastic deformation relaxation.

3.1 Incrementally Increased Static Load Results

The crack tip deformation zone size of pre-cracked material was monitored under increasing load until failure. Figure 12 shows optical images of cracks in both mill-annealed and β -annealed material prior to static loading and after release of a near critical load. The deformation zone of the mill-annealed material is contained within the area marked by residual shear bands (Figure 12b). The deformation zone of the β -annealed material extends beyond the crack tip opening (compare Figures 12d and 10). The crack front of the β -annealed material is more jagged because it follows the grains of the coarse microstructure. The area ahead of the crack front in the β -annealed material contains several small cracks that were created by crack

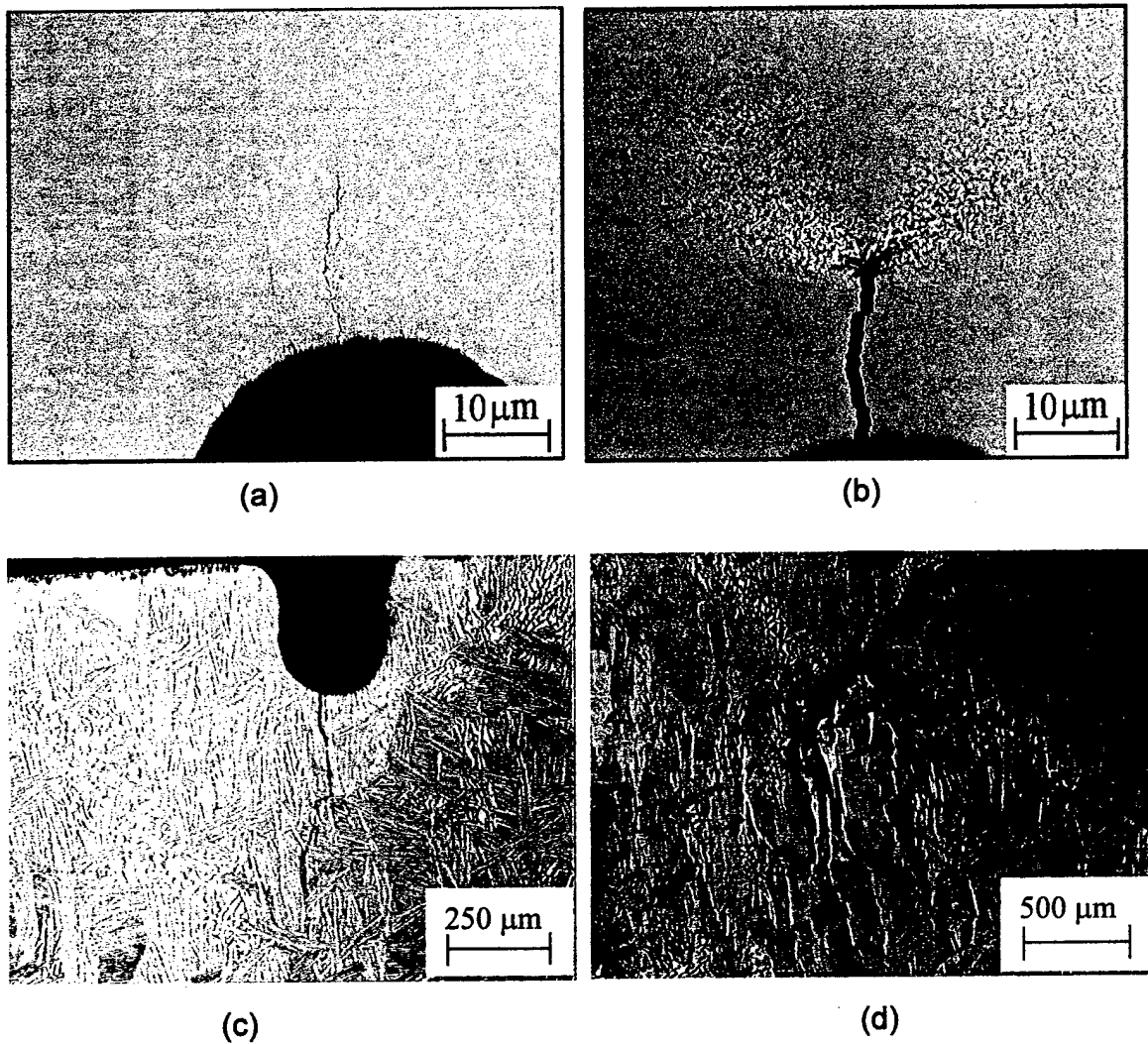


Figure 12. Optical images of deformation near crack tip. Mill-annealed material (a) prior to loading and (b) after unloading from 3425 N. β -annealed material (c) prior to loading and (d) following unloading of 2890 N.

branching. Also note that the crack length of both materials remained constant throughout loading until the point of unstable crack growth (Figures 12b and 12d).

3.1.1 Profilometric Images

Profilometry was proven to be a valid nondestructive technique for qualitative investigation of the surface deformation ahead of a crack tip. Representative visual results of the

surface damage as imaged by the profilometer are shown in Figures 9 and 10. The data provided in Figures 9 and 10 were gathered under load so both plastic and elastic deformations exist.

The images in Figure 9 are similar to the images obtained for all mill-annealed and duplex microstructures. The presence of a distinct region of deformation ahead of the crack is shown in Figure 9. The deformation in β -annealed specimens is illustrated in Figure 10. The deformation in the β -annealed material is uneven and varies specimen to specimen as expected for a very coarse grain material. This variation is a result of the dependence of the deformation direction upon the orientation of the coarse grains in this microstructure.

3.1.2 Stress Intensity Factor Calculations and Consideration

It was assumed that the deformation zone size would rapidly increase when the applied load developed to stress intensity - K levels close to the critical stress intensity factor - K_Q . The critical stress intensity factor, K_Q , for plane stress, is referred to in this work instead of K_{IC} , the critical stress intensity factor for plane strain, because the stress state is dependent on the thickness of the thin samples used in this work.

When the K level in the cracked component reached the K_Q value, fast fracture developed. The K_Q values discussed here were easily obtained from valid plain stress fracture toughness tests. When the K_Q value was reached it was impossible to stop or slow the failure. For this reason, the surface area of the deformation and volume of the depression zone, as determined by the profilometer, were plotted against the stress intensity factor. A relationship resulted from trends in the changes of surface deformation during the approach to K_Q .

Test conditions at the point of fracture of the first sample of each material enabled calculation of the alloy K_Q . The calculated K_Q of the material provided a better-estimated stress

under which each group of samples would fail. This enabled better examination of the region directly prior to the critical load and allowed a more precise study of the nature of crack instability and better prediction of failure.

3.1.3 Analysis of Profilometric Images

Quantified data from the incrementally increased static load tests is shown in Figure 13. Area and volume data was calculated through analysis of images like those contained in Figures 9 and 10. The region of deformation ahead of the crack increased exponentially both in area and volume with the increasing stress intensity factor (Figure 13). Directly prior to failure the area of deformation retracts for almost all samples (Figure 13a). Unlike area, the deformation volume continually increases with K until the final failure (Figure 13b). The consistency of the deformation volume and stress intensity factor relationship makes this comparison a viable tool for failure prediction.

Data analysis indicates an exponential increase in the slope of the deformation volume versus stress intensity factor that indicates an upcoming plastic instability. Detection of this sudden increase in the slope of deformation volume over stress intensity factor may become a useful tool in anticipating eventual instability and may be a basis for methods to detect the beginning of fast fracture in structural components with sharp notches or existing cracks.

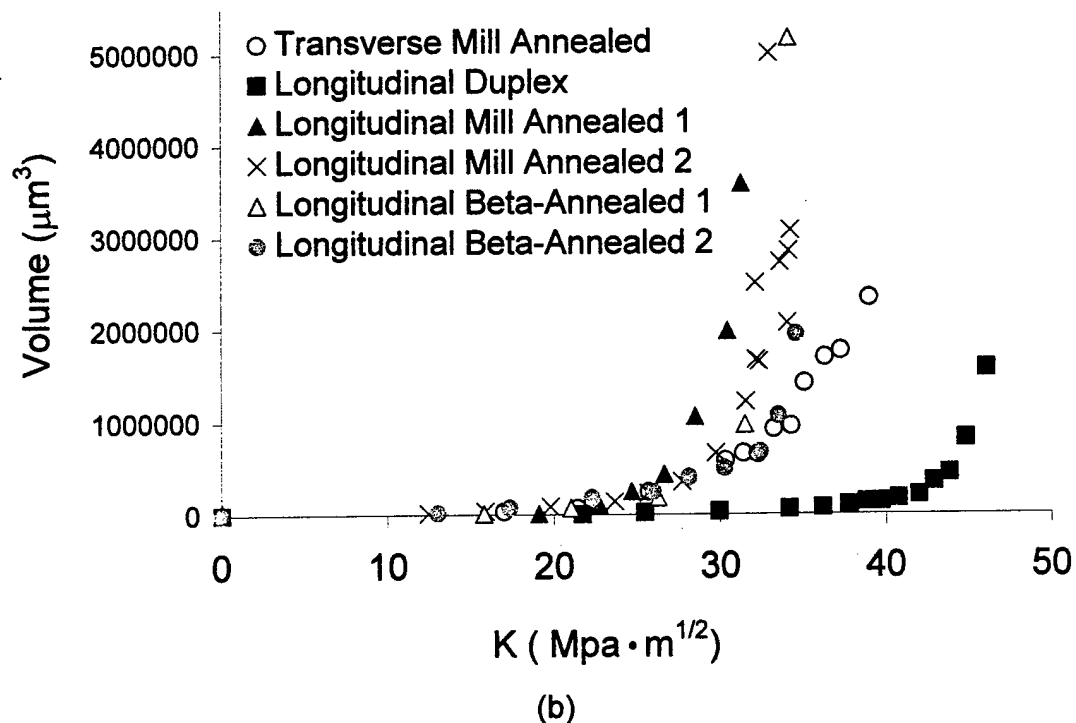
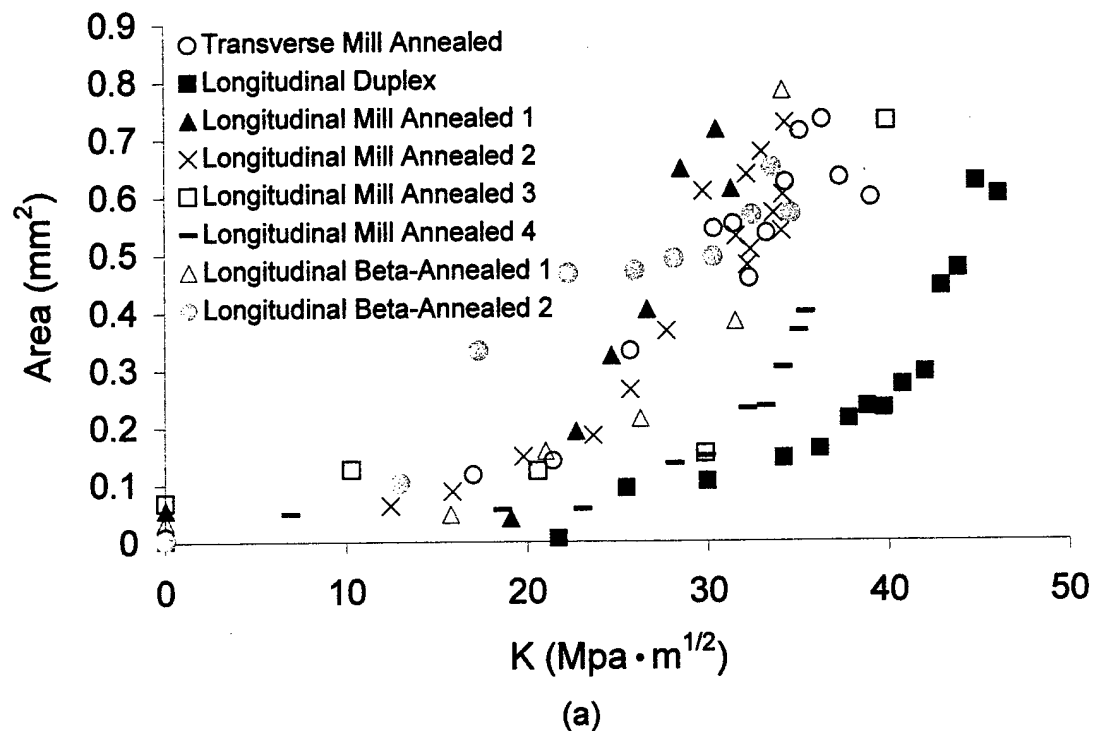


Figure 13. Deformation and stress factor relationship of Ti-6Al-4V for (a) area of deformation and (b) volume of depression for a variety of microstructures and test orientations.

3.2 Deformation Shape and Size

Profilometric data shows a distinct deformation shape that is common for all mill-annealed and duplex microstructure specimens tested. This shape is shown in Figure 9. The general shape of the deformation remains the same from the beginning of loading through development of crack instability. The deformation continues to accumulate as the magnitude of the load is increased. The symmetrical shape shown in Figure 9 is typical of relatively fine-grain materials like the mill annealed and duplex microstructures used in this study. Coarse-grain or highly textured materials like the β -annealed microstructure develop a less symmetric plastic zone because the plastic deformation slip activity ahead of the crack tends to follow large grains oriented for easier slip or a preferred crystallographic orientation (Figure 10).

Original deformation investigations included efforts to relate the development of deformation symmetry to failure prediction. Another investigation analyzed the relationship between the aspect ratio of the deformation and oncoming failure. It was discovered that such correlations were not indicative of upcoming failure. Instead, the deformation shape is due entirely to the influence of microstructure. The discrepancy between Figures 9 and 10 clearly illustrates the dependence of deformation shape on the microstructure of the material.

3.2.1 Influence of Microstructure on Deformation Size

Three microstructures and two material orientations have been tested. Each microstructure variance causes a slight change in the magnitude of the relationship between the deformation size and the stress intensity factor, but all materials tested behave similarly. The magnitude difference between materials can both be anticipated and explained. The slope of the deformation versus K curve approaches infinity at the K_Q of each material. Thus, if the K_Q of a material is known its behavior can be approximated. In this study the magnitude or K_Q of the β -annealed material is much lower than expected⁶. This discrepancy may be the result of embrittlement that occurred when the sheet material was air contaminated during heat treatment.

The described behavior and magnitude dependence is shown in Figure 13, but is schematically represented in Figure 14. The indicated relationship with K can be shown with

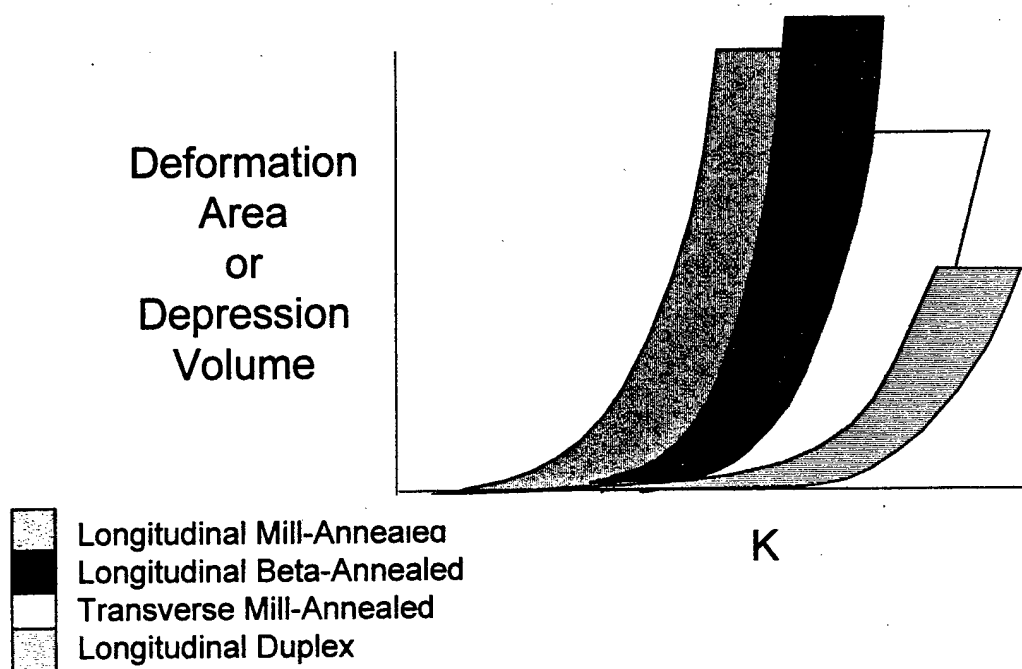


Figure 14. Illustration of microstructure affects on deformation size and stress intensity relationship.

both deformation surface area and depression volume data. However, data scatter is much lower in depression volume analysis making this the relationship of choice for a practical inspection method.

3.2.2 Effects of Depression Volume on the Specimen Cross-Sectional Area

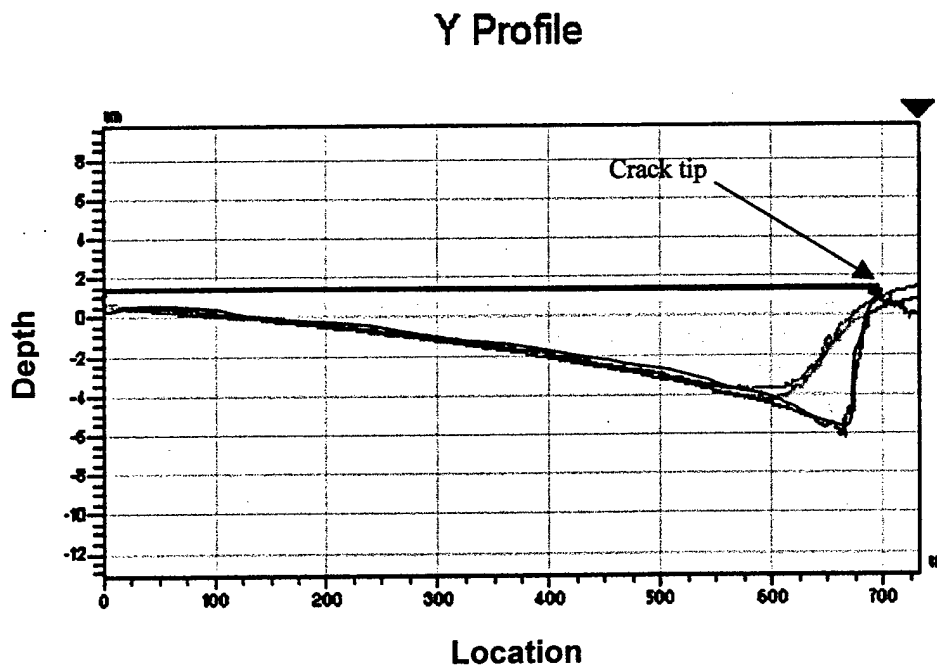


Figure 15. The highlighted region of this profile represents the reduced area (A_{red}) of the sample due to surface deformation. This image was taken from a 2-D analysis of the crack tip where the red green and blue lines are representative of a grid over the image (Reference Figure 11).

Original stress intensity calculations were based on engineering stress or the load per cross sectional area of the original sample. As damage accumulated, the thickness of the sample at the crack tip zone was reduced and proper comparisons required true stress calculations. The reduction in cross sectional area for a mill-annealed specimen near its critical load is illustrated

as a 2-dimensional plot in Figure 15. The data presented in Figure 15 is from Figure 11. The true cross sectional area was calculated using Equation 3. This equation is based on the assumption that the depth of the deformation is equivalent on both sides of the sample. The true stress varied negligibly from the original engineering stress values so further analysis of the affect of the reduction of specimen thickness due to the deformation was disregarded in this study. The relative affect of this cross sectional area reduction is highly dependent upon the original sample thickness. Thin samples will be greatly affected by a minor cross section reduction while thick samples will be negligibly influenced.

$$A_{\text{true}} = A_{\text{eng}} - 2(A_{\text{red}}) \quad \text{Equation 3}$$

3.2.3 Correlating the Observed Surface Deformation and Plastic Deformation

A correlation between the observed surface deformation and plastic deformation is necessary to relate this work with accepted fracture mechanics laws. A rough comparison of theoretical plastic deformation and surface deformation was created by plotting the theoretical radius of plastic deformation for a K level equivalent to that documented for a surface deformation image. The theoretical equation plotted (Equation 2) describes the radius of plastic deformation of a material in the plane stress condition and is based on an in-plane two-dimensional model. This equation is valid since the samples used in this work are thin enough for the plane stress condition to exist throughout their entire cross-section, but is only a broad comparison since the surface deformations represent out-of-plane displacement or displacement perpendicular to the theoretical modeling plane.

The theoretical radius was calculated, plotted as a function of θ , and then sized to correlate to the figure over which it was overlaid. The theoretical plastic deformation shape did not represent the surface deformation (Figure 16). The difference in shape was justified because the kidney shape represents the in-plane material behavior and the shape seen on the surface is the result of out of plane displacement.

The discrepancy in size may also result from the inclusion of both elastic and plastic

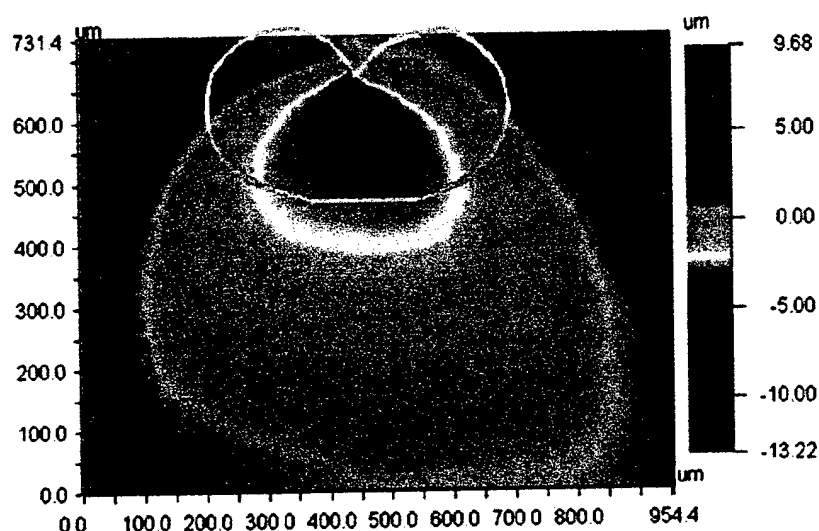


Figure 16. Theoretical plastic zone compared to surface deformation at 3114 N load (image is of mill-annealed material).

contributions to the surface deformation. If these contributions were separated, one may discover that only the deepest area of deformation is representative of plastic deformation. With such consideration, the theoretical plastic zone size may more closely represent the experimental plastic zone size. Quantifying plastic deformation in samples with known amounts of surface deformation may identify the threshold plastic deformation height. Accepted techniques for such measurements were presented in the introduction. Even with a threshold defined for plasticity

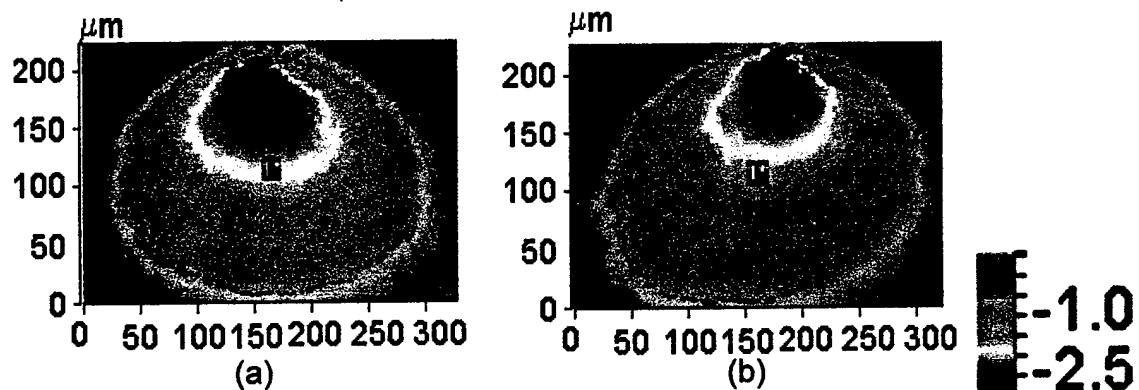
visual observations still suggest that the experimental and theoretical plastic zone shapes will not correlate well.

3.3 Deformation as a Function of Time

Damage accumulation during extended length static loads was observed during testing. The increase in deformation surface area during the application of a maintained static load is shown in Figure 17 for two separate loads. The images in Figure 17 are from a mill-annealed sample. An image was taken at the initiation of a load step and then another image was taken after a specified amount of time. Note that the rate of deformation accumulation increases substantially as K_Q is approached.

To further investigate deformation accumulation under a maintained load, multiple images were taken of a loaded specimen over an extended period of time. Examination of the data revealed that the deformation zone expands under static loading. During the initial hour of loading the increase in deformation size is substantial. After several hours, the rate of increase in the deformation zone size drops considerably (Figure 18). This decrease in rate may be partially related to a negligible release of load that occurs as the deformation increases. This load release is less than 1% of the total load.

Images taken at load of 2722 N. Time elapsed between images is 0:48:24. Surface area increased from 0.033 mm² to 0.034 mm²



Images taken at load of 3114 N. Time elapsed between images is 0:08:04. Surface area increased from 0.048 mm² to 0.050

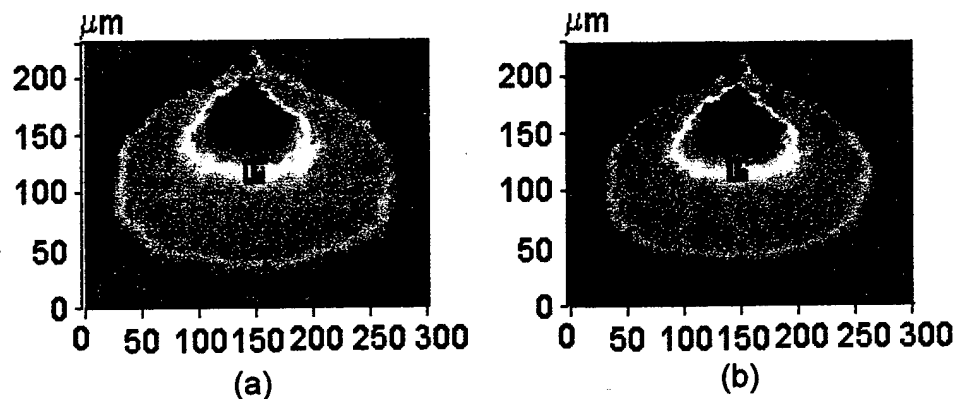


Figure 17. Detection of time dependent room temperature deformation at the crack tip zone (mill-annealed Ti-6Al-4V) (a) images taken at initiation of load and (b) images taken after designated elapsed time.

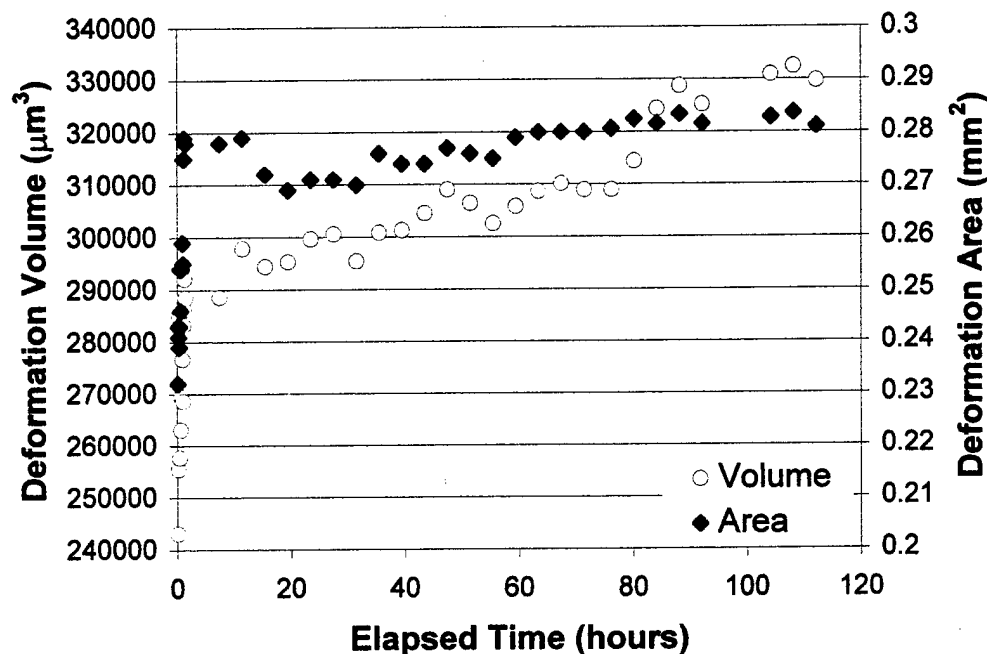


Figure 18. Deformation area and depression volume as a function of time (under static load of 3000 N, duplex material).

3.4 Deformation Relaxation

The surface deformation investigated throughout this work includes both plastic and elastic contributions. A substantial amount of the elastic deformation was expected to relax upon release of the static load. To track this deformation retraction, images were taken of the specimen under load and then directly following release of the load. Measurements showed a minimal decrease in the deformation area. This strain release was time dependent and could be traced over a period of several hours. An additional study was performed to determine if the relative amount of elastic to plastic deformation decreased as deformation size increased. The relationship between elastic and plastic deformation was tracked by loading a specimen to a specific load, imaging the sample under load, releasing the load, and immediately imaging the

sample without load. The result of this test is presented in Figure 19. The duration of time the sample was under load was relatively constant for all load steps. The percent of relaxed deformation was calculated at each load step using Equation 4. At loads up to $\frac{1}{2}$ the critical load of the sample just over 20% of the deformation relaxed upon release of the load. At loads over $\frac{1}{2}$ of the critical load 60% of the deformation relaxed. Most importantly, after deformation relaxation the exponential relationship between the deformation size and the stress intensity factor remained.

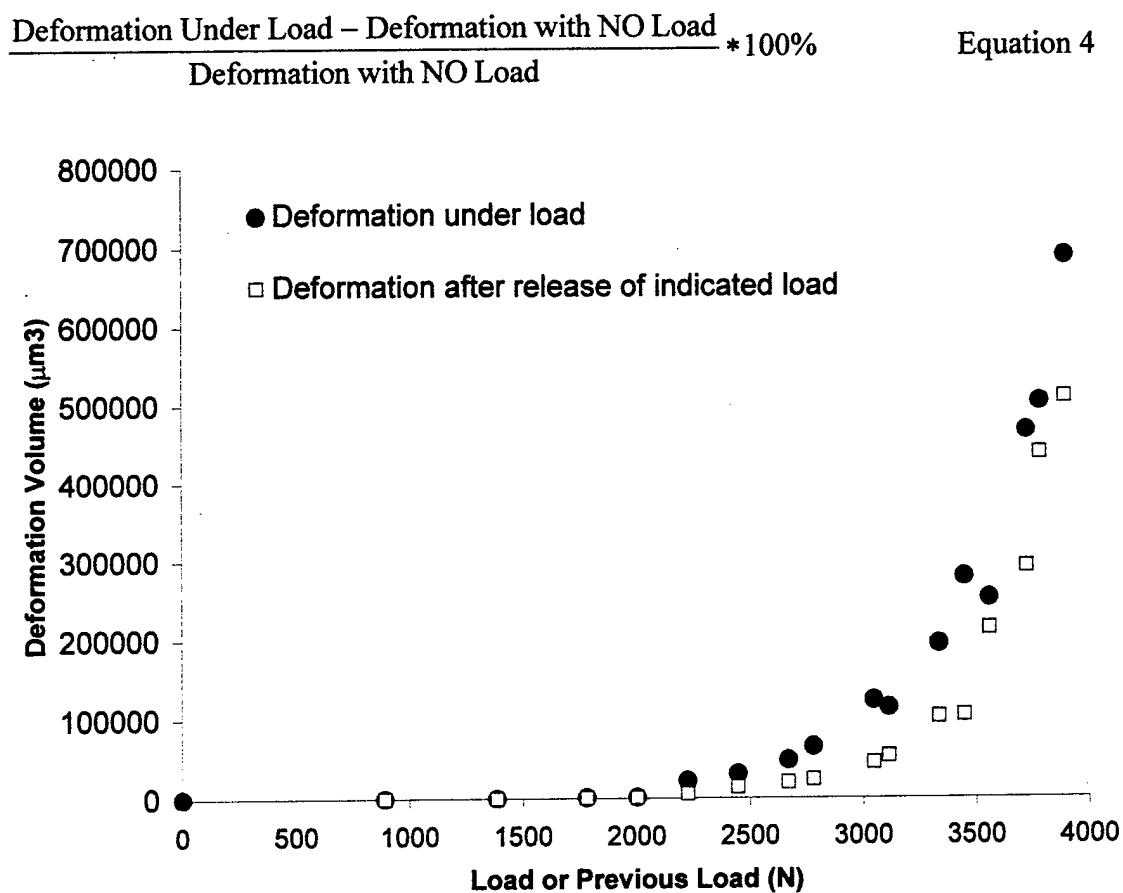


Figure 19. Deformation relaxation after release of load for mill-annealed material.

3.5 Criteria for Failure Prediction

Examination of the common relationship between deformation zone size and the stress intensity factor indicates that criteria for failure may be extracted from surface deformation data. The suggested criterion for failure is a critical rate of change (r_c). This rate is the slope of the size of deformation over the stress intensity factor at a determined point prior to failure. A schematic of this rate is shown in Figure 20.

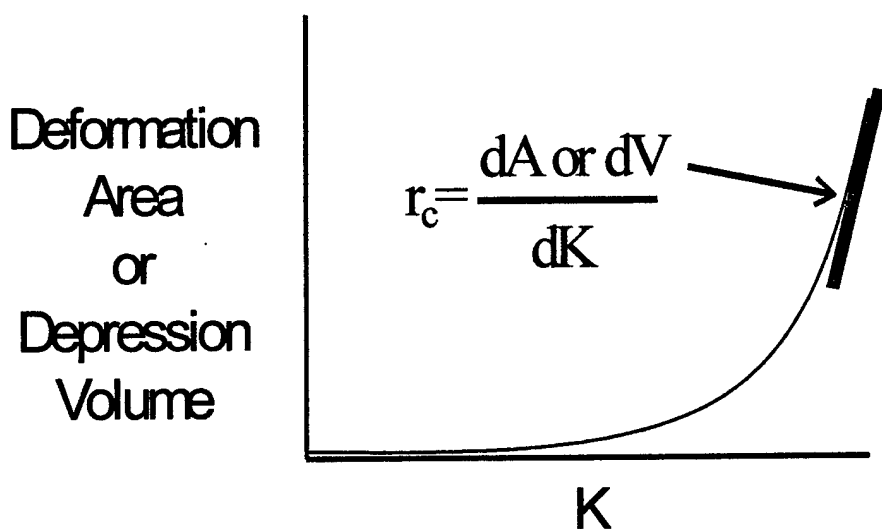


Figure 20. Criteria for failure: critical rate of deformation growth with respect to change in stress intensity factor (a schematic).

CHAPTER 4

CONCLUSIONS AND RECOMMENDATIONS

4.1 Conclusions

The objective of this work was to develop a method to characterize the deformation zone ahead of a crack tip using white light interference profilometry and from such characterizations develop a methodology to predict upcoming fracture. Results suggest that a comparison of the change in the volume of the depression over the change in the stress intensity factor (dV/dK) can be the basis for development of a nondestructive evaluation method to predict oncoming crack instability of visible flaws.

Through this work, the following findings were made:

1. White light interference profilometry can be successfully used to document the topography of crack tip deformation. Valuable measurements of this deformation include quantification both of the surface area of the deformation and volume of the depression ahead of a crack tip.
2. A distinct deformation zone was found on the surface ahead of a crack tip. This deformation had a distinct shape for all fine-grained mill-annealed and duplex specimens. The shape of this surface deformation zone deviated from the theoretical plastic zone shape. Deformation on coarse β -annealed samples greatly deviated from theoretical plastic zone shapes. The surface deformation of the coarse β -annealed material was uneven and varied in shape from specimen to specimen. This variation was due to the strong influence of the coarse grain structure on the path of the deformation.
3. The surface area of the deformation and volume of the depression ahead of a crack tip increased both as a function of load and a function of time under load.

4. The deformation trends for several microstructures and orientations of Ti-6Al-4V were studied. All curves of the depression volume vs. the stress intensity factor had similar rates. Altering the microstructure caused a shift in the curve of this relationship. The shift was proportional to the difference in the expected K_Q values of the dissimilar microstructures.
5. Deformation relaxation was measured upon release of the static load, but the general deformation curves comparing the volume of the depression and the stress intensity factor still resembled the curves seen during examination of images taken under load.
6. It was proposed that a critical rate of change between the size of the crack tip deformation (surface area of deformation or volume of depression) and the stress intensity factor may be used to predict crack instability. This rate of change (r_c) may be the basis for development of a nondestructive evaluation method to predict oncoming crack instability of visible flaws.

4.2 Recommendations

Future work on this project includes experimental examination of the contribution of plastic deformation to the measured surface deformation. Once a correlation is developed between surface and plastic deformations, profilometric data could provide measurements of plastic deformation that are required for improved fracture mechanics analysis. Additional work includes experimentation with materials other than titanium to possibly broaden the scope of this work.

BIBLIOGRAPHY

1. J. M. Finney, "Fatigue crack growth in metallic military aircraft structures," *Handbook of Fatigue Crack Propagation in Metallic Structures*. (Vol. 2, Elsevier Science B.V., 1994) 1539-1541.
2. Aging of U.S. Air Force Aircraft Final Report, Publication NMAB-488-2, National Academy Press, Washington, D.C. (1997).
3. R.R. Boyer, "An overview on the use of titanium in the aerospace industry," *Materials Science and Engineering A213*, 103-114 (1996).
4. K. Nakajima, K. Terao, and T. Miyata, "The effect of microstructure on fatigue crack propagation of $\alpha+\beta$ titanium alloys In-situ observation of short fatigue crack growth," *Materials Science and Engineering*, A243, 176-181 (1998).
5. M. Niinomi and T. Kobayashi, "Fracture characteristics analysis related to the microstructures in titanium alloys," *Materials Science and Engineering*, A213, 16-24 (1996).
6. D. Eylon, lecture notes: Light Metal Alloys, University of Dayton, 1998.
7. Howard E. Boyer and Timothy L. Gall, *Metals Handbook: Desk Edition*, (American Society for Metals, Metals Park, Ohio, 1985), 9.1-9.12.
8. D. Eylon and P. J. Bania, "Fatigue cracking characteristics of β -annealed large colony Ti-11 alloy," *Metallurgical Transactions A*, 9A, 1273-1279 (1978).
9. P. D. Nicolaou, E. B. Shell, T. E. Matikas, "Microstructural and surface characterization of Ti-6Al-4V alloys after fretting fatigue," *Materials Science and Engineering A269*, 98-103 (1999).

10. Masayuki Shimojo, Makoto Chujo, Yakichi Higo and Shigetomo, "Mechanism of the two stage plastic deformation following an overload in fatigue crack growth," *Int. J. Fatigue* Vol. 20, No. 5, 365-371 (1998).
11. G. A. Harman, J. W. Provan, "Fatigue crack-tip plasticity revisited – The issue of shape addressed," *Theoretical and Applied Fracture Mechanics* 26, 63-79 (1997).
12. Richard W. Hertzberg, *Deformation and Fracture Mechanics of Engineering Materials*, (John Wiley & Sons, New York, New York, 1983), 279-280.
13. G. C. Sih, "Some basic problems in fracture mechanics and new concepts," *Engineering Fracture Mechanics*, Vol. 5, 365-377 (1973).
14. *ASM Handbook Vol. 19*, (ASM International, Materials Park, Ohio, 1996), 5.
15. D. B. Barker, R.J. Sanford and R. Chona, "Determining K and related stress-field parameters from displacement fields," *Experimental Mechanics*, 399-407, (December 1985).
16. R. J. Sanford and J. W. Daily, "A general method for determining mixed-mode stress intensity factors from isochromatic fringe patterns," *Eng. Fract. Mech.*, 11, 621-633 (1979).
17. C. W. Smith, D. Post, G. Hiatt, and G. Nicoletto, "Displacement measurements around cracks in three dimensional problems by a hybrid experimental technique," *Experimental Mechanics*, 23 (1), 15-20 (1983).
18. Robert J. Sanford, "Determining fracture parameters with full-field optical methods," *Experimental Mechanics*, 241-247 (September 1989).

19. B. S. -J. Kang, Y.-N. Zhuang and Q.-K. Liu, "Experimental investigation of creep-crack-tip deformation using moiré interferometry," *Experimental Mechanics*, 309-315 (December 1992).
20. H. Krishnamoorthy and H. V. Tippur, "Extracting fracture parameters using local collocation of full-field displacement data," *Experimental Techniques*, 22-25 (January/February, 1999).
21. M. S. Dadkhah, A. S. Kobayashi, F. X. Wang and D. L. Grassler, "J-Integral measurement using moiré interferometry," *Proc. VI Int. Cong. Exp. Mech.*, 227-234 (1998).
22. Ashraf-F Bastawros and Kyung-S Kim, "Experimental analysis of near-crack-tip plastic flow and deformation characteristics (I): Poly crystalline aluminum," *Journal of the Mechanics and Physics of Solids* 48, 67-98 (2000).
23. T. D. Dudderar and H. J. Gorman, "The determination of Mode I Stress-intensity factors by holographic interferometry," *Experimental Mechanics*, 13 (4), 145-149 (1973).
24. Sridhar Krishnaswamy, Hareesh V. Tippur and Ares J. Roaskis, "Measurement of transient crack-tip deformation fields using the method of coherent gradient sensing," *J. Mech. Phys. Solids* Vol. 40, No. 2, 339-372 (1992).
25. S. Ramaswamy, H. V. Tippur and L. Xu, "Mixed-mode crack-tip deformations studied using modified flexural specimen and coherent gradient sensing," *Experimental Mechanics*, 218-227 (September 1993).
26. G. Han, M. A. Sutton and Y.J. Chao, "A study of stationary crack-tip deformation fields in this sheets by computer vision," *Experimental Mechanics*, 125-140 (June 1994).

27. C. F. Shih, W. R. Andrews, and R. G. Delorenxi, "Studies on crack initiation and stable crack growth," *Elastic-Plastic Fracture*, ed. J. D. Lands, J. A. Begley and G. A. Clarke, ASTM STP 668, Amer. Soc. Test. Mat., 170-186 (1974).
28. W. H. Tuppeny, Jr. and A. S. Kobayashi, *Manual on Experimental Stress Analysis*, 2nd ed., (Society for Experimental Stress Analysis, West Port, CT, 1965), 29-48.
29. Albert S. Kobayashi, *Handbook on Experimental Mechanics*, (Society for Experimental Mechanics, Inc. Prentice-Hall, Inc. Englewood Cliffs, NJ, 1987), 162-427.
30. Paul Caber, "Interferometer characterizes laser-textured steel," *Laser Focus World*, 157-158 (November 1997).
31. Brain Bowe and Vincent Toal, "White light interferometric surface profiler," *Optical Engineering*, 37(6), 1796-1799 (1998).
32. Eli Raz, "A multiple white light interferometer," *Rev. Sci. Instrum.* 67 (10), 3416-3419 (1996).
33. S. Lippold and J. Podlesny, *Surface Profilers: Technical reference manual*, (Wyko Corporation, Tuscon AZ, 1996), 1-1 - 1-12.
34. Thom Connolly, "Scanning interferometer characterizes surfaces," *Laser Focus World*, 85-87 (August 1995).